UNIVERSITY OF CALIFORNIA
SANTA CRUZ

NANOMAGNET DYNAMICS WITH MAGNETOSTATIC AND MAGNETOELASTIC INTERELEMENT COUPLING

A dissertation submitted in partial satisfaction
of the requirements for the degree of

DOCTOR OF PHILOSOPHY

in

ELECTRICAL ENGINEERING

by

Yu Yahagi

December 2015

The Dissertation of Yu Yahagi is approved:

Professor Holger Schmidt, chair

Professor Michael Isaacson

Professor Nobuhiko Kobayashi

Tyrus Miller
Vice Provost and Dean of Graduate Studies

Table of Contents

List of Figures and Tables

Abstract

Densely packed nanomagnet arrays are intensely investigated as the basis of spintronic devices as well as for understanding the fundamental physics of the magnetic spins in confined structures. As nanomagnet devices reduce their dimensions to the nanometer scale, their behavior is critically modified by numerous factors such as the finite size, shape, interfacial effects, fabrication defects, and interelement coupling. Among them, this thesis specifically addresses two factors controlling the interelement coupling.

First, we discuss dipolar coupling between nanomagnets with a novel dynamic separation approach. By probing densely packed arrays of nickel elliptic disks and distinguishing signals in the frequency domain, individual subgroups of nanomagnets are characterized beyond the diffraction-limited spatial resolution. The technique is applied to nanomagnet arrays consisting of nickel elliptic disks with different orientations. Supplemented with micromagnetic simulations, the effect of the dipolar coupling on a specific nanomagnet subgroup is identified. The second part investigates the magnetization dynamics magnetoelastically coupled with surface acoustic waves (SAWs). In nanopatterned periodic arrays, magnetization precession and SAWs are simultaneously excited by a pump laser pulse. We show for the first time that the magnetization response is indeed coupled to the SAWs in nanomagnet arrays and the spin wave spectra are distinctly altered from the unperturbed ones, showing pinning and enhancement of the magnetization precession at the SAW frequencies. Taking the magnetoelastic effect into account, a newly developed

simulation procedure demonstrates excellent reproduction of the measurements. Extension modules for OOMMF micromagnetic simulation framework have been developed to offer general magnetoelastic modeling capability and are now publically available. Utilizing these experimental and modeling techniques, we present a novel experimental method for characterizing the damping parameter of nanostructured magnets. The linewidth of the pinning of the magnetization precession is directly connected with the Gilbert magnetization damping parameter and is utilized as an accurate measure for its experimental estimation, avoiding usual issues associated with the time-domain analysis. The new method enables accurate characterization of the damping parameter of nanopatterned magnets, governing important spintronic device characteristics such as threshold current density in spin transfer torque magnetic random access memories and transition jitter in heat-assisted magnetic recording.

Acknowledgement

This work was realized only with the support of my mentors, colleagues, collaborators, thesis committee, friends, and families. I am deeply grateful of all of them. Among them, I would like to articulate my special appreciation to several individuals for their help with particular salience. First and above all, Holger Schmidt, my advisor, with his great patience, has given me opportunities to work on the dissertation projects and carry them through to completion. Through many hours of discussions in the past several years, he has fostered my attitude about research activities and prepared me as a scientist. It was a pleasure to work with all my colleagues, with special thanks to those with whom I worked closely on the nanomagnet dynamics. Zhigang Liu and Rebekah Brandt kindly shared their expertise and brought me to the frontier of the field. I relied on arduous and brilliant work of my fellows, Cassidy Berk and Mike Jaris. Lastly, but really foremost, I am deeply indebted to my wife, Ayako. Without her unconditional support, which I received in our times of hardship, I would not be where I stand today. This thesis has been dedicated to her and I am particularly glad to have heard her words of acceptance.

1. Introduction

1.1 Spintronics for information technologies

Fabrication capability on the dimension of nanometers, comparable to the spin diffusion length in nonmagnetic metals [1,2], enabled use of electron spins in addition to the electronic charges in handling information. In contrast to the conventional magnetic devices where the spins are manipulated and probed with induction coils, spintronic devices utilize quantum-mechanical effect and achieve higher energy efficiency and signal to noise ratio (SNR). The field of study on such devices is termed spintronics and has been intensely studied with its main interest in recording applications, magnetic sensing, and communication as will be discussed below.

The early phase of spintronics research was fueled by the interest in hard disk drives (HDDs). In particular, research gained momentum after development of giant magnetic resistance (GMR) in 1980s, pushing the limit of the magnetic field detection in the HDD read head [3,4]. A spin valve structure exhibits distinct resistance depending on the relative orientation of the spin configuration (parallel or antiparallel) in the pinned and free layers. As depicted in Fig. 1.1, the parallel and antiparallel configurations differently scatter the conduction electrons depending on their spins. In the parallel configuration (Fig. 1.1a), the spin-up electrons can travel through the spin valve virtually without scattering and provide low resistance. In the antiparallel configuration (Fig. 1.1b), both spin-up and spin-down electrons are

scattered and the spin valve exhibits high resistance. After the discovery of GMR, several other breakthroughs have enabled continued growth in the areal recording density in HDDs. Tunneling magnetic resistance (TMR) further improved the detection SNR [5,6]. As depicted in Fig. 1.2, TMR is found in a magnetic tunneling junction (MTJ) structure, having a tunnel barrier instead of the nonmagnetic metal layer in GMR. Electrons with a certain spin state can tunnel through the barrier only when there are available states corresponding to the same spin in the other ferromagnetic layer. In the parallel configuration (Fig. 1.2a), the majority spin electrons can tunnel to the majority spin states in the second layer and the MTJ exhibit large conductance. In the antiparallel configuration (Fig. 1.2b), however, the mismatch of the available spin states in the two layers results in large resistance. The magnetic recording media also have undergone a major technical transition for higher areal recording density; conventional longitudinal recording configuration was replaced by perpendicular magnetic recording (PMR) in early 2000s [7]. As illustrated in Fig. 1.3a, PMR is achieved with a single-pole write head and a soft underlayer (SUL), which forms a mirror image of the pole and completes the magnetic circuit. Comparing to the fringe field in longitudinal recording, this enables larger writing field for switching the recording bits with larger coercivity. PMR has achieved smaller recording bits and has replaced the longitudinal recording in HDDs [7–10]. As a result of these compound improvements, the recording density of HDDs increased exponentially at an average rate of ~40%/year since 1980s until early 2000s [11]. Having a fabrication advantage of not requiring nanopatterning in lateral

dimensions (a flat planar film of thin granular magnetic layers), HDDs dominated information storage for several decades, followed by the advancement of the Gbit/in^2 NAND flash memories in recent years [12].

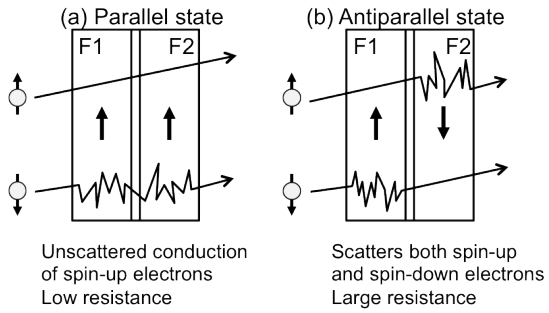

Fig. 1.1. Schematic diagram of giant magnetoresistance (GMR). Two ferromagnetic layers (F1, F2) are separated by a thin nonmagnetic metal layer. (a) Parallel and (b) antiparallel configurations. Conduction electrons with different spin states undergo different levels of scattering, resulting in large change in resistance.

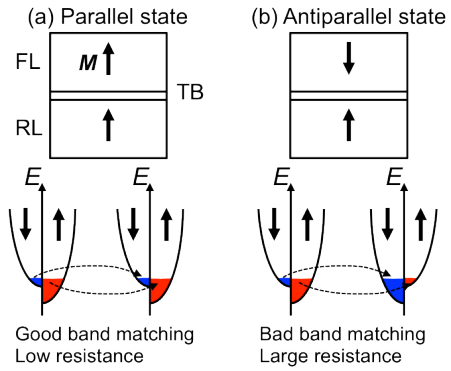

Fig. 1.2. Schematic diagram of a magnetic tunneling junction (MTJ). A reference layer (RL) and a free layer (FL) are separated by a tunneling barrier (TB). (a) Parallel and (b) antiparallel states. Conduction electrons can tunnel between the FL and RL

only when there are available states in the other layer corresponding to the same spin state. Mismatch of these states leads to large resistance.

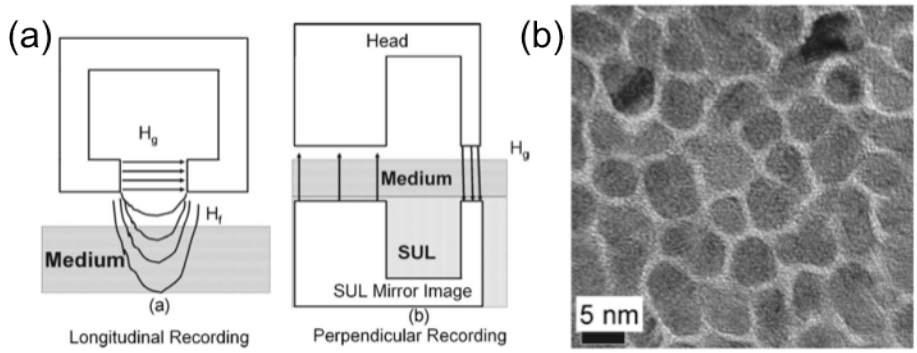

Fig. 1.3. (a) Schematic diagram of longitudinal (left) and perpendicular (right) magnetic recording (PMR). In PMR, a soft underlayer (SUL) can be seen as a mirror image of the single-pole write head, completing the magnetic circuit. (b) Scanning electron micrograph of a CoCrPt granular PMR medium. Taken from [7].

The growing trend of the HDD recording density is facing a fundamental limit in thermal stability called the superparamagnetic limit. A recording bit in HDD media is formed with multiple magnetic grains (Fig. 1.3b) each of which is saturated in one direction. In order to form sufficiently smooth recording bits, the grain size needs to be much smaller than the size of the recording bits [7]. As the average grain diameter reduces to 6-7 nm [7,9], the thermal fluctuation becomes significant. The characteristic time for thermal spin flipping τ at the temperature T is governed by the Neel-Arrhenius law [13,14]

$$\tau = \tau_A \exp\left(\frac{KV}{k_B T}\right), \tag{1.1.1}$$

where K is the anisotropy constant, V is the average grain volume, k_B is the Boltzmann constant, and $1/\tau_A$ is the attempt frequency, typically in the order of 10^9 to 10^{12} s^{-1} [13,15,16]. To achieve stable storage for 100 years ($\tau = 3.15\times10^9$ s), $KV/k_BT >$ 40–50 is desired. τ undergoes a very steep change around a grain diameter of a few nanometers, limiting further decrease in the recording bit size. Available magnetic field from a HDD write head limits K, which governs the coercivity of the recording media. To extend this limit, two basic concepts have been actively investigated—increasing the grain volume V or the anisotropy energy K.

The first approach takes the form of bit patterned media (BPM) (Fig. 1.4) [9,10,17–19]. By patterning the recording medium into a densely packed array of single-domain nanomagnets, and by using thicker nanomagnets, the grain volume V can be increased to the size of the single recording bit. This approach, however, abandons the advantage of the HDD media of not requiring nanoscale fabrication in lateral dimensions and is subject to the fabrication difficulties, rather poor yield, large switching field distribution [18], as well as a demand for a high-speed error correction scheme in case the read/write head "misses" a nanomagnet [9]. In the context of the advanced HDD technologies, the focus of studies has shifted toward the second approach with higher anisotropy material and structures, implemented with energy assisting to overcome a large switching energy barrier. Among such approaches, heat-assisted magnetic recording (HAMR) is most promising and widely studied

[9,20–25]. In this approach, the recording media are constructed with materials of high coercivity (e.g., FePt with $L1_0$ phase or Co/Pt and Co/Pd multilayers and superlattices), easily exceeding 50 kOe with the grain diameter below 5 nm. In order to overcome the switching energy barrier, embedded laser light is delivered to the narrowly confined region through a plasmonic waveguide to heat the medium up close to the Currie temperature, lowering the coercivity field of the grains.

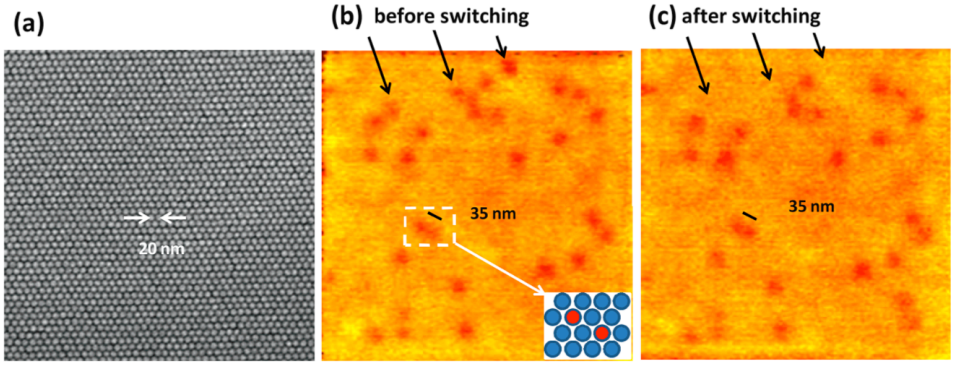

Fig. 1.4. (a) Scanning electron micrograph of Co/Pd multilayer nanomagnet dots, deposited on pre-patterned SiO_x posts. The array pitch is 20 nm, corresponding to an areal density of 1.9 Tbit/in^2. (b, c) Sequential mangetic force micrography images taken at remanence after applying switching fields at 13.55 and 13.60 kOe, respectively. Dark spots indicate individual bits that remained unswitched. The black arrows point to three bits that flipped their state due to the increase in the switching field by 50 Oe. Taken from [10].

Advancement of basic spintronic components has led to incarnation of new recording technologies. Magnetic random access memories (MRAMs) have acquired

a broad interest in practical recording application due to the scalability, nonvolatility, high switching speed (< 20 ns), and virtually unlimited write endurance (>10^{16} write cycles), ideal for replacing the dynamic random access memories (DRAMs) for the computer main memory [26–29]. An MRAM cell consists of an MTJ (Fig. 1.2). The information is stored as the magnetization direction of its free layer, which is flipped with the magnetic field from writing striplines. With a CMOS transistor connected in series to the MTJ, the free layer spin orientation is obtained with the TMR. The first demonstration of MRAMs was formed with an amorphous aluminum oxide barrier. A crystalline MgO (001) barrier was shown to achieve much larger TMR ratio and has been used in newer MRAM designs [30–36].

In contrast to passive spintronic effects, such as GMR and TMR, active effect of the spin-polarized current on the spin has enabled efficient spin manipulation. The spin transfer torque (STT) is a transfer of angular momentum from a spin-polarized current to the spins in the ferromagnets [37,38] and can switch the spin orientation [34,39–41]. It is combined with the MTJ structure as an STT-MRAM device. To flip the free layer magnetization in this design, a sufficiently large current is simply applied through the MTJ stack. It eliminates the need for writing transmission lines and reduces the device footprint by an order of magnitude down to ~2 F^2, where F is the lithographic minimum feature size [42]. The required power for switching an MTJ also scales down with decreasing device size, as opposed to the exponential increase in the conventional MRAM design with writing field application [27]. Therefore, low

switching current density J_{c0} is a key parameter in development of STT-MRAMs. For a perpendicular MTJ [15],

$$J_{c0} = \frac{1}{\eta}\frac{2\alpha e}{\hbar} M_S t H_K \tag{1.1.2}$$

is directly proportional to the Gilbert damping parameter α, which will be defined in section 2.2. CoFeB has an advantage of low damping and is now the main material for future MRAM designs, typically achieving J_{c0} in the order of 10^6 A/cm^2 [15,33,34,43].

The STT effect is also utilized in racetrack memories (RTMs) for moving the magnetic domains across permalloy nanowires [44]. Their concept is sketched in Fig. 1.5. Magnetic domains are switched with the field from a fixed write head. Instead of moving the write head structure as in HDDs, the RTM moves the magnetic domains with spin-polarized current. The bit length (spacing between consequent domain walls) is controlled by pinning sites fabricated along the nanowire. The speed and repeatability of domain wall motion are studied intensely for realization of RTMs. RTMs involve rather large magnetic domains for information storage and do not appear particularly advantageous in high recording density. The major significance of this structure is that it is probably the closest candidate for the three dimensional recording, which would easily increase the recording capacity by a factor of many orders of magnitude by extending the recording structure in the z direction.

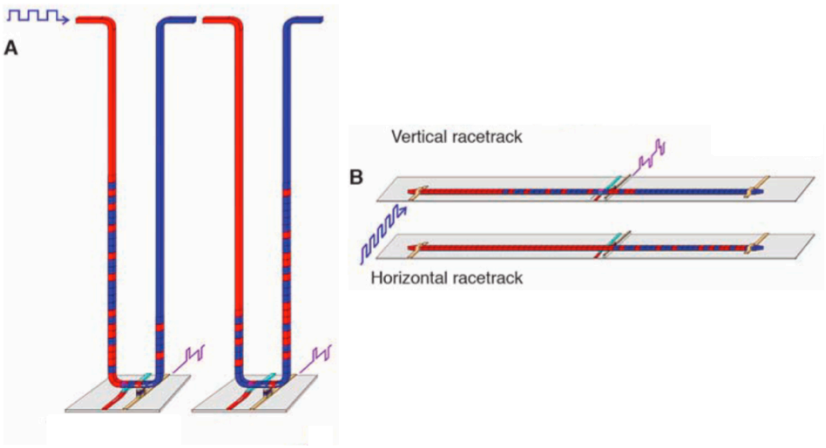

Fig. 1.5. Two configurations proposed for racetrack memories (RTMs). Pulsed spin-polarized current is applied at the left end of the nanowires to move the domain walls. (A) Vertical configuration would provide high storage density by storing information as domain wall positions in U-shaped nanowires. (B) Horizontal configuration is easier to fabricate for experiments. Taken from [44].

Apart from recording applications, STT is also being investigated as a potential source of GHz oscillation [45,46] for communication, microwave-assisted magnetic recording (MAMR) applications, and for RF signal detection [47]. By applying a DC voltage across a MTJ structure and balancing the STT and damping in the free layer, a steady spin precession at the ferromagnetic resonance (FMR) frequency can be excited. The AC power can be extracted with a GMR sensor. Other microwave oscillators (e.g., monolithic microwave ICs) involve integrated circuitry with resonators, mixers, amplifiers, and filters and have low efficiency. The STT

oscillator can be achieved with a single MTJ and can be incorporated with conventional LSI fabrication.

Recently, an unprecedented spin-switching phenomenon called the all-optical switching (AOS) was demonstrated in rare-earth–transition-metal ferrimagnet alloys [48–58] and in synthetic ferrimagnets [59,60]. When the sample is irradiated with a single laser pulse with circular polarization, the net magnetization of the ferrimagnet switches its direction without any external field. The exact mechanism of the switching still remains controversial but it is typically understood as a combination of the heating close to the Currie temperature and the inverse Faraday effect, acting on two ferrimagnet sublattices with different magnetic moments [50]. Under a narrow window of laser fluence, it is also reported that mere heating with no net magnetic angular momentum (linearly polarized light) can switch the net magnetization as well [51]. Conventional micromagnetics fails to model this phenomenon involving rapid temperature increase and the reduction of net magnetization. Atomistic modeling of such material structures predicted the spin dynamics with different relaxation time scale for the two sublattices that are strongly coupled to each other. This reproduced the purely thermal switching as well [51,61,62]. Atomistic modeling is only applicable to bulk and relatively small structures. Several groups have extended micromagnetics to include temperature-dependent magnetization magnitude and two sublattices but a full-fledged modeling of micrometer-scale structures has not been reported. AOS typically involves a laser spot of 30–150 μm in diameter and is not immediately applicable for nanoscale recording bits. While AOS in micro- and

nanopatterned GdFeCo was demonstrated [53,54,58], it is not clear what exact condition is required for AOS, especially with nonuniform condition in patterned elements. Therefore, investigation and modeling of the AOS on nanopatterned structures or with near field laser excitation is of great interest.

1.2 Magnetization dynamics in nanopatterned magnets

In the context of the development of magnetic recording technologies, we are particularly interested in the magnetization dynamics of nanostructured magnets. The dynamics of nanostructures is engineered through size, shape, coupling with other layers, mechanical stress, and material composition. They have been widely studied as a basis of spintronic devices, as well as a platform to understand fundamental physics in material science. As the development of modern information technology demands smaller recording bits on a nanometer scale and faster operation in the GHz range, it is becoming ever more critical to understand the spin dynamics of nanostructured magnets.

The finite size and shape of nanomagnets cause the spin behavior to deviate distinctly from that of the bulk and planar films. On studies of soft magnets (e.g., permalloy) patterned on a micro- and nanometer scale, the finite size leads to a nonuniform distribution of the magnetization in individual magnets and generates a nonuniform demagnetization field. In addition to shifting the FMR frequency, multiple spin wave eigenmodes are present [63–69]. The large change in effective field tends to be confined close to the device edges and gives rise to the edge mode, a spin wave eigenmode whose power is confined close to the nanomagnet edges.

Numerous confined spin wave modes appear and complicate the magnetization dynamics. These modes are heavily dependent on the magnet shape, size, and aspect ratio (lateral size/thickness). When multiple spin wave modes with overlapping spectra are excited, dephasing of these modes makes the net oscillation decay faster than the intrinsic damping [70–73].

Damage and defects induced in nanopatterning, such as implantation of impurities, disordered lattice structures, edge and interface roughness can also lead to a significant modification of spin dynamics [74–78]. It is difficult to model the exact origin and nature of the localized damage and is usually treated as a phenomenological modification of macroscopic material parameters. Modeling of local variation of such parameters is often worked out by guess, for example, by reducing the total anisotropy constant in small edge regions. Nevertheless, this approach often predicts noticeable change in device characteristics with edge damage of just a few nanometers [76–78].

In thin, small nanomagnets with large anisotropy that is of interest for memory applications, the exchange interaction prefers excitation of a single coherent precession mode. The large anisotropy energy required for thermal stability often dominates the magnetization dynamics and the relative importance of magnet shape becomes less significant. In this regime, fabrication damage and defects play a large role in determining the magnetization dynamics [77].

When the nanomagnets are closely packed in an array with small separations, interelement coupling induces crosstalk between the recording bits. In nanomagnet

arrays, the dipolar field from the neighboring elements changes both static and dynamic properties of the whole array. When the nanomagnets are placed in a magnetostatic environment that is modified by the stray dipole field from neighboring elements, they can have different ground state of the magnetizations, leading to distinctly different precession frequencies [79–81] and switching field distributions [82–84]. Dynamic dipolar coupling also excites a number of collective spin wave modes for the entire array structure [85–87], splitting and broadening the mode spectra via energy transfer to the neighboring elements at the FMR frequency. This can alter the switching characteristic of each nanomagnet too [88].

In dynamic measurements on nanomagnet arrays, the spatial resolution of the measurement techniques poses an important issue. Typically, the signal of such measurements is an averaged response of many nanomagnets within the detection region including deviations of each nanomagnet. It is difficult to retrieve the covert dynamics of individual nanomagnets. For example, due to the deviation in shape, size, and localized defects, each nanomagnet is expected to have a slightly different FMR frequency. This broadens the mode spectra and may cover the splitting of different spin wave modes within each nanomagnet or cause an apparent increase in the damping rate [85]. In order to probe the dynamics of individual nanomagnets, measurements on isolated single magnets are often desired to complement the array measurement [71,89–95]. Alternatively, detection of a single nanomagnet within a densely packed array with high spatial resolution is required. Both approaches typically suffer lower signal to noise ratio (SNR). In chapter 4, we will discuss the

dynamic separation approach to probe individual nanomagnets within densely packed arrays beyond the diffraction limit.

Coupling of the magnetization dynamics with mechanical vibration also has a non-negligible role. Periodically patterned nanostructures have mechanical eigenmodes in the GHz range and can strongly alter the magnetization dynamics via magnetoelastic coupling. This greatly complicates the measurements of array structures. We have developed a measurement and analysis technique to model the magnetoelastically coupled dynamics in nanopatterned structures. Chapter 5 gives more detailed descriptions of the theories and analysis methods, followed by several chapters demonstrating such phenomena in TR-MOKE experiments and numerical simulations.

1.3 Problem statement and chapters

Among the factors affecting nanomagnet dynamics presented in the last section, this thesis specifically discusses two problems. First, we will discuss the dynamic separation approach to probe distinct groups of nanomagnets within densely packed arrays beyond the spatial resolution of diffraction-limited optics. The second part of the thesis investigates the magnetoelastic coupling with surface acoustic waves strongly altering the magnetization behavior. This thesis is organized as follows.

Chapter 2 introduces the theory of magnetization dynamics. With a brief description of Hamiltonian terms of a spin system, it is mainly discussed using the micromagnetic model to describe nanometer-scale structured magnets. An example of

a small-angle precession mode (Kittel mode) is presented. This chapter ends with concepts of numerical analysis within the framework of micromagnetics.

Chapter 3 describes the measurement principles and techniques. Magneto-optic effects as the probe of magnetization will be introduced in a semiclassical Lorentzian model and will be related to the dielectric tensor of magnetically ordered materials. General remarks of time-resolved magneto-optic measurement techniques and the actual setup description will be given as well as a brief description of the analysis techniques used to interpret the experimental data.

In Chapter 4, we present the dynamic separation approach applied on nickel elliptic disks. This chapter investigates the dipolar coupling of nickel nanomagnets and resolves the magnetization dynamics in individual groups of nanomagnets, oriented in different directions. Supplemented with micromagnetic simulations, the dipolar coupling within densely packed arrays is characterized.

Chapter 5 presents the magnetoelastic effect in densely packed nanomagnet arrays. The dynamics of nanomagnet spins are strongly coupled to the surface acoustic waves simultaneously excited with the pump laser pulse. In this chapter, the basic theory of magnetoelastically coupled system is introduced. A numerical simulation procedure to model such systems with a complex structure was developed and will be discussed.

Chapter 6 presents the first demonstration of strong magnetoelastic coupling in nanostructured magnets. The behavior of the magnetization precession turned out to be drastically different from the pure magnetic response. The modeling procedure

introduced in Chapter 5 is applied to interpret the observed dynamics, yielding excellent agreement.

In Chapter 7, using the knowledge of the magnetoelastically coupled dynamics attained in previous chapters, we propose a novel experimental method to characterize the damping parameter of nanopatterned magnets. The method is utilized for characterizing TbFe, nickel, and cobalt nanomagnet arrays. Its validity is corroborated with a theory, simulations, and comparison with another experimental method.

Chapter 8 summarizes findings presented in the preceding chapters. It closes the thesis by discussing their significance and future prospects.

2. Magnetization dynamics

This chapter will review theories concerning the magnetization dynamics. The magnetization is first presented as an electron spin localized at atomic sites and the Heisenberg exchange is introduced as a practical model to explain the ferromagnetic ordering. For analysis of magnetization dynamics on a 100-nm length scale, micromagnetics is introduced as an approximation. The Landau-Lifshitz (LL) and Landau-Lifshitz-Gilbert equations are presented as the governing equations of the magnetization motion within this framework, along with a representative solution of the small angle precession. Finally, concepts and challenges of numerical simulation approaches are discussed at the end of the chapter.

2.1 Energy terms in Heisenberg Hamiltonian

Magnetization in a material is modeled as a net magnetic dipole moment per unit volume, originating from the angular momentum of the electron. In a classical model, this is viewed as a loop current of an electron with the mass m and charge e (< 0) traveling at the speed of v along a circular trajectory of radius a. The loop current of $I = ev/(2\pi a)$ gives the magnetic dipole moment

$$\mu = \pi a^2 |I| = \frac{|e| av}{2} \tag{2.1.1}$$

at the center of the loop. (2.1.1) is related to the angular momentum of the electron $\Gamma = mav$ as

$$\mu = \frac{|e|}{2m}\Gamma . \tag{2.1.2}$$

In a quantum-mechanical view, the angular momentum is discretized with the separation $\hbar$ and is expressed with an azimuthal quantum number l as

$$\Gamma_l = \sqrt{l(l+1)}\hbar . \tag{2.1.3}$$

Substituting (2.1.3) in (2.1.2), the Bohr magneton μ_B is defined as the coefficient for obtaining the magnetic moment of an electron.

$$\mu = \frac{|e|\hbar}{2m}\sqrt{l(l+1)} = \mu_B\sqrt{l(l+1)} . \tag{2.1.4}$$

Under an external magnetic field, the z component (parallel to the external field) of the orbital angular momentum is quantized into $2l+1$ values and expressed as

$$\mu_z = \frac{|e|\hbar}{2m}m_l = \mu_B m_l \tag{2.1.5}$$

with the magnetic quantum number m_l, taking an integer value between $-l$ to $+l$. In addition to the orbital angular momentum, the electron spin contributes to the magnetic moment. The spin angular momentum $\Gamma_s = \hbar\sqrt{s(s+1)}$ is expressed with the spin quantum number s, taking a value of $s = \pm 1/2$ and contributes to the spin magnetic moment

$$\mu_s = \frac{|e|\hbar}{m}\sqrt{s(s+1)} = 2\mu_B\sqrt{s(s+1)} . \tag{2.1.6}$$

When more than one electrons occupy the incomplete shell, the orbital and spin angular momenta $\boldsymbol{\Gamma}_{l,i}$ and $\boldsymbol{\Gamma}_{s,i}$ of the ith electron are vectorially added and result

in the net orbital and spin angular momenta $\boldsymbol{\Gamma}_L$ and $\boldsymbol{\Gamma}_S$. They are expressed by the quantum numbers

$$L = \sum_i m_{l,i},\ S = \sum_i s_i\ , \tag{2.1.7}$$

replacing l and s in the previous discussion. $m_{l,i}$ and s_i are the magnetic and spin quantum numbers for the ith electron in the incomplete shell and are determined by the following Hund's rules:

(1) s_i are decided by maximizing S in accordance with the Pauli exclusion principle.

(2) $m_{l,i}$ are decided by maximizing L in accordance with rule (1).

(3) The total angular moment quantum number J is determined as

$$J = \begin{cases} |L-S| & \text{(for a shell less than half occupied)} \\ L+S & \text{(for a shell more than half occupied)} \end{cases}. \tag{2.1.8}$$

The net magnetic moment is obtained as

$$\mu = \frac{g\mu_B}{\hbar}\Gamma = g\mu_B\sqrt{J(J+1)} \tag{2.1.9}$$

with the Landé g-factor

$$g = 1 + \frac{J(J+1)+S(S+1)-L(L+1)}{2J(J+1)}. \tag{2.1.10}$$

The g-factor represents the relative contribution of the orbital and spin angular momenta to the net magnetic moment. For example, it takes a value of g = 1 and 2 for a purely orbital and purely spin contribution, respectively. For the free atoms or ions of 3d and 4f metals, the values of L, S, and J are calculated with the Hund's rules and

are shown in the top row of Fig. 2.1. Note, however, that in 3d transition metal ions in a solid, the orbital angular momentum is quenched and L is small. Because the electric field in the lattice turns the plane of the orbits into crystallographic directions, the 3d orbital angular momentum $\Gamma_{L,z}$ average to zero [96 p. 35,97 p. 74,98 pp. 386–390]. As seen in the bottom row of Fig. 2.1, the magnetic moments measured in 3d metals closely follow the theoretical calculation $\mu = 2\mu_B\sqrt{S(S+1)}$, assuming only the spin angular momentum. In 4f metals, on the other hand, the 4f electrons are closer to the nucleus than those of the 5s and 5p electrons. They are effectively screened from the effect of the electric field in the lattice and contribute to the net magnetic moment, making Eq. (2.1.9) a good model.

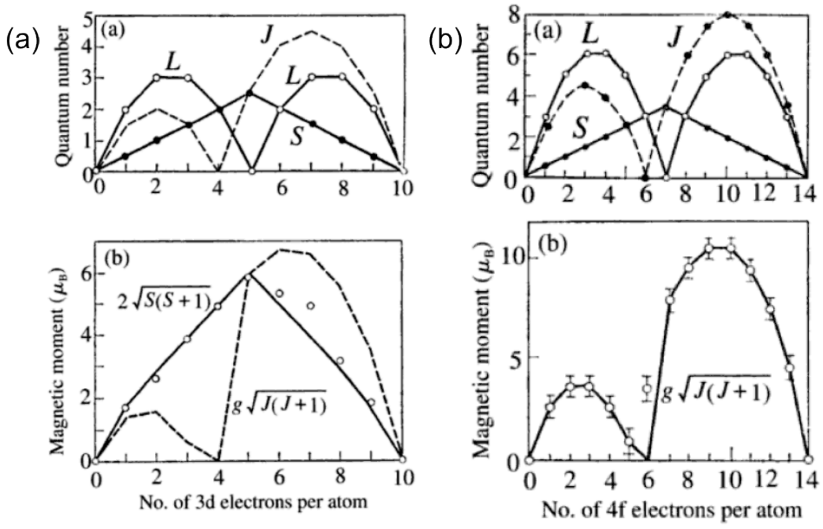

Fig. 2.1. (Top) The quantum numbers S, L, and J for free 3d and 4f atoms. Taken from [98].

Eq. (2.1.9) is also a generalized form of (2.1.2) with the net angular momentum Γ. The ratio of the magnetic dipole moment μ and Γ is defined as the gyromagnetic ratio

$$\gamma = \frac{g|e|}{2m}. \tag{2.1.11}$$

As will be discussed in section 2.2, this appears as a coefficient determining the torque on the magnetization vector and thus the frequency of its precession motion.

The origin of ferromagnetic and antiferromagnetic ordering is addressed with the Heisenberg model. In this model, the magnetic moments are spins localized at atomic sites. The problem of many electrons with the Coulomb potential energy due to the electron-electron and electron-nuclei interactions is treated with the Hartree-Fock approximation, following a discussion in [96 pp. 36–44]. It utilizes the mean field theory, assuming that effect of other conduction electrons are modeled as a single averaged effect. It thus reduces a many-body problem to a single-body problem. Suppose that when each electron is separated from each other, the electron is described with an eigenfunction

$$\varphi_k(\boldsymbol{\rho}_1), \tag{2.1.12}$$

where $\boldsymbol{\rho}_1$ is the spatial and spin coordinate of the electron 1. When the electrons are brought closer, the wave function of the whole electron system is approximated by a Slater determinant, expressed as the linear superposition of the products of (2.1.12) as [98 pp. 190–195]

$$\psi = \frac{\det[\varphi_k]}{\sqrt{N!}}, \tag{2.1.13}$$

where the numerator is defined as

$$\det[\varphi_k] = \begin{vmatrix} \varphi_1(\boldsymbol{\rho}_1) & \cdots & \varphi_1(\boldsymbol{\rho}_N) \\ \vdots & & \vdots \\ \varphi_N(\boldsymbol{\rho}_1) & \cdots & \varphi_N(\boldsymbol{\rho}_N) \end{vmatrix}. \tag{2.1.14}$$

(2.1.13) obeys the Pauli exclusion principle that requires the wave function to be antisymmetric with respect to interchanging two electrons. Interchanging of any two electrons corresponds to interchanging the two column positions in the right hand side of (2.1.14) and leads to reversal of the sign of ψ. It follows that $\psi = 0$ when $\boldsymbol{\rho}_i = \boldsymbol{\rho}_j$ with $i \neq j$, in accordance with the Pauli exclusion principle, prohibiting two electrons to share the identical quantum state.

The Hamiltonian has the form of

$$\mathcal{H} = \sum_i \mathcal{H}_i + \frac{1}{2}\sum_{i \neq j} \frac{e^2}{r_{ij}} + \mathcal{H}_c\,, \tag{2.1.15}$$

where

$$\mathcal{H}_i = -\frac{\hbar}{2m_e}\nabla_i^2 + V_i \tag{2.1.16}$$

is the standard Hamiltonian operating on the ith electron with the Coulomb potential V_i created by the ion cores. The second summation in (2.1.15) is the Coulomb potential energy due to an electron–electron interaction, and the last term is the Hamiltonian operating on the ion cores. With the definition of the wave function ψ in (2.1.13) and this Hamiltonian (2.1.15), the energy of the system is calculated as

$$\mathcal{E} = \int \psi^* \mathcal{H} \psi \, \mathrm{d}\tau_1 \, \mathrm{d}\tau_2 \cdots \mathrm{d}\tau_N$$

$$= \frac{1}{N!}\int \det[\varphi_{k'}^{*}]\mathcal{H}\det[\varphi_k]\,\mathrm{d}\tau_1\,\mathrm{d}\tau_2\cdots\mathrm{d}\tau_N\,. \tag{2.1.17}$$

Since each term in (2.1.15) is linear and operates only on *i*th and *j*th electrons, (2.1.17) can be expanded as

$$\mathcal{E} = \sum_{i=1}^{N}\mathcal{E}_i + \frac{1}{2}\sum_{i,j=1,i\neq j}^{N}\mathcal{E}_{ij} + \mathcal{E}_c\,, \tag{2.1.18}$$

where the indices i, j denote the numbers determined by the quantum states of the *i*th and *j*th electrons. The second summation in (2.1.18) describes the interaction between pairs of the electrons. This purely electrostatic effect can also be expressed as a spin–spin interaction if the exchange interaction

$$\mathcal{H}_{\mathrm{eff}} = -\sum_{i\neq j} J_{i,j}\boldsymbol{S}_i\cdot\boldsymbol{S}_j \tag{2.1.19}$$

is added to the Hamiltonian [99 pp. 51–58], where $\boldsymbol{S}_{i,j}$ are the spin vectors along the magnetic moment with the magnitude of S and $J_{i,j}$ is the *exchange integral*

$$J_{i,j} = 2\int \varphi_i^{*}(\boldsymbol{r}_1)\varphi_j^{*}(\boldsymbol{r}_2)\frac{e^2}{|\boldsymbol{r}_i-\boldsymbol{r}_j|}\varphi_i(\boldsymbol{r}_2)\varphi_j(\boldsymbol{r}_1)\,\mathrm{d}\boldsymbol{r}_1\,\mathrm{d}\boldsymbol{r}_2\,. \tag{2.1.20}$$

(2.1.19) is the well-known Heisenberg exchange interaction. These terms, as discussed above, are derived as a correction of the Coulomb potential, taking the Pauli exclusion principle into account. The definition of the sign of $J_{\mathrm{i,j}}$ differs in literatures but in the definition of (2.1.20), positive $J_{i,j}$ prefers $\boldsymbol{S}_i$ and $\boldsymbol{S}_j$ to be parallel and causes ferromagnetic ordering. Conversely, negative $J_{i,j}$ results in antiparallel ordering of neighboring spins, as seen in antiferromagnets and ferrimagnets.

The summation in (2.1.19) is, strictly speaking, applied to all pairs of spins in the system. The exchange integral $J_{i,j}$ is a strong function of the distance between the spins and often only nearest neighbors are considered.

2.2 Micromagnetics and Landau-Lifshitz-Gilbert equation

The quantum-mechanical model in the previous section describes the spins at the atomic sites. However, calculation of spins with this approach is frequently too burdensome and unnecessary. Also, it is sometimes difficult to obtain all the material parameters required for description of the whole system. For these reasons, an alternative approach is generally exerted for studying the magnetization dynamics in nanoscale structures. This approach is generally known as micromagnetics and assumes a continuity of magnetization in the material. Despite its name, magnetic quantities, such as magnetization and the energy densities discussed in the previous section, are treated as continuous functions of position and thus assume macroscopic values. For the rest of this thesis, we will be analyzing the magnetization dynamics under this approach.

The equation of motion in micromagnetics was first proposed by Landau and Lifshitz as [100]

$$\frac{\partial \boldsymbol{M}}{\partial t} = -\gamma \boldsymbol{M} \times \boldsymbol{H}_{\text{eff}} - \frac{\gamma\lambda}{M_S^2} \boldsymbol{M} \times (\boldsymbol{M} \times \boldsymbol{H}_{\text{eff}}), \tag{2.2.1}$$

where $\boldsymbol{H}_{\text{eff}}$ is the effective field that will be defined shortly, γ is the gyromagnetic ratio defined in (2.1.11), and λ is a dissipation parameter. Gilbert modified (2.2.1) [101,102] into the form known today as the Landau-Lifshitz-Gilbert (LLG) equation

$$\frac{\partial \boldsymbol{M}}{\partial t} = -\gamma \boldsymbol{M} \times \boldsymbol{H}_{\text{eff}} + \frac{\alpha}{M_{\text{S}}} \boldsymbol{M} \times \frac{\partial \boldsymbol{M}}{\partial t} \tag{2.2.2}$$

by replacing $\gamma \boldsymbol{M} \times \boldsymbol{H}_{\text{eff}}$ in the second term of (2.2.1) by $\partial \boldsymbol{M}/\partial t$ and introducing a dimensionless Gilbert damping parameter α. The two equations are identical when the parameters in (2.2.1) are replaced as

$$\gamma \to \frac{\gamma}{1+\alpha^2} \text{ and } \lambda \to \frac{\alpha M_{\text{S}}}{1+\alpha^2}, \tag{2.2.3}$$

Typically in a bulk of 3d transition metal, α is on the order of 10^{-3}–10^{-2} and the relative difference of γ in (2.2.1) and (2.2.2) is less than a percent. A larger damping parameter on the order of 10^{-1} can be found in alloys or in multilayer structures [103–106] and the difference may be noticeable. Motion of the magnetization is depicted in Fig. 2.2. The first terms in (2.2.1) and (2.2.2) describe the torque on $\boldsymbol{M}$. When no loss is assumed for the system, $\boldsymbol{M}$ continues its precession around the equilibrium axis. The second term describes the loss of the system, which behaves like friction. Both (2.2.1) and (2.2.2) ensures that $\boldsymbol{M}$ retains a constant magnitude and only changes its orientation. This can be shown by taking the dot product of the both sides of (2.2.1) and (2.2.2) with $\boldsymbol{M}$, obtaining

$$\frac{\partial |\boldsymbol{M}|^2}{\partial t} = 0. \tag{2.2.4}$$

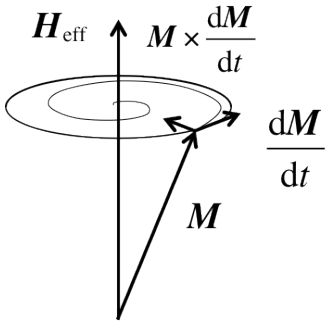

Fig. 2.2. Magnetization precession described with the LLG equation.

In the micromagnetic model, magnetization dynamics are affected by various energy terms. In addition to the Zeeman energy (contribution of the externally applied field)

$$U_{\mathrm{Z}} = -\mu_0 \boldsymbol{M} \cdot \boldsymbol{H}_{\text{app}}, \tag{2.2.5}$$

anisotropy, exchange, and demagnetization terms are typically considered. In Chapter 5, we will also introduce the magnetoelastic energy terms. All the terms in the Gibbs free energy density contribute to the effective field $\boldsymbol{H}_{\text{eff}}$ in the LL equation (2.2.1) and LLG equation (2.2.2). In the same manner as the virtual work principle in kinetics, this is derived using the variational derivative

$$\boldsymbol{H}_{\text{eff}} = -\frac{1}{\mu_0}\frac{\delta U}{\delta \boldsymbol{M}} \equiv -\frac{1}{\mu_0}\frac{\partial U}{\partial \boldsymbol{M}} + \sum_i \frac{\partial}{\partial x_i}\left[\frac{\partial U}{\left(\partial \boldsymbol{M}/\partial x_i\right)}\right]. \tag{2.2.6}$$

Below, we will discuss the most common micromagnetic energy terms and their contribution to $\boldsymbol{H}_{\text{eff}}$.

2.2.1 Exchange energy in micromagnetics

As seen in Eq. (2.1.19), the exchange energy among spins can be expressed as the inner product of neighboring spin vectors. For a small angle, the inner product in (2.1.19) is approximated as

$$\boldsymbol{S}_i \cdot \boldsymbol{S}_j \approx S^2 \cos\phi_{ij} \approx -\left|\phi_{ij}\right|^2 \approx -\left|\boldsymbol{m}_i - \boldsymbol{m}_j\right|^2, \tag{2.2.7}$$

where $\boldsymbol{m}$ is the unit vector parallel to the magnetization direction. Within the approximation of micromagnetics, $\boldsymbol{m}$ is defined not only at atomistic sites but for all space. It can be replaced with its Taylor expansion to the first order $\left|\boldsymbol{m}_i - \boldsymbol{m}_j\right| = \left|(\boldsymbol{s}_i \cdot \nabla)\boldsymbol{m}\right|$, where $\boldsymbol{s}_i$ is the position vector pointing from the lattice point i to j. The exchange energy then becomes

$$\mathcal{E}_{\mathrm{EX}} = JS^2 \sum_i \sum_{\boldsymbol{s}_i} \left[(\boldsymbol{s}_i \cdot \nabla)\boldsymbol{m}\right]^2. \tag{2.2.8}$$

By changing the summation over i to an integral

$$U_{\mathrm{EX}} = A_{\mathrm{EX}} \left[(\nabla m_x)^2 + (\nabla m_y)^2 + (\nabla m_z)^2\right] \tag{2.2.9}$$

with the *exchange constant* (or the *exchange stiffness constant*)

$$A_{\mathrm{EX}} = \frac{JS^2}{a} c, \tag{2.2.10}$$

where c = 1,2, and 4 for simple cubic, bcc and fcc crystals, respectively and

$$A_{\mathrm{EX}} = \frac{2\sqrt{2}JS^2}{a} \tag{2.2.11}$$

for close-packed hexagonal crystals. Substituting (2.2.9) into (2.2.6), the exchange contribution to $\boldsymbol{H}_{\mathrm{eff}}$ is

$$\boldsymbol{H}_{\mathrm{EX}} = \frac{2A_{\mathrm{EX}}}{\mu_0 M_{\mathrm{S}}} \nabla^2 \boldsymbol{m}. \tag{2.2.12}$$

2.2.2 Anisotropy

Ferromagnetic and ferrimagnetic materials typically favor magnetization in particular directions that reduce the total energy density. This originates, for example, from crystallographic structure, mechanical stress, and the interfacial effects. These effects are of local nature and to be distinguished from the demagnetization energy, also known as the shape anisotropy, determined by the macroscopic shape and magnetization of the sample as will be discussed below. Here, we treat it only phenomenologically. The most common forms of the anisotropy are uniaxial and cubic anisotropy. In the former case, the anisotropy energy density is phenomenologically modeled as the even power series of the sinusoidal functions of the magnetization angle, where odd numbers are ruled out due to azimuthal symmetry. In most cases, only the lowest order term is necessary and the uniaxial anisotropy is expressed as

$$U_{\mathrm{U}} = -K_1 \cos^2\theta = K_1(\boldsymbol{m}\cdot\boldsymbol{e})^2, \tag{2.2.13}$$

where θ is the angle of the magnetization direction with respect to the anisotropy axis. The uniaxial anisotropy is also expressed with the unit vector along the symmetry axis $\boldsymbol{e}$, in more general cases. In some cases, the second coefficient K_2 with $\cos^4\theta$ term is also used. A positive K_1 value means that the magnetization along the anisotropy axis is energetically favorable and it is called the easy axis. When $K_1 < 0$, $\boldsymbol{e}$ is the hard axis (the easy plane is perpendicular to $\boldsymbol{e}$). From Eq. (2.2.13), the uniaxial anisotropy energy contributes to the effective field as

$$\boldsymbol{H}_{\mathrm{U}} = \frac{2K_1}{\mu_0 M_{\mathrm{S}}}(\boldsymbol{m}\cdot\boldsymbol{e})\boldsymbol{e} = \boldsymbol{H}_{\mathrm{K}}(\boldsymbol{m}\cdot\boldsymbol{e})\boldsymbol{e}, \tag{2.2.14}$$

where $H_{\mathrm{K}} \equiv 2K_1/(\mu_0 M_{\mathrm{S}})$ is called the *anisotropy field*. It is sometimes used to specify the anisotropy in place of K_1.

In addition to the crystallographic directions, anisotropy energy terms may arise from interfaces and surfaces, due to the broken symmetry at the surfaces and modification of the wave function near the interfaces of two different materials. Phenomenologically, the energy density is often expressed in the form of Eq. (2.2.13) and the same mathematical treatment can be applied as the "effective" uniaxial anisotropy.

For cubic crystals, the symmetry about interchanging x, y, and z axes requires even powers of the magnetization. Since the lowest term $m_x^2 + m_y^2 + m_z^2 = 1$ is a constant, the cubic anisotropy energy density is expanded as

$$U_{\mathrm{C}} = K_1(m_y^2 m_z^2 + m_z^2 m_x^2 + m_x^2 m_y^2) + K_2 m_x^2 m_y^2 m_z^2 . \tag{2.2.15}$$

For $K_1 > 0$ (e.g., Fe), (100) directions are the easy axes, while for $K_1 < 0$ (e.g., Ni), the easy axes are along (111). Again, K_2 is often unnecessary and omitted.

2.2.3 Demagnetization

When a magnetic body is magnetized, an uncompensated dipole moment appears. This is seen as a virtual "magnetic charge" which generates an additional field inside and outside the magnetic body. This field, because it reduces the total local field inside a magnet, is called the *demagnetization field* $\boldsymbol{H}_{\mathrm{D}}$. It is convenient to obtain the scalar magnetostatic potential Φ_{D} as a solution of

$$\nabla^2 \Phi_{\mathrm{D}} = \nabla \cdot \boldsymbol{M} \tag{2.2.16}$$

with the boundary conditions

$$\Phi_{\mathrm{D,in}} - \Phi_{\mathrm{D,out}} = 0,\ \frac{\partial \Phi_{\mathrm{D,in}}}{\partial n} - \frac{\partial \Phi_{\mathrm{D,out}}}{\partial n} = \boldsymbol{M} \cdot \boldsymbol{n}\,, \tag{2.2.17}$$

where $\boldsymbol{n}$ is the unit vector along the outward surface normal. $\boldsymbol{H}_{\mathrm{D}}$ is obtained as

$$\boldsymbol{H}_{\mathrm{D}} = -\nabla \Phi_{\mathrm{D}}\,. \tag{2.2.18}$$

Eq. (2.2.16) can be understood as a Poisson equation with the volumetric and surface magnetic charges $\rho = -\nabla \cdot \boldsymbol{M}$ and $\sigma = \boldsymbol{n} \cdot \boldsymbol{M}$, artificially defined point charges originating from uncompensated magnetic moments. The solution for (2.2.16) is given by the integral of the Green function $G(\boldsymbol{r}, \boldsymbol{r}') = 1/(4\pi|\boldsymbol{r} - \boldsymbol{r}'|)$, as

$$\Phi_{\mathrm{D}} = \frac{1}{4\pi}\left(-\int_V \frac{\nabla' \cdot \boldsymbol{M}(\boldsymbol{r}')}{|\boldsymbol{r} - \boldsymbol{r}'|}\mathrm{d}V' + \int_S \frac{\boldsymbol{n} \cdot \boldsymbol{M}(\boldsymbol{r}')}{|\boldsymbol{r} - \boldsymbol{r}'|}\mathrm{d}S' \right), \tag{2.2.19}$$

resulting in

$$\boldsymbol{H}_{\mathrm{D}}(\boldsymbol{r}) = -\nabla \Phi_{\mathrm{D}}(\boldsymbol{r}) = \frac{1}{4\pi}\left[-\int_V \frac{(\boldsymbol{r} - \boldsymbol{r}')\rho(\boldsymbol{r}')}{|\boldsymbol{r} - \boldsymbol{r}'|^3}\mathrm{d}V' - \int_S \frac{(\boldsymbol{r} - \boldsymbol{r}')\sigma(\boldsymbol{r}')}{|\boldsymbol{r} - \boldsymbol{r}'|^3}\mathrm{d}S' \right]. \tag{2.2.20}$$

In the simple case of uniformly saturated magnets, the demagnetization field can be expressed with a single demagnetization tensor $\vec{\vec{N}}$ as

$$\boldsymbol{H}_{\mathrm{D}} = -\vec{\vec{N}}\boldsymbol{M}\,. \tag{2.2.21}$$

$\vec{\vec{N}}$ is solely determined by the macroscopic shape of the magnet. This condition holds either at sufficiently large external fields where the nonuniformity of the magnetization is negligible or in an ellipsoid. Infinite rods and films fall in the second category as its extremes. When the Cartesian coordinate is defined along the major

axes of the ellipsoids, $\vec{\vec{N}}$ is further reduced to a diagonal matrix. Table 2.1 shows elements of $\vec{\vec{N}}$ in some representative cases.

Shape	N_x	N_y	N_z
Sphere ($a = b = c$)	1/3	1/3	1/3
Prolate ellipsoid ($a = b$, $c > a$) [107]	$\frac{1-N_z}{2}$	$\frac{1-N_z}{2}$	$\frac{1}{p^2}\left[\frac{1}{2\xi}\ln\left(\frac{1+\xi}{1-\xi}\right)-1\right]$
Inifinite thin film ($a = b = \infty$, $c = +0$)	0	0	1
Infinite cylinder ($a = b = +0$, $c = \infty$)	1/2	1/2	0

Table 2.1. Demagnetization factors for representative ellipsoids whose surface is defined by $(x/a)^2 + (y/b)^2 + (z/c)^2 = 1$. $p \equiv c/a$, $\xi \equiv \sqrt{p^2 - 1}/p$. Numbers are in the SI unit system. In CGS unit, the values of N_x, N_y, and N_z must be multiplied by 4π.

Once the demagnetization field $\boldsymbol{H}_\mathrm{D}$ is evaluated, either by Eq. (2.2.19)–(2.2.20) for a general case or by (2.2.21) for a uniformly saturated magnet, the demagnetization contribution to the free energy density can be evaluated as

$$U_\mathrm{D} = -\frac{1}{2}\mu_0 \boldsymbol{M} \cdot \boldsymbol{H}_\mathrm{D}, \tag{2.2.22}$$

where the factor of one half is necessary to avoid double counting of the interaction between two dipoles.

In nanostructured devices, the shape frequently deviates from an ellipsoid and nonuniform demagnetization needs to be evaluated numerically. Unlike the local

functions seen in exchange (2.2.12) and anisotropy (2.2.14) fields, the long range nature of Eq. (2.2.20) makes its evaluation challenging. More details will be discussed in section 2.3.

2.2.4 Kittel mode

As a representative example depicting magnetization precession, we will derive the ferromagnetic resonance mode in an infinite film. The discussion was derived and generalized in [108 pp. 35–37]. We assume a small Gilbert damping parameter α. The LLG equation (2.2.2) ensures the conservation of M and the equation of motion is replaced by two variables in spherical coordinates as

$$\frac{\partial \theta}{\partial t} = -\frac{\gamma}{\mu_0 M_S \sin\theta}\frac{\partial U}{\partial \varphi} - \frac{\alpha\gamma}{\mu_0 M_S}\frac{\partial U}{\partial \theta}$$

$$\frac{\partial \varphi}{\partial t} = \frac{\gamma}{\mu_0 M_S \sin\theta}\frac{\partial U}{\partial \theta} - \frac{\alpha\gamma}{\mu_0 M_S \sin^2\theta}\frac{\partial U}{\partial \varphi}, \tag{2.2.23}$$

where θ and φ are the polar and azimuthal angles of $\boldsymbol{M}$, respectively. First, the equilibrium direction θ_0 and φ_0 are obtained by solving

$$\left(\frac{\partial U}{\partial \theta}\right)\Big|_{\theta=\theta_0,\varphi=\varphi_0} = 0, \left(\frac{\partial U}{\partial \varphi}\right)\Big|_{\theta=\theta_0,\varphi=\varphi_0} = 0. \tag{2.2.24}$$

By substituting the uniaxial anisotropy energy $U_U = K_1 \sin^2\theta$ (2.2.13), demagnetization energy $U_D = \mu_0 M_S^2 \cos 2\theta / 4$ (2.2.21), and the Zeeman energy

$$U_Z = -\mu_0 M H_{app}\left[\cos\theta\cos\theta_H + \sin\theta\sin\theta_H\cos(\varphi-\varphi_H)\right], \tag{2.2.25}$$

(2.2.24) becomes a transcendent equation

$$\left(K_1 - \frac{\mu_0 M_S^2}{2}\right)\sin 2\theta_0 - \mu_0 M_S H_{app}\sin(\theta_H - \theta_0) = 0\,, \tag{2.2.26}$$

where θ_H specifies the direction of the external field $\boldsymbol{H}_{app}$. The equilibrium magnetization direction θ_0 is obtained as a numerical solution of (2.2.26). Substituting small deviation of the magnetization angles $\theta = \theta_0 + \delta\theta\exp(i\omega t)$ and $\varphi = \varphi_0 + \delta\varphi\exp(i\omega t)$ into (2.2.23),

$$\left(i\omega + \frac{\gamma}{\mu_0 M_S \sin\theta_0}U_{\theta\varphi} + \frac{\alpha\gamma}{\mu_0 M_S}U_{\theta\theta}\right)\delta\theta + \left(\frac{\gamma}{\mu_0 M_S \sin\theta_0}U_{\varphi\varphi} + \frac{\alpha\gamma}{\mu_0 M_S}U_{\theta\varphi}\right)\delta\varphi = 0$$

$$\left(i\omega - \frac{\gamma}{\mu_0 M_S \sin\theta_0}U_{\theta\varphi} + \frac{\alpha\gamma}{\mu_0 M_S \sin^2\theta_0}U_{\varphi\varphi}\right)\delta\varphi$$

$$-\left(\frac{\gamma}{\mu_0 M_S \sin\theta_0}U_{\theta\theta} - \frac{\alpha\gamma}{\mu_0 M_S \sin^2\theta_0}U_{\theta\varphi}\right)\delta\theta = 0\,, \tag{2.2.27}$$

where

$$U_{\theta\theta} = \left(\frac{\partial^2 U}{\partial\theta^2}\right)\Bigg|_{\theta=\theta_0,\varphi=\varphi_0} = 2\left(K_1 - \frac{\mu_0 M_S^2}{2}\right)\cos 2\theta_0 + \mu_0 M_S H_{app}\cos\left(\theta_H - \theta_0\right)$$

$$U_{\theta\varphi} = \left(\frac{\partial^2 U}{\partial\theta\partial\varphi}\right)\Bigg|_{\theta=\theta_0,\varphi=\varphi_0} = 0$$

$$U_{\varphi\varphi} = \left(\frac{\partial^2 U}{\partial\varphi^2}\right)\Bigg|_{\theta=\theta_0,\varphi=\varphi_0} = \mu_0 M_S H_{app}\sin\theta_0\sin\theta_H\,. \tag{2.2.28}$$

For Eq. (2.2.27) to have a nontrivial solution, the determinant of the coefficients must be 0 (compatibility condition). With α = 0, this condition yields the ferromagnetic resonance frequency

$$\omega_0 = \frac{\gamma}{\mu_0 M_S \sin\theta_0}\sqrt{U_{\theta\theta}U_{\varphi\varphi} - U_{\theta\varphi}^2}$$

$$= \gamma\sqrt{H_1 H_2}\,, \tag{2.2.29}$$

where

$$H_1 = H_{app}\cos(\theta_0 - \theta_H) + \left(\frac{2K_1}{\mu_0 M_S} - M_S\right)\cos 2\theta_0$$

$$H_2 = H_{app}\cos(\theta_0 - \theta_H) + \left(\frac{2K_1}{\mu_0 M_S} - M_S\right)\cos^2\theta_0\,. \tag{2.2.30}$$

Eq. (2.2.29) is used to model the ferromagnetic resonance (Kittel mode) frequency in unpatterned films. When $\boldsymbol{H}_{app}$ is applied perpendicular or parallel to the film ($\theta_0 = \theta_H = 0$ or $\theta_0 = \theta_H = 2\pi$) H_1 and H_2 become identical and the precession frequency linearly depends on H_{app} with the proportional constant of γ. When the field is canted, Eq. (2.2.26) and (2.2.29) need to be numerically evaluated. In Chapter 4, a fit of observed frequency with (2.2.29) is used to obtain the material parameters such as γ, M_S, and K_1.

2.3 Numerical techniques for magnetic modeling

The micromagnetic analysis was first applied to limited geometries (e.g., ellipsoids, where the demagnetization field is uniform in the body). With the development of the easily available computational resources and numerical techniques in 1980s, magnetic simulations have become a widely used tool for studying the behaviors of micro- and nanoscale magnetic structures [109–118].

In most numerical micromagnetic simulations today, the finite-difference time domain (FDTD) method is utilized for time integration of the LL equation (2.2.3). The simulated body is spatially discretized either with the finite difference method (FDM) or the finite element method (FEM). The effective field $\boldsymbol{H}_{\text{eff}}$ (2.2.6) is evaluated for each time step, taking into account Zeeman, exchange, anisotropy, and demagnetization field. The magnetization evolution after a small time step is evaluated with a Runge-Kutta method (e.g., Euler method or another higher-order member in the family of Runge-Kutta methods). The Zeeman, exchange, and anisotropy fields are locally defined and can easily be evaluated with standard FDM or FEM. The demagnetization field, due to its long-range character, is the most computationally intense part of micromagnetic simulations. Various numerical methods have been developed. Here, we review the concepts of two most commonly used techniques for evaluation of $\boldsymbol{H}_{\text{D}}$ in the FDM and FEM.

For the finite difference space discretization, as used for OOMMF [119] and MuMax3 [120], the simulated body is split into cuboid cells. The distribution of $\boldsymbol{M}$ is approximated by an aggregate of magnetic moments with the magnitude of $\boldsymbol{\mu}_i = \boldsymbol{M}V$ at the center of each cell, where V is the volume of each cuboid. The demagnetization field $\boldsymbol{H}_{\text{D},i}$ at the center of the cell i is given by the summation of the dipole fields from the other cells $j \neq i$ as

$$\boldsymbol{H}_{\text{D},i} = \frac{1}{\mu_0 4\pi} \sum_{j \neq i} \left(\frac{3\boldsymbol{r}_{ij}(\boldsymbol{\mu}_j \cdot \boldsymbol{r}_{ij})}{r_{ij}^5} + \frac{\boldsymbol{\mu}_i}{r_{ij}^3} \right). \tag{2.3.1}$$

This can be rewritten as

$$\boldsymbol{H}_{\mathrm{D},i}^{\alpha} = \frac{1}{\mu_0 4\pi} \sum_{\beta} \sum_{j \neq i} W_{ij}^{\alpha\beta} \mu_j^{\beta} \tag{2.3.2}$$

with the interaction matrices $W_{ij}^{\alpha\beta}$, where $\alpha, \beta = x, y, z$. $W_{ij}^{\alpha\beta}$ is determined solely by the geometry and has only to be evaluated once. Direct evaluation of (2.3.1) suffers the complexity of $\mathcal{O}(N^2)$, where N is the number of the cells. Eq. (2.3.2) is in the form of discrete convolution and can be efficiently evaluated with the Fast Fourier transform (FFT) and multiplication in the k-space [113–116]. The final $\boldsymbol{H}_{\mathrm{D},i}$ is obtained with the inverse FFT. The FFT and inverse FFT limit the complexity of the total process, reducing it to $\mathcal{O}(N \log N)$. The efficient evaluation of $\boldsymbol{H}_{\mathrm{D}}$ is the advantage of the FDM and is part of the reason it was popular in the micromagnetic community, despite its apparent disadvantages of regular meshing and step-wise edges.

For the FEM approach, the simulation structure typically is discretized with a tetrahedron mesh. The partial differential equation is transformed into a series of linear algebraic equations with the Galerkin method [112]. The scalar magnetic potential Φ_{D} is first obtained as a solution of the Poisson equation (2.2.16) and $\boldsymbol{H}_{\mathrm{D}}$ is evaluated with (2.2.18). With the boundary conditions (2.2.17), evaluation of Φ_{D} requires meshing of the space outside the magnet of interest, typically with ~5 times as large dimension [117]. The hybrid finite element/boundary element (FE/ME) method [118] eliminates the need to model a large outer space and is commonly used today by FE micromagnetic simulators, such as Magpar [121] and NMag [122]. It splits the magnetic scalar potential into two parts $\Phi_{\mathrm{D}} = \Phi_{\mathrm{D1}} + \Phi_{\mathrm{D2}}$ where Φ_{D1} obeys

the Poisson equation (2.2.16) inside the magnet and is defined 0 outside with the Neumann boundary condition. Φ_{D2} is taken to make the whole potential Φ_D to meet the boundary condition (2.2.17). Now Φ_{D1} can be evaluated with the standard FEM without meshing the space outside the magnet and Φ_{D2} is directly evaluated from Φ_{D1} with the boundary method

$$\Phi_{D2}(\boldsymbol{r}) = \frac{1}{4\pi}\int_S \frac{\Phi_{D2}(\boldsymbol{r}')(\boldsymbol{r}-\boldsymbol{r}')}{|\boldsymbol{r}-\boldsymbol{r}'|}\mathrm{d}\boldsymbol{r}' . \tag{2.3.3}$$

On the boundary nodes, $\Phi_{D2} = B\Phi_{D1}$ is calculated with a $N \times N$ dense matrix B, where N is the number of boundary nodes. The memory requirement for B scales quadratically with N, hence biquadratically with the size of the simulated structure. Especially with thin film structures frequently encountered in micromagnetics, B often limits the simulation size. Recently, hierarchical matrices were used to compress B into a set of sparse matrices with a given approximation error [123,124], alleviating this disadvantage over the FDM.

3. Measurement methods

In this chapter, we will review the principles and measurement/analysis techniques of the magnetization detection with optical method. First, the origin of the light-spin interaction—magneto-optic effect is introduced in Lorentz and electromagnetic models. The magneto-optic effect is then combined with synchronized magnetization excitation to achieve the time resolution. The actual time-resolved magneto-optic Kerr effect microscopy system utilized for the study in this paper is described in section 3.3. Lastly, some analysis tools for interpreting the experimental result are briefly described at the end of this chapter.

3.1 Magneto-optic effect

As light travels through or gets reflected from a material under a magnetic field or with magnetic order, its polarization changes its direction and the ellipticity. The phenomenon is generally termed as the magneto-optic effects and has been used as a probe of spin orientation in materials. This section describes the two most common types of such effects—the Faraday effect and the magneto-optic Kerr effect (MOKE). In these cases, the polarization of the incident light is altered by the presence of the magnetization or the magnetic field, as the light goes through the material (Faraday effect) or gets reflected upon (MOKE). Another type of magneto-optic effects (the Cotton-Mouton effect or Voigt effect) is not covered here, as it has much smaller effect comparing to MOKE and is less frequently used for magnetization detection.

The first demonstration of the magneto-optic effect was reported by M. Faraday in 1846 [125]. As depicted in Fig. 3.1, when a linearly polarized light travels through a transparent material with a nonzero Verdet constant V under the presence of a magnetic field, the transmitted light undergoes rotation in the polarization angle and originally linear polarization becomes elliptic. The effect was named after its discoverer as the Faraday effect and is sometimes called the magnetic circular dichroism as well. To characterize the strength of this effect, the Faraday rotation θ_F is defined as the change in light polarization angle after having traveled through the medium. Conventionally, its sign is defines as in Fig. 3.1. In a right-hand coordinate system with a light wave vector $\boldsymbol{k}$ and a magnetic flux density $\boldsymbol{B}$ along the z direction, a positive θ_F corresponds to an increase in the azimuthal angle of the polarization direction. The polarization of the transmitted light becomes elliptic and the Faraday ellipticity η_F is defined as the ratio of the major and minor polarization amplitude. The Faraday rotation θ_F and Faraday ellipticity η_F is combined as the complex Faraday rotation

$$\tilde{\theta}_F = \theta_F - i\eta_F . \tag{3.1.1}$$

Experimentally, the complex Faraday rotation was found to be proportional to the length d of the medium and the magnitude of the externally applied magnetic field as

$$\tilde{\theta}_F = VBd\cos\alpha , \tag{3.1.2}$$

where α is the angle between $\boldsymbol{B}$ and the direction of light propagation. The Verdet constant V is a material-specific coefficient depending on the wavelength. In a

magnetically ordered material, it depends on the magnetization rather than the external field. Any dichroism effects unrelated to magnetic properties also lead to rotation of the transmitted light. The Faraday effect, however, has a unique nonreciprocal character: the rotation direction is a function of both the magnetic field and the light propagation direction. When the light goes through a Faraday medium, gets reflected, and travels through the same medium in the opposite direction, the light polarization experiences further rotation, whereas in other normal circular dichroism, the light polarization gets reversed to its original state.

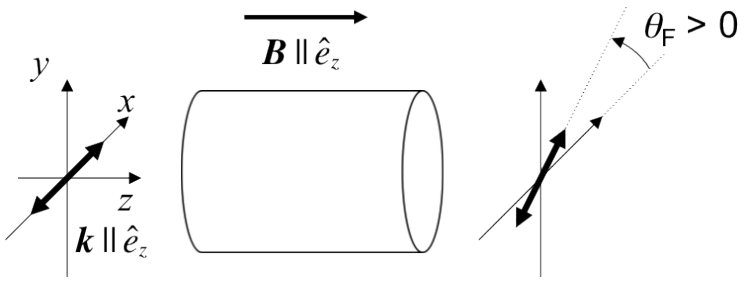

Fig. 3.1. Sketch of the Faraday rotation. With the magnetic flux densty $\boldsymbol{B}$ and wave vector $\boldsymbol{k}$ along the z direction, the positive Faraday rotation θ_F is defined as in the figure. The Faraday ellipticity is neglected in this sketch.

Similar polarization change is observed upon reflection off a magnetized material and the effect is called the magneto-optic Kerr effect (MOKE). This should not be confused with the electro-optic Kerr effect (or simply the Kerr effect) which describes the nonlinear dependence of the refractive index on the electric field. Similar to the complex Faraday rotation, the Kerr rotation θ_K and the Kerr ellipticity

η_K are defined as the change in light polarization direction and the ellipticity. The two can be expressed as a complex Kerr rotation

$$\tilde{\theta}_K = \theta_K - i\eta_K . \quad (3.1.3)$$

Fig. 3.2 depicts representative experimental geometries, defined by the magnetization direction in regard to the sample surface and the plane of incidence. Magnetization perpendicular to the sample surface (Fig. 3.2a) is called the polar configuration. When the magnetization is parallel to the surface and the plane of incidence (Fig. 3.2b), it is called the longitudinal MOKE and when the magnetization is parallel to the surface but perpendicular to the plane of incidence (Fig. 3.2c), it is called the transverse MOKE. The observed Kerr rotation depends on the experimental geometry. For example, when the incident angle is small, the polar MOKE is linear in *M* while the longitudinal MOKE is quadratic in *M* [126 pp.480–481]. The transverse MOKE exhibits no Kerr rotation but Kerr ellipticity. When the magnetization is oriented along an intermediate direction among these configurations, the polarization of the reflected light exhibits the mixture of polar, longitudinal, and transverse MOKE.

Phenomenologically, both in the Faraday effect and MOKE, the modulation of the light polarization is understood as the differential dielectric constant for right-hand circularly polarized (RCP) and left-hand circularly polarized (LCP) light. The RCP and LCP light experience different reflection, absorption, and refractive indices, depending on the magnetization of the material or the magnetic field. Any light polarization is decomposed as a summation of RCP and LCP components that

experience different rate of reflection, absorption, and retardation. The reflected or transmitted light is expressed as the summation of the two polarizations, having experienced different modulation, and exhibits the change in polarization angle and ellipticity.

In section 3.1.1, we will discuss a semiclassical explanation of the origin of such effect using a Lorentz model. In section 3.1.2, the magneto-optic effect is related to the off-diagonal elements of the dielectric tensor of the material.

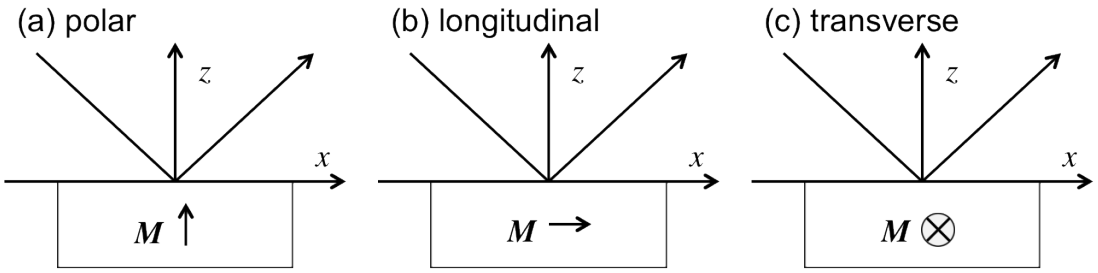

Fig. 3.2. Magneto-optic Kerr geometries.

3.1.1 Lorentz model of complex dielectric tensor

A semiclassical model of light dispersion in the presence of magnetic field was developed by H. A. Lorentz [127]. This gives a qualitative explanation of the origin of magneto-optic effects, namely the off-diagonal elements in the dielectric tensor depending on the magnetic field. Following discussion in [126 pp. 481–486], the atomistic Lorentz oscillator model of dispersion under a magnetic field is reviewed below. In the Lorentz model, an electron is modeled as a classical mass

point obeying Hooke's law in a quadratic potential well around an atom site. The electron experiences the electrostatic and Lorentz forces with the damping term $\gamma\dot{\vec{r}}$. With sinusoidal electric field $\boldsymbol{E}$ of the light and a constant magnetic field $\boldsymbol{B}$ along the z axis, the equation of motion reads

$$\ddot{\vec{r}} + \gamma\dot{\vec{r}} + \omega_0^2\vec{r} = \frac{e}{m}\vec{E}\exp\left(i(\omega t - kz)\right) + \omega_c\dot{\vec{r}} \times \hat{e}_z, \tag{3.1.4}$$

where e is the electron charge, m is the free electron mass, $\omega_0 = \kappa/m$ is the mechanical resonant frequency, $\omega_c = eB/mc$ is the cyclotron frequency, and $\hat{e}_i$ for $i = x, y, z$ is unit vectors along the Cartesian axes. Since $e < 0$, the sign of ω_c is negative in this definition. Here, the light is propagating along the z axis and the electric field is in the xy plane.

As the right hand side of (3.1.4) shows, the driving force to the system is only in xy plane and E_x and E_y are coupled to each other. The stationary solution can be conveniently expressed with the basis of circularly polarization

$$\hat{e}_\pm = \frac{1}{\sqrt{2}}(\hat{e}_x \pm i\hat{e}_y) \tag{3.1.5}$$

and one can solve for the two circularly polarized planar waves propagating along z. The + and – in the subscript correspond to the RCP and LCP light. Assuming the solution in the form of

$$\vec{r}_\pm = \vec{r}_{0\pm}\hat{e}_\pm = \tilde{A}_\pm\vec{E}_\pm \tag{3.1.6}$$

with the complex oscillation amplitude $\tilde{A}_\pm$, and $\vec{E}_\pm = E_{0\pm}\exp\left(i(\omega t - kz)\right)\hat{e}_\pm$. By substituting (3.1.6) into (3.1.4),

$$\tilde{A}_{\pm}\vec{E}_{0\pm}(-\omega^2 + i\gamma\omega + \omega_0^2) = \frac{e}{m}\vec{E}_{0\pm}\hat{e}_{\pm} \pm i\omega\omega_c\tilde{A}_{\pm}\vec{E}_{0\pm}\hat{e}_{\pm} \times \hat{e}_z . \tag{3.1.7}$$

Solving for the oscillation amplitude,

$$\tilde{A}_{\pm} = \frac{e}{m(\omega_0^2 - \omega^2 \pm \omega\omega_c + i\gamma\omega)} . \tag{3.1.8}$$

The macroscopic polarization is obtained with the atomic concentration of the electrons per unit volume N as

$$\vec{P}_{\pm} = \tilde{\alpha}_{\pm}\vec{E}_{\pm} = Ne\vec{r}_{\pm} = Ne\tilde{A}_{\pm}\vec{E}_{\pm} , \tag{3.1.9}$$

where $\tilde{\alpha}_{\pm}$ is the polarizability of the electron for each helicity. This gives the dielectric constant (in CGS unit)

$$\tilde{\varepsilon}_{\pm} = \tilde{\varepsilon}'_{\pm} + i\tilde{\varepsilon}''_{\pm} = 1 + 4\pi\tilde{\alpha}_{\pm} = 1 + \frac{4\pi Ne^2}{m}\frac{1}{\omega_0^2 - \omega^2 \pm \omega\omega_c + i\omega\gamma} \tag{3.1.10}$$

whose real and imaginary parts lead to the refraction and absorption. Comparing (3.1.10) to the standard results in the absence of the magnetic field, the resonant frequency ω_0 has been shifted by a quantity depending on the magnetic field B. The shift in resonant frequency $\omega_{0\pm}$ satisfies

$$\omega_0^2 - \omega_{0\pm}^2 \pm \omega_{0\pm}\omega_c = 0 \tag{3.1.11}$$

and is obtained as

$$\omega_{0\pm} - \omega_0 = \pm\frac{1}{2}\omega_c = \pm\omega_L , \tag{3.1.12}$$

where an approximation $\omega_0^2 - \omega_{0\pm}^2 \approx 2\omega_{0\pm}(\omega_{0\pm} - \omega_0)$ has been applied. ω_L is the Larmor frequency. Since $\omega_c = eB/mc$ has a negative sign with $e < 0$, Eq. (3.1.12) leads to a relation

$$\omega_{0+} < \omega_0 < \omega_{0-} . \tag{3.1.13}$$

Therefore, when $\left|\omega_{0+} - \omega_{0-}\right| << \omega_0$, the shape of the energy dispersion of the index of refraction does not change its form but simply shift along the ω axis by $\mp\omega_c$. Hence, in the region of normal dispersion $\partial n/\partial\omega > 0$,

$$n_+(\omega) > n_-(\omega) . \tag{3.1.14}$$

As a light travels through this medium, the RCP light is more retarded than the LCP light, leading to the positive Faraday rotation ($\theta_F > 0$).

3.1.2 Macroscopic dielectric tensors

As demonstrated in the previous section, the shift in the resonance frequency induced by the magnetic field causes circular dichroism in optical properties. In this section, we relate this circular dichroism to the off-diagonal elements in the dielectric tensor and will show that it describes the magneto-optic effects.

We assume that the incident light is propagating along the z axis. The dielectric tensor of the material has the off-diagonal component

$$\tilde{\boldsymbol{\varepsilon}} = \begin{pmatrix} \tilde{\varepsilon}_{11} & \tilde{\varepsilon}_{12} & 0 \\ \tilde{\varepsilon}_{21} & \tilde{\varepsilon}_{22} & 0 \\ 0 & 0 & \tilde{\varepsilon}_{33} \end{pmatrix}, \tag{3.1.15}$$

assuming the intrinsic property in x and y direction. As discussed in section 3.1.1, it is convenient to handle the problem in another basis of right- and left-hand circular polarization. With the transformation matrix

$$T = \frac{1}{\sqrt{2}}\begin{pmatrix} 1 & 1 & 0 \\ i & -i & 0 \\ 0 & 0 & \sqrt{2} \end{pmatrix}, \quad T^{-1} = \frac{1}{\sqrt{2}}\begin{pmatrix} 1 & -i & 0 \\ 1 & i & 0 \\ 0 & 0 & \sqrt{2} \end{pmatrix}, \tag{3.1.16}$$

the problem can be transformed from the Cartesian basis to the circularly polarization as

$$\tilde{\boldsymbol{\varepsilon}} = \boldsymbol{T}\tilde{\boldsymbol{\varepsilon}}_{\pm}\boldsymbol{T}^{-1}, \tag{3.1.17}$$

where

$$\tilde{\boldsymbol{\varepsilon}}_{\pm} = \begin{pmatrix} \tilde{\varepsilon}_{+} & 0 & 0 \\ 0 & \tilde{\varepsilon}_{-} & 0 \\ 0 & 0 & \tilde{\varepsilon}_{33} \end{pmatrix}. \tag{3.1.18}$$

By substituting (3.1.16) and (3.1.18) to (3.1.17), the components of (3.1.15) becomes

$$\tilde{\varepsilon}_{11} = \frac{1}{2}(\tilde{\varepsilon}_{+} + \tilde{\varepsilon}_{-}), \tag{3.1.19}$$

$$\tilde{\varepsilon}_{21} = i(\tilde{\varepsilon}_{+} - \tilde{\varepsilon}_{-}) = -\tilde{\varepsilon}_{12}. \tag{3.1.20}$$

Therefore, the dielectric tensor has the form of

$$\tilde{\boldsymbol{\varepsilon}} = \begin{pmatrix} \tilde{\varepsilon}_{11} & \tilde{\varepsilon}_{12} & 0 \\ -\tilde{\varepsilon}_{12} & \tilde{\varepsilon}_{11} & 0 \\ 0 & 0 & \tilde{\varepsilon}_{33} \end{pmatrix} \tag{3.1.21}$$

and can be expressed with only three components $\tilde{\boldsymbol{\varepsilon}}_{11}$, $\tilde{\boldsymbol{\varepsilon}}_{33}$, and $\tilde{\boldsymbol{\varepsilon}}_{12}$. It further reduces to $\tilde{\varepsilon}_{33} = \tilde{\varepsilon}_{11}$ in an isotropic medium as in a frequently encountered situation.

Similarly, the index of refraction in a magnetized medium or in a magnetic field becomes a tensor with non-zero off-diagonal element.

$$\tilde{\boldsymbol{n}} = \begin{pmatrix} \tilde{n}_{11} & \tilde{n}_{12} & 0 \\ -\tilde{n}_{12} & \tilde{n}_{11} & 0 \\ 0 & 0 & \tilde{n}_{33} \end{pmatrix} \text{ or } \tilde{\boldsymbol{n}}_{\pm} = \begin{pmatrix} \tilde{n}_{+} & 0 & 0 \\ 0 & \tilde{n}_{-} & 0 \\ 0 & 0 & \tilde{n}_{33} \end{pmatrix}, \tag{3.1.22}$$

where

$$n_{\pm}^2 = \varepsilon_{11} \pm i\varepsilon_{12} \tag{3.1.23}$$

and

$$\tilde{n}_{11} = \frac{1}{2}(\tilde{n}_{+} + \tilde{n}_{-})$$

$$\tilde{n}_{12} = -i(\tilde{n}_{+} - \tilde{n}_{-}). \tag{3.1.24}$$

When the RCP and LCP light goes through the medium or gets reflected from the interface, the polarization of the reflected or transmitted light is expressed by Snell's law with the refractive index n_{+} and n_{-}, as in the normal incidence

$$\tilde{r}_{\pm} = \frac{\tilde{n}_{\pm} - 1}{\tilde{n}_{\pm} + 1}. \tag{3.1.25}.$$

After traveling through a medium of thickness d, the amplitude of RCP and LCP light becomes modulated. The total transmitted light is the sum of these two components. The complex Faraday rotation is

$$\tilde{\theta}_{\mathrm{F}} = \theta_{\mathrm{F}} - i\eta_{\mathrm{F}} = \frac{\omega d}{2c}(\tilde{n}_{+} - \tilde{n}_{-}). \tag{3.1.26}$$

The complex Kerr rotation of the reflected light is obtained with a similar treatment. The complex reflection coefficient is expressed in a phasor expression $\tilde{r}_{\pm} = r_{\pm}\exp(i\phi_{\pm})$ and the polar Kerr rotation and the ellipticity are given as

$$\theta_{\mathrm{K}} = -\frac{\phi_{+} - \phi_{-}}{2}$$

$$\tan\eta_{\mathrm{K}} = -\frac{r_+ - r_-}{r_+ + r_-}. \tag{3.1.27}$$

For small Kerr rotation $|\theta_{\mathrm{K}}| << 1,\ |\phi_{\mathrm{K}}| << 1$,

$$\tilde{\theta}_{\mathrm{K}} \approx i\frac{\tilde{r}_+ - \tilde{r}_-}{\tilde{r}_+ + \tilde{r}_-} \approx i\frac{\tilde{n}_+^2 - \tilde{n}_-^2}{2\tilde{n}_{11}(\tilde{n}_{11}^2 - 1)}. \tag{3.1.28}$$

When the above condition $|\theta_{\mathrm{K}}|, |\phi_{\mathrm{K}}| << 1$ does not hold, the exact solution of (3.1.27) can be obtained as a solution of the transcendent equation [126 p. 485]

$$\frac{\sin(2\theta_{\mathrm{K}})\cos(2\eta_{\mathrm{K}})}{1+\cos(2\theta_{\mathrm{K}})\sin(2\eta_{\mathrm{K}})} - i\frac{\sin(2\eta_{\mathrm{K}})}{1+\cos(2\theta_{\mathrm{K}})\sin(2\eta_{\mathrm{K}})} = i\frac{\tilde{r}_+ - \tilde{r}_-}{\tilde{r}_+ + \tilde{r}_-}. \tag{3.1.29}$$

In experiments, these effects are phenomenologically quantified with the magneto-optic coefficient q defined as

$$\tilde{\boldsymbol{\varepsilon}} = n_{11}^2 \begin{pmatrix} 1 & iq & 0 \\ -iq & 1 & 0 \\ 0 & 0 & 1 \end{pmatrix}. \tag{3.1.30}$$

q can be experimentally found. For representative ferromagnet such as nickel and iron, from the MOKE contrast, q is in the order of 10^{-2} [128]. The above derivation assumed normal incidence of light and the magnetization or the external magnetic field perpendicular to the sample surface. For an arbitrary magnetization orientation and incidence angle, the dielectric tensor is derived as [129]

$$\tilde{\boldsymbol{\varepsilon}} = n_{11}^2 \begin{pmatrix} 1 & iq\cos\theta & -iq\sin\varphi\cos\theta \\ -iq\cos\theta & 1 & iq\cos\varphi\sin\theta \\ iq\sin\varphi\cos\theta & -iq\cos\varphi\sin\theta & 1 \end{pmatrix}, \tag{3.1.31}$$

where θ and φ are the polar and azimuthal angles of the magnetization $\boldsymbol{M}$, respectively, with the z direction defined as the normal direction of the plane surface.

3.2 Principles of time-resolved magneto-optic Kerr effect

3.2.1 Magnetization perturbation schemes

For dynamic measurement of magnetization evolution, the MOKE measurement principles described in the previous section are combined with synchronized excitation and detection. Generally, in dynamic MOKE measurement, the spin system is excited and its subsequent evolution, governed by LLG equation (2.2.2) is probed at some time delay. Multiple excitation schemes have been developed. Pulsed or modulated magnetic field application, laser heating, spin-selective excitation with polarized light, and elastic strain pulses will be discussed below.

The first excitation scheme is typically implemented with a coplanar waveguide (CPW) and a photoconductive switch (PCS) [65,130–135]. Fig. 3.3 shows a representative schematic of such experimental design. The sample magnets are fabricated directly on or by the CPW and its magnetization is perturbed by the pulsed field generated by flowing a pulsed current through the CPW. The pump laser pulse is focused on the PCS and excites conduction electrons in the PCS substrate, creating a current surge through the impedance-matched CPW.

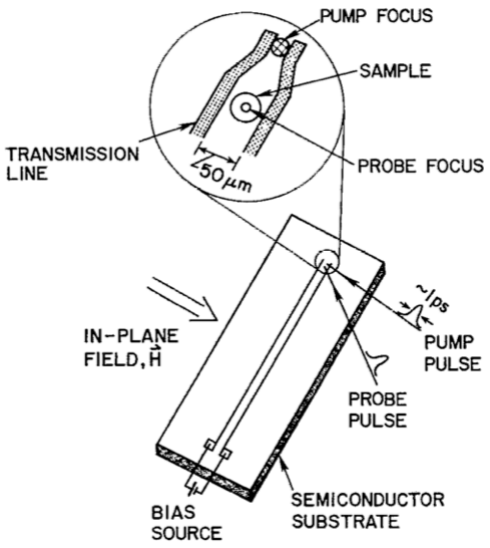

Fig. 3.3. A schematic diagram of pulse field application using a photoconductive switch. A pump pulse is focused on a photoconductive switch, creating a current surge through the transmission line. The transient magnetic field perturbs the magnetization and free precession motion is probed with a time-delayed probe beam. Taken from [130].

The second scheme is less restricted in sample preparation and will be mainly utilized for the experimental work in this thesis. A femtosecond laser pulse is focused on a magnetic sample and excites a part of the conduction electrons by several electron volts on a subpicosecond time scale. The excited "hot electrons" are then thermalized and coupled with the lattice and spin system in sub- to tens of picosecond time scale. Beaurepaire *et al* [136] first reported the ultrafast demagnetization in nickel using 60 fs laser pulses and it has been a field of intense study. Due to the highly nonequilibrium state during this process, the exact mechanism of

magnetization perturbation has still been an active debate [137–141]. Beaurepaire *et al*, however, successfully modeled the process with a phenomenological three-temperature model. This is now commonly used for interpreting TR-MOKE measurements.

The three-temperature model assumes three different heat baths—electron, lattice, and spin systems. Each heat bath has specific heat and is coupled with each other with a given coupling coefficient g_{ij}. The laser pulse excites the electron system and the energy of the hot electron gets redistributed to the other two systems. The model is expressed with a set of three coupled rate equations

$$C_{\mathrm{e}}\left(T_{\mathrm{e}}\right)\frac{\partial T_{\mathrm{e}}}{\partial t}=\frac{\partial}{\partial t}\left(\kappa\frac{\partial T_{\mathrm{e}}}{\partial z}\right)+\frac{1}{\zeta}S\left(t\right)e^{-\frac{z}{\zeta}}-g_{\mathrm{el}}\left(T_{\mathrm{e}}-T_{\mathrm{l}}\right)-g_{\mathrm{es}}\left(T_{\mathrm{e}}-T_{\mathrm{s}}\right)$$

$$C_{\mathrm{l}}\left(T_{\mathrm{l}}\right)\frac{\partial T_{\mathrm{l}}}{\partial t}=-g_{\mathrm{el}}\left(T_{\mathrm{l}}-T_{\mathrm{e}}\right)-g_{\mathrm{ls}}\left(T_{\mathrm{l}}-T_{\mathrm{s}}\right)$$

$$C_{\mathrm{s}}\left(T_{\mathrm{s}}\right)\frac{\partial T_{\mathrm{s}}}{\partial t}=-g_{\mathrm{es}}\left(T_{\mathrm{s}}-T_{\mathrm{e}}\right)-g_{\mathrm{ls}}\left(T_{\mathrm{s}}-T_{l}\right), \qquad (3.2.1)$$

where C_i is the specific heat, g_{ij} is the coupling coefficients, κ is the electron heat conductance, and the indices i, j = e, l, s denote electron, lattice, and spin systems. The heat transfer in space is only modeled in the electron system. The second term in the first equation in (3.2.1) is the absorbed energy density per unit time induced by the laser pump pulse. $S(t)$ is the absorbed pump pulse fluence per unit time and $\zeta=\lambda/4\pi k$ is the skin depth of the excitation laser pulse. For nickel and cobalt, for example, it is 13.5 and 10.6 nm, respectively, at the wavelength of 400 nm [142].

Fig. 3.4 shows an example of numerical calculation. (3.2.1) was numerically integrated with the explicit Euler method using the parameters listed in Table 3.1. The pump laser pulse with a Gaussian shape has the peak fluence of 1.7 mJ/cm^2 and the full width half maximum (FWHM) of 200 fs. The electron temperature rises with a femtosecond time scale and the energy is subsequently redistributed to the other two subsystems. After 20 ps, the three temperatures have approximately identical values and the thermal energy in the system can be described with a single rate equation of the heat dissipation. This process evolves with two different time scales. First, the rapid excitation and thermalization of the hot electrons happen in the first picosecond [136]. The hot electrons thermalize with the other two heat baths in the subsequent picosecond time scale. The elevated lattice and spin temperatures go back to the original level in much slower time scale of tens or hundreds of picosecond in transition metals, and of tens of nanosecond in rare earth metals, which has more localized 4f electrons and exhibits smaller heat conductance κ.

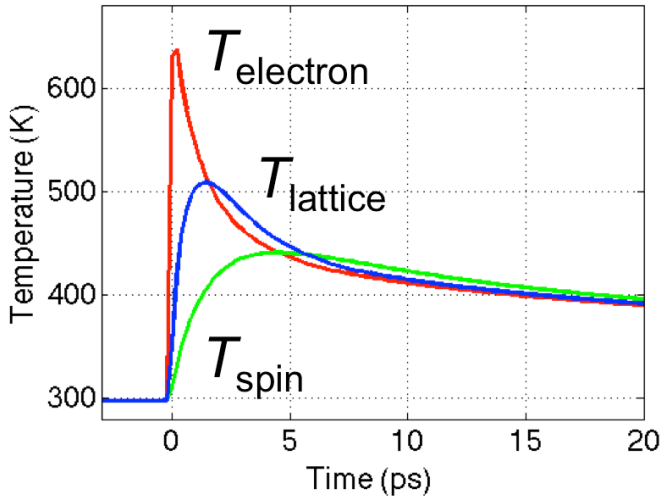

Fig. 3.4. An example of the three temperature modeling obtained with numerical time integration of (3.2.1). Heating in a 30 nm nickel film was simulated with the parameters listed in Table 3.1 and the peak pump fluence of 1.75 mJ/cm^2 with the FWHM of 200 fs. The plot shows the temperature of the three subsystems at the center of the nickel layer.

Parameters	Values
Pump fluence F (mJ cm^{-2})	1.70
Pump pulse duration full width half maximum (fs)	200
Complex refractive index $\tilde{n}$	$1.61+2.36i$
Electron thermal conductivity κ (W m^{-1} K^{-1})	91 [142]
Electron heat capacity per unit volume C_e (J m^{-3} K^{-1})	gT_e
g (J m^{-3} K^{-2})	6×10^3 [136]
Lattice heat capacity per unit volume C_l (J m^{-3} K^{-1})	2.2×10^6 [136]
Spin heat capacity per unit volume C_s (J m^{-3} K^{-1})	$m_1\left(1-T_s/T_C\right)^{0.1}+m_2$

m_1 (J m^{-3} K^{-1})	-2.15×10^{6} [143]
m_2 (J m^{-3} K^{-1})	2.38×10^{6} [143]
Currie temperature T_C (K)	631
Coupling coefficients [136]	
g_{sl} (W m^{-3} K^{-1})	0.3×10^{17}
g_{es} (W m^{-3} K^{-1})	5.6×10^{17}
g_{el} (W m^{-3} K^{-1})	7.0×10^{17}

Table 3.1. Parameters for three-temperature simulation in a nickel elliptic disk.

After the subpicosecond demagnetization, the spin system in TR-MOKE experiments experience a deterministic perturbation of the magnetization direction. This is usually attributed to the effective field pulse with ~150 ps pulse width originating from the temperature dependence of the material parameters, most commonly the crystalline/interfacial anisotropy. The effective field pulse can be modeled using a result of three-temperature model analysis and assumed T dependence of the parameters. It can also be approximated as a Gaussian field pulse with appropriate pulse width around 150 ps [66]. In typical simulation analysis where the small-angle precession frequency and damping is the primary interest, the exact shape and magnitude of the excitation field only has a limited effect on the final results.

Apart from the thermal excitation described in the previous paragraphs, nonthermal excitation with circularly polarized pump light is possible via the inverse

Faraday effect (IFE). Typically, in transition metals, the inverse Faraday effect is found very small (e.g., <0.01% contribution in nickel films) and the thermal effect dominates [139]. In transparent garnet films, however, the inverse Faraday effect can dominate the excitation process [144,145]. In [144], the phase and amplitude of the excited precession depended on the polarization of the pump pulses (Fig. 3.5). This result is attributed to a strong transient magnetic field due to the inverse Faraday effect. The authors estimated this effective field from the amplitude of the observed precession; for a transient power density of 10^{11} W/cm^2, the transient effective field due to the IFE was estimated to be ~0.6 T for the 100 fs pump pulse duration.

The effect was also demonstrated in a rare-earth–transition-metal ferrimagnet alloy too [146]. By measuring a GdFeCo film demagnetized into multiple domains, they cancelled the thermally-excited precession of differently magnetized domains, which are out of phase. The inverse Faraday effect, on the other hand, excites the coherent precession in all domains, contributing to the spatially averaged net signal.

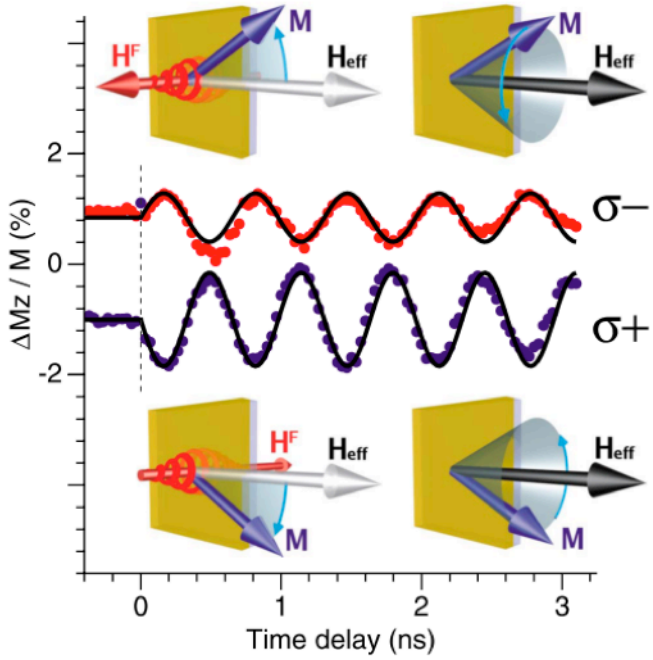

Fig. 3.5. Magnetization perturbation with inverse Faraday effect in a 7.5-μm-thick garnet ($Lu_{1.69}Y_{0.65}Bi_{0.66}Fe_{3.85}Ga_{1.15}O_{12}$) film with circularly polarized pump pulses. With 10^{11} W/cm^2 transient pump power density, the field induced with the inverse Faraday effect for the 100 fs pulse duration was estimated to be ~0.6 T from the observed precession amplitude. Taken from [144].

Recently, several groups demonstrated magnetization excitation by means of elastic strain. Through the magnetoelastic coupling of (Mn,Ga)As [147–150], they demonstrated that the magnetization precession can be excited by sending an acoustic pulse, generated with a laser pulse focused at a metallic layer separated from the ferromagnetic samples (Fig. 3.6). A few years later, magnetization excitation with

similar scheme was demonstrated in a 200-nm-thick polycrystalline nickel film as well [151].

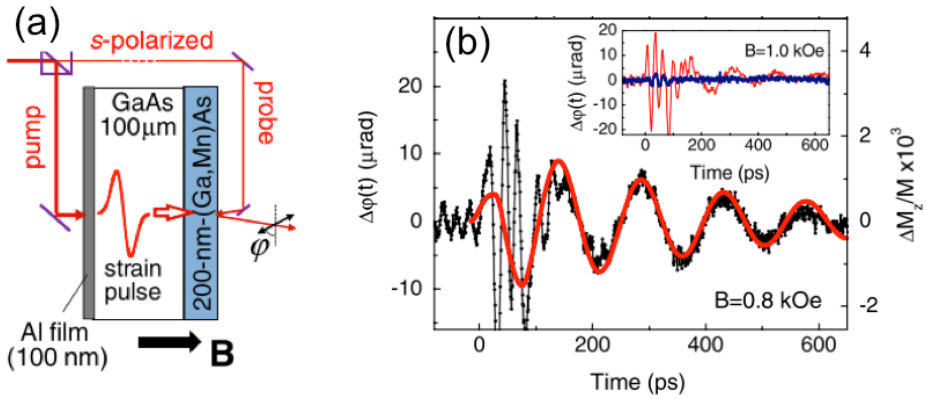

Fig. 3.6. (a) Pump-probe scheme with the pump pulse hitting the back of the substrate. An elastic pulse travels across the GaAs substrate and hits the (Ga,Mn)As film on the front side and excites the magnetization precession via magnetoelastic effect. (b) Observed MOKE rotation. For 0 to ~100 ps, the presence of the elastic strain in (Ga,Mn)As film modulates the reflected light intensity. After the strain pulse has left (>~150 ps), a clear oscillation due to the magnetization precession is observed. Taken from [147].

In our study, too, the magnetoelastic coupling was shown to play an essential role in magnetization excitation and evolution in patterned nanomagnets. The excitation laser pulse excites mechanical vibration modes of the nanostructure simultaneously with the magnetization precession. The two distinct oscillation

phenomena were found strongly coupled together. Detailed descriptions of the magnetoelastic effect and the measurements are given in Chapter 5 through 7.

For better manipulation of the spin systems, excitation with multiple field pulses has been investigated. Any of the magnetization perturbation schemes discussed above can be implemented with two or more excitation pulses. For example, see [132] for the magnetic field pulse with a CPW, [145] for the inverse Faraday effect in a garnet film, [152] for the magnetoelastic coupling in polycrystalline nickel. The thermal excitation with a pulse laser was also found to achieve similar effect in nickel films in our work. When the second excitation pulse of an appropriate power is delivered with the π phase delay of the precession period, it stops the magnetization precession. When the second pulse is delivered in phase, on the contrary, it can selectively enhance a particular oscillation mode with a given frequency. The delay between the two excitation pulses is determined by the precessional frequency of the mode of interest. This may be inconvenient when the precession is highly damped or when you try to suppress more than one frequency components. By using three or more pump pulses, it has been demonstrated that you have more leeway in adjusting the delay between pulses [152].

3.2.2 Probing magnetization dynamics

After the perturbation of spin system discussed in the previous section, the evolution of the magnetization is probed with a probe laser pulse, which is delivered to the sample with a controlled time delay t from the magnetization perturbation. Upon reflection from the sample, the polarization of the probe beam is changed via

magneto-optic effects and is converted to the laser power using a set of polarization optics. By controlling the delay t and recording the polarization, the magnetization evolution is obtained as a function of time t after excitation. Following the discussion in [153], this section reviews several experimental configurations to monitor the magnetization evolution using the magneto-optic Kerr effect.

The polarization of the reflected beam is analyzed with a second polarizer. Three widely used configurations are known for analyzing the polarization of the probe beam after transmission or reflection from the sample. Crossed polarizers, balanced photodetectors (BPD), and photoelastic modulator (PEM) will be discussed in the following part. Here, the probe light has linear polarization defined by going through a polarizer oriented at an angle α_P. The light intensity at each part of the experimental setup is analyzed with the Jones vector

$$\boldsymbol{E} = \begin{pmatrix} E_S \\ E_P \end{pmatrix} = \begin{pmatrix} \sin\alpha_P \\ \cos\alpha_P \end{pmatrix} \tag{3.2.2}$$

and the Jones matrix for the polarization change upon reflection from the sample

$$S = \begin{pmatrix} r_S & -r_S\tilde{\theta}_K \\ r_S\tilde{\theta}_K & r_P \end{pmatrix}, \tag{3.2.3}$$

where $\tilde{\theta}_K = \theta_K - i\eta_K$ is the complex Kerr rotation for s-polarized light in the limit of $\left|\tilde{\theta}_K\right| << 1$. r_s and r_p are the reflection coefficients for s- and p-polarized light, respectively.

The simplest of the three detection configurations is the crossed polarizer configuration, where the second polarizer (analyzer) is oriented at approximately 90°

from the transmitting axis of the first polarizer. With the polarizer angle $\alpha_P = \pi/2$ and a small analyzer angle from the rejection direction $|\alpha_A| << 1$, the intensity of the probe after the analyzer is expressed as

$$\frac{I}{I_{in}} = \left| \begin{pmatrix} \sin\alpha_A \\ \cos\alpha_A \end{pmatrix}^T S \begin{pmatrix} \sin\alpha_P \\ \cos\alpha_P \end{pmatrix} \right|^2 = R\left(\alpha_A^2 + 2\alpha_A\theta_K + \varepsilon^2\right), \tag{3.2.4}$$

where R is the reflectivity of the sample. The second term in the right hand side of (3.2.4) is proportional to the Kerr rotation angle θ_K. From (3.2.4), the dynamic part of the signal is

$$\frac{\Delta I(t)}{I_{in}} = 2R_0\alpha_A\Delta\theta_K(t) + \alpha_A^2\Delta R(t). \tag{3.2.5}$$

As (3.2.5) shows, the signal is also modulated by the change in the reflectivity and this configuration does not separate the nonmagnetic signal $\Delta R(t)$ from the magnetic signal. As will be discussed in Chapter 5, this is not desirable in the measurements of patterned arrays, where the separation of magnetic and nonmagnetic signal becomes critical. One can increase the MOKE signal by making α_A bigger, however, the photodetector suffers larger noise from increased background photocurrent. As a result, the signal to noise ratio (SNR) is typically optimized by rotating the analyzer by 3°-7° from the rejection orientation [154].

The other two configurations, in principle, are able to completely separate the nonmagnetic contribution from the TR-MOKE signal. The balanced photodetectors utilize two photodiode and a polarizing beamsplitter, oriented along approximately 45° from the transmission axis of the first polarizer, as sketched in Fig. 3.7. The angle

of the polarizing beamsplitter is adjusted to balance the intensity of the two split beams. The polarization of the probe beam is analyzed by subtracting the signal of the two detectors. This can be done either by subtracting the photocurrent of the two detectors before amplification or by amplifying each photocurrent first with a transimpedance amplifier and subtracting the voltage with an op-amp circuit. The subtraction of the photocurrent before any amplification has the lowest additive noise. The subtraction of signals has additional advantage in SNR due to the cancellation of the common mode noise at the two detectors, especially with a somewhat noisy light source. The transimpedance amplifier circuitry has an advantage of providing the separate photodetector signals and simultaneously enabling another operation. With the s-polarized probe beam (polarizer angle $\alpha_P = 0$), the difference signal is

$$\begin{aligned}\frac{I}{I_{in}} &= \left|\begin{pmatrix}\sin\alpha_A\\ \cos\alpha_A\end{pmatrix}^T S\begin{pmatrix}\sin\alpha_P\\ \cos\alpha_P\end{pmatrix}\right|^2 - \left|\begin{pmatrix}\sin\alpha_A\\ -\cos\alpha_A\end{pmatrix}^T S\begin{pmatrix}\sin\alpha_P\\ \cos\alpha_P\end{pmatrix}\right|^2 \\ &= R\left[\left(\cos^2\alpha_A - \sin^2\alpha_A\right)\left(\theta_K^2 + \eta_K^2 - 1\right) + 4\sin\alpha_A\cos\alpha_A\theta_K\right]\end{aligned}. \qquad (3.2.6)$$

The difference signal of the two photodiodes (3.2.6) is balanced when

$$\frac{2\sin\alpha_A\cos\alpha_A}{\cos^2\alpha_A - \sin^2\alpha_A} = \tan(2\alpha_A) = \frac{1-\theta_K^2-\eta_K^2}{2\theta_K} \approx \frac{1}{2\theta_K}, \qquad (3.2.7)$$

or for $\alpha_A \approx 45°$. Using $\alpha_A = 45°$ yields a dynamic response of

$$\frac{\Delta I(t)}{I_{in}} = 2R_0\Delta\theta_K(t) + 2\theta_{K0}\Delta R(t), \qquad (3.2.8)$$

which still has a nonmagnetic contribution proportional to $\Delta R(t)$. Complete separation of the nonmagnetic signal can be achieved when the condition (3.2.7) is met, where

the signal of the two detectors are exactly balanced. The total signal becomes $I(t)/I_{\text{in}} = 2R(t)(\theta_{\text{K}}(t) - \theta_{\text{K0}})$ and, in the limit of small Kerr rotation,

$$\frac{\Delta I(t)}{I_{\text{in}}} = 2R_0 \Delta\theta_{\text{K}}(t). \tag{3.2.9}$$

The sum of the signals can also be obtained. It simply shows the change in the reflectivity $\Delta R(t)$. This provides a convenient way of monitoring both of magnetic and nonmagnetic signals at the same time.

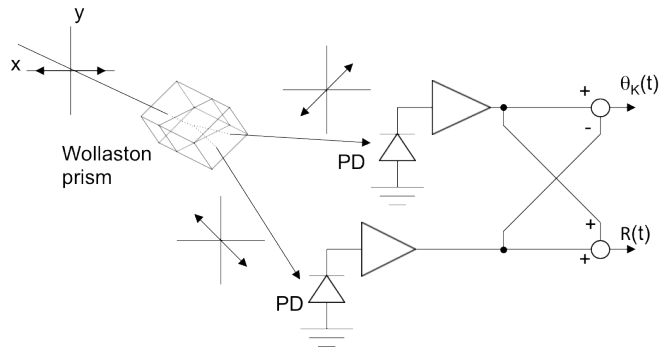

Fig. 3.7. The balanced photodetector configuration for detecting the magnetic (difference) signal $\theta_{\text{K}}(t)$ and nonmagnetic (sum) reflectivity $R(t)$. Wollaston prism (analyzer) oriented at the analyzer angler $\alpha_{\text{A}} \approx \pi/4$ splits the probe beam into orthogonal polarizations. The photocurrent from the two photodiodes (PDs) are converted to voltage and the difference and the sum of the voltage signal is obtained using a set of operational amplifiers.

An alternative method of completely separating the nonmagnetic contribution from the signal is modulating the polarization of the probe beam. This is achieved

with a photoelastic modulator (PEM), placed before the sample with its modulation axis 45° from the transmission axis of the first polarizer. The PEM stretches and compresses along the modulation axis at 20-200 kHz (typically at 50 kHz) and modulates the relative retardation of the two linearly polarized light, along and perpendicular to the modulation axis. When the modulation axis is aligned 45° from the light polarization with a proper modulation depth, the polarization of the transmitted light becomes RCP and LCP repeatedly, as depicted in Fig. 3.8. With smaller modulation depth, the polarization of the transmitted light remains elliptic.

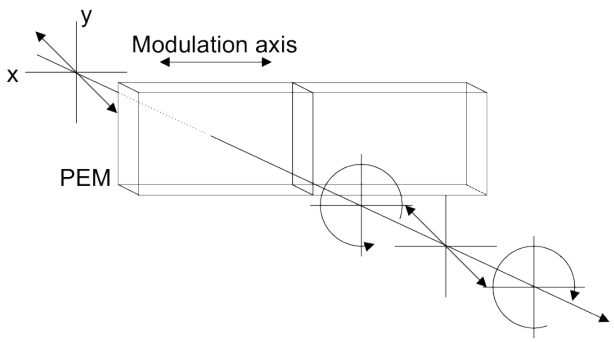

Fig. 3.8. Polarization modulation with a PEM. The transducer stretches and compresses the PEM crystal at 20–200 kHz, modulating the retardation of light polarized along the modulation axis. Depending on the depth of modulation A_0, the transmitted light becomes elliptically or circularly polarized.

Various configurations with the PEM [153] are used but we present one common setup here. When the modulation axis of the PEM is aligned along the s polarization direction, the incident probe beam is modulated with the Jones matrix

$$M(t') = \begin{pmatrix} 1 & 0 \\ 0 & e^{iA(t')} \end{pmatrix}, \tag{3.2.10}$$

where $A(t') = A_0 \cos(\Omega t')$. A_0 is the depth of modulation and t' is the time for PEM modulation. The polarizer transmission axis is set to $\alpha_P = \alpha_M + \pi/4 = \pi/4$. The reflected beam is analyzed with an analyzer with $\alpha_A \approx 0$ (transmitting s polarized light) and the power at the detector is characterized as

$$\frac{I(t')}{I_{in}} = \left| \begin{pmatrix} \sin\alpha_A \\ \cos\alpha_A \end{pmatrix}^T SM(t') \begin{pmatrix} \sin\alpha_P \\ \cos\alpha_P \end{pmatrix} \right|^2$$

$$= R\left\{ \frac{1}{2} - (\theta_K - \rho'\alpha_A)\cos[A(t')] - \eta_K \sin[A(t')] \right\} \tag{3.2.11}$$

within the first order of α_A and $\tilde{\theta}$. By expanding $\cos[A_0 \cos(\Omega t')]$ and $\cos[A_0 \cos(\Omega t')]$ in (3.2.11) with spherical harmonics $\cos(n\Omega t')$, AC component at the harmonics of Ω are obtained carrying various information. The amplitude of the three lowest harmonics (n = 0, 1, and 2) is obtained as

$$\frac{I_{dc}}{I_{in}} = R\left[\frac{1}{2} + J_0(A_0)\theta \right] \approx \frac{R}{2} \tag{3.2.12a}$$

$$\frac{I_\Omega}{I_{in}} = -J_1(A_0) R \eta_K \tag{3.2.12b}$$

$$\frac{I_{2\Omega}}{I_{in}} = J_2(A_0) R(\theta_K - \rho'\alpha_A), \tag{3.2.12c}$$

where $J_n(A_0)$ is the nth order Bessel function. The second term in (3.2.12a) can be eliminated by choosing A_0 = 2.405. In the weak perturbation limit, the dynamic signal becomes

$$\frac{\Delta I_{\Omega}(t)}{I_{\mathrm{dc}}} = -2J_1(A_0)\left[\Delta\eta_{\mathrm{K}}(t) + \frac{\Delta R(t)}{R_0}\eta_{\mathrm{K}0}\right] \tag{3.2.13a}$$

$$\frac{\Delta I_{2\Omega}(t)}{I_{\mathrm{dc}}} = 2J_2(A_0)\left[\Delta\theta_{\mathrm{K}}(t) + \frac{\Delta R(t)}{R_0}\left(\theta_{\mathrm{K}0} - C_0(t)\alpha_{\mathrm{A}}\right)\right], \tag{3.2.13b}$$

where $C_0(t) = \rho_0' + \left(\Delta\rho'(t)/\Delta R(t)\right)R_0$. As (3.2.13) shows, the ellipticity η_{K} at time t appears as an oscillating component at Ω and the polarization angle θ_{K} is reflected in 2Ω component. The lock-in amplification at these frequencies extracts the dynamic MOKE signal.

In order to achieve larger SNR, double-modulation configuration is typically used. As depicted in Fig. 3.9, a second lock-in amplifier is used with the chopped pump beam as the reference frequency. Comparing to the mechanical chopping in other excitation schemes (~ 1 kHz), somewhat fast PEM modulation (~ 50 kHz) requires sufficiently large photodetector bandwidth. This is not a challenging requirement with a transimpedance amplifier but a naïve current-voltage conversion with a small resistor may suffer low SNR. The need for the second lock-in amplifier limits the time constant of the first lock-in amplifier to be below $1/(2\pi f_{\mathrm{chopper}})$. The balance between the large mechanical noise at low chopping frequency and the required noise rejection at the first stage determines f_{chopper}.

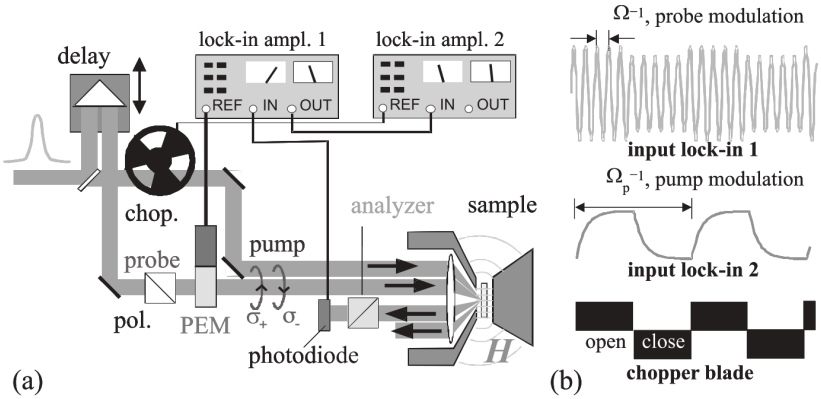

Fig. 3.9. Double-modulation configuration for TR-MOKE with a PEM. The first lock-in amplifier picks up either Ω or 2Ω component. The pump is chopped at somewhat slow rate of ~100 Hz for the second-stage lock-in amplification. Taken from [153].

3.3 TR-MOKE setup

The evolution of magnetization in femto- and picosecond time scale is monitored with the time-resolved magneto-optic Kerr effect (TR-MOKE) setup. Fig. 3.10 shows a general schematic of the setup. Ultrafast laser pulses from a Ti:sapphire laser (Coherent MIRA 900, center wavelength: 800 nm, repetition rate: 76 MHz, FWHM: 150 fs) is split into the pump and the probe beams. The pump beam is converted to half the wavelength (400 nm) with a second harmonic generator (Coherent SHG) and a color filter to remove any residual 800 nm light with the extinction rate of ~10^{-5}. This enables a good separation of the pump and probe beams with a color filter before photodetectors and enables the use of high numerical

aperture objective lens ($60\times$ objective with the NA of 0.85) with both beams coaxially aligned and guided to the sample with normal incidence. A single pump pulse typically conveys 13 pJ of energy to the sample and is focused down to the $1/e^2$ diameter of 1–10 μm. The probe beam has smaller energy and is combined with the pump beam after going through an optical delay stage. Two delay stages (PI M-531 and Newport M-IMS400PP) are placed in the probe beam path in series (Fig. 3.10 shows only one conceptual delay stage). They move a total scan length of 60 cm and control the delay time between pump and probe pulses up to 4 ns with the precision of ± 20 fs. The reflected beams from the sample is collected with the same objective lens and guided to the balanced photodetectors. The color filter eliminates the pump beam from the detection arm and the probe beam polarization is analyzed with balanced photodetectors. A polarizing beamsplitter cube (PBSC) or a Wollaston prism is used to split the probe light components with different polarizations. Due to the etalon fringe of the parallel faces of cubic prisms, the PBSC has poorer noise characteristic. Replacing it with a Wollaston prism reduced the noise density by 6 dB at 1 kHz. The photocurrent from silicon photodiodes is immediately amplified with an embedded op-amp circuit (OPT101) in order to avoid picking the noise from environment (e.g., magnetic field and vibration). This converts the small photocurrent into voltage signal with the DC gain of 2×10^5 V/A and enables using somewhat long (~20 cm) cables for more convenient detector mounting. The amplified voltage signal is subtracted from each other with a home-built op-amp circuit. This circuit also outputs the sum signal of the detectors simultaneously. This enables the

measurements of the magnetic (difference channel) and nonmagnetic (sum channel) measurement at the same time, as will be used in Chapter 6 and 7. In addition to the sensitivity to light polarization, the difference channel enjoys the suppression of the common mode noise and achieves greater SNR than the sum channel. With typical probe power, the difference signal has the noise density of 0.6-0.9 $\mu V/\sqrt{Hz}$ (2–3 dB above the shot noise) at 1 kHz. The sum signal has larger noise density of ~5 $\mu V/\sqrt{Hz}$.

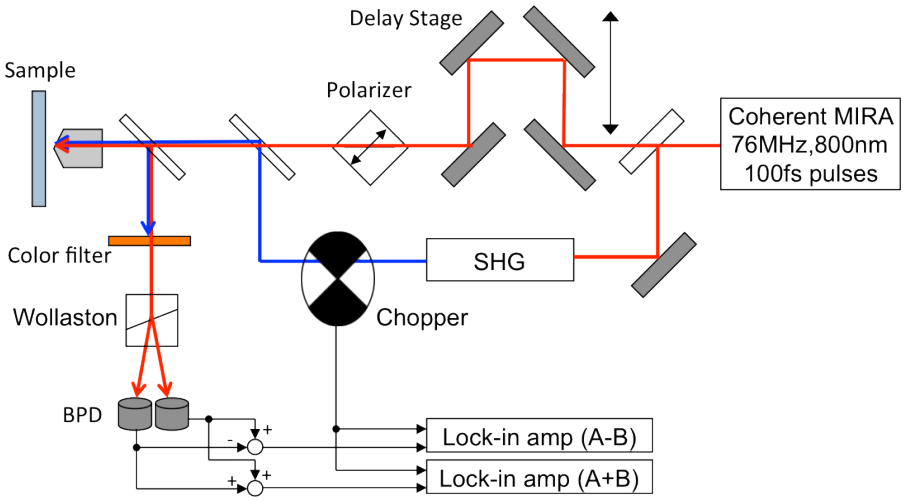

Fig. 3.10. Schematic of all-optical TR-MOKE system. Ultrafast laser pulses are split into the pump (400 nm) and probe (800 nm) beams and focused on the sample with a $60\times$ objective. Reflected probe beam is analyzed with the balanced photodetectors and lock-in amplifiers.

The sample is mounted on a commercial Witec microscope system modified for magnetic field application and drawing in external laser beams. An embedded bright-field optical microscope and a CCD camera capture the surface images as well as the probe beam spot. The focus of the beams is adjusted by changing the height of the objective assembly controlled with a stepper motor. The stage is actuated with a 3-axis piezoelectric scanner and enables precise control of the sample position with ~10 nm precision. This enables measurements of single nanometer scale magnets. Even though it is typically not well resolved in the optical microscope, one can find them by monitoring the reflected probe power as you move the stage.

With the automation of the focal position and the sample positioning, knife edge measurements of the pump and probe spot size achieves higher precision than a previously used manual procedure. A beam is focused at a sharp edge of sample and the edge position is scanned with the sample stage. The reflected light is collected with an embedded multimode fiber and a photomultiplier tube. The reflected power is modeled as an integration of a two-dimensional Gaussian peak, resulting in an error function [155]

$$P_{\mathrm{N}}(x) = \frac{1}{2}\left[1 + \mathrm{erf}\left(\frac{x - x_0}{w}\right)\right], \tag{3.3.1}$$

where w is the $1/e^2$ beam radius. Fig. 3.11a shows an example of the knife edge measurements taken at an edge of a 30-nm-thick nickel film deposited on an AR coated silicon (λ = 800 nm) substrate. From the fit, the $1/e^2$ spot radius w and beam position x_0 are determined as a function of the objective height, as shown in Fig.

3.11b. Cleaved silicon edges work well, having a clear contrast of the reflected beam power. A deposited micron-scale structure with straight edges also works and frequently is more convenient since they can be found close to the sample structure of interest. When the contrast of the reflectivity from the deposited structure and the substrate is small, this hampers the measurement precision.

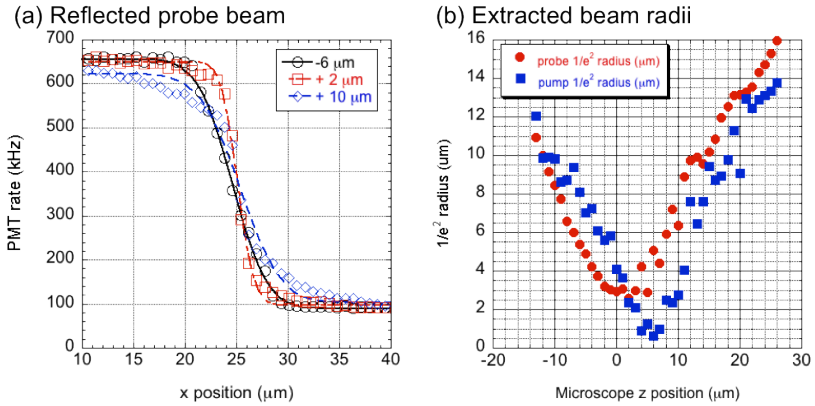

Fig. 3.11. Knife edge measurements of the pump and probe beam, taken at an edge of 30 nm nickel film deposited on an AR coated silicon substrate (λ = 800 nm). (a) Representative probe beam power measured as a function of the edge position, taken at the objective height of –6, +2, and +10 μm. Scanned in x direction. (b) $1/e^2$ beam diameter estimated with (3.3.1). The horizontal axis is the height of the objective, relative to the focal point of the CCD image. TR-MOKE measurements are usually carried out at the objective height close to 0 um. If desired, the focus of each beam can further be adjusted separately by changing the beam diversion before entering the objective.

The external field is applied using a pair of permanent NdFeB magnets. Two magnets with $1/2 \times 1''$ cylinder are paired antiparallel and placed below the sample stage. The stray field from the cylinder bases forms a semi loop as depicted in Fig. 3.12a and field with arbitrary magnitude and direction in the xz plane can be obtained by adjusting the magnet position. The magnets are placed on a 3-axis stepper motor. The sample mount has an opening to allow the approach of the magnets up to the backside of the sample. Unlike the well-defined field in a gap between electromagnet poles, the field obtained with the NdFeB magnets suffers more uncertainty. However, it has a great advantage in flexible field orientation and smallness. The front end of the sample is completely untrammeled and any optical beam path configuration can be implemented.

To obtain accurate field values with the NdFeB magnets, somewhat elaborate field calibration is necessary. A millimeter scale Hall probe was mounted in the sample stage and recorded the x component of the magnetic field at various magnet positions. The Hall probe was then rotated by 90° and recorded the z component as a function of magnet position. The active Hall sensor device is embedded in a plastic plate and the magnet position is accordingly offset with the probe design. The obtained field vector was then interpolated as in Fig. 3.12b and a numerical inverse function is obtained. Taking a desired field value and direction, this function returns the position where the magnet pair should be placed. An in-house AutoIt script [156], Magnet Positioner, controls the 3-axis stage via Witec microscope controller software and moves the magnets to the target position.

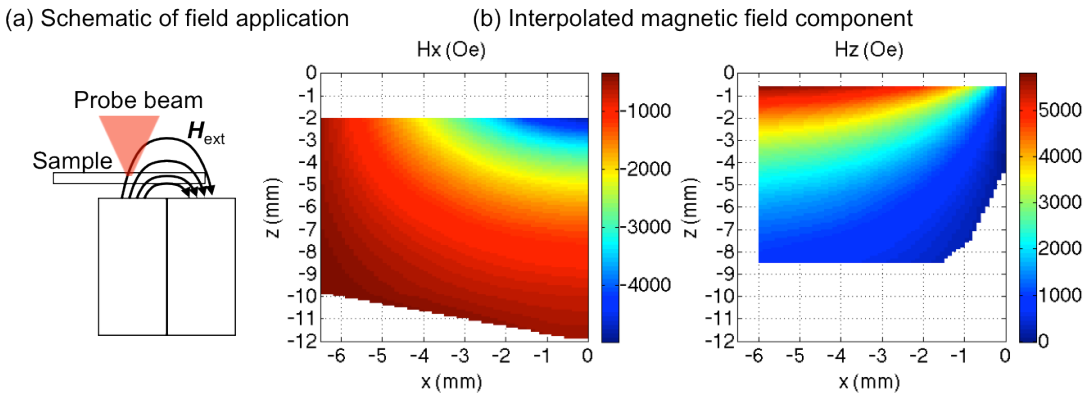

Fig. 3.12. (a) Schematic of field application with a pair of cylindrical NdFeB magnets. (b) Interpolated H_x and H_z measured at magnet position of (x,z). The origin (0,0) is defined as the center of the two magnet faces at the height of the sample's front surface.

3.4 Analysis method

The recorded signal from the TR-MOKE is analyzed to extract the precession frequency and the effective damping coefficient α. The decaying background of the signal should be subtracted by fitting the signal with a spline curve. When a spline curve is used to model the background decay, care should be taken not to induce artificial oscillation, especially with a small signal and large background. Fig. 3.13a and b shows typical signal and background subtraction, measured on a 30-nm-thick polycrystalline nickel film. From the data, we extract the frequency of the magnetization precession and damping parameter α.

3.4.1 FFT

To analyze the background-subtracted signal of TR-MOKE, Fast Fourier transform (FFT) is implemented with Matlab. The raw data is interpolated and resampled to make the total length of 2^n with a constant interval. Hamming or Blackman window function is applied in order to mitigate the side lobes in Fourier spectra at the expense of slightly compromised frequency resolution. Our typical TR-MOKE scan is 800–2500 ps long and the frequency resolution of the Fourier spectra becomes 0.4–1.3 GHz [157 pp. 555–559]. A series of zeros is padded at the end of the data [157 pp. 583–588], making the total length 2^{n+m}. In our setup, m = 2–3 is selected to make the total length of the data equivalent to 6–8 ns. Imperfect background subtraction gives rise to slow transition of signal, which results in the low frequency component (as seen in Fig. 3.13c). By repeating the measurements and analysis with various applied field $\boldsymbol{H}_{\text{app}}$, field-dependent spin wave spectra are obtained. As shown in Fig. 3.13d, the film signal typically shows a clean single frequency peak. From nanomagnets, the precession frequency may show more complex spectra, reflecting the edge modes or surface acoustic waves, as will be discussed in Chapter 5. When multiple peaks are close to each other, eyeballing of the peak frequency may be spurious and we fit the peaks with a Gaussian shape using least square method. This is especially important to eliminate the arbitrariness when multiple peaks are partially overlapping to each other.

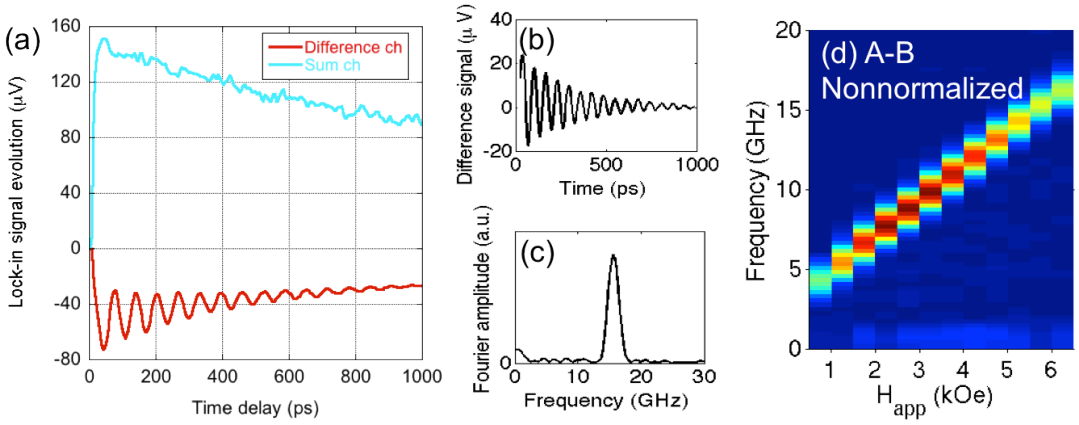

Fig. 3.13. Exemplary TR-MOKE signal from a 30 nm polycrystalline nickel film. (a) Evoluation of lock-in raw signals of difference (magnetic) and sum (nonmagnetic) channels. (b) Background-corrected difference signal and (c) its Fourier spectrum. (d) Fourier spectra of the difference signal measured at various field H_{app} applied at 30° from the surface normal.

3.4.2 Damping analysis with digital filtering

Unlike in FMR measurements where linewidth is proportional to the decay constant of the oscillation, the linewidth of TR-MOKE peak is often determined by the length of the signal. This is because the FMR is essentially a time-invariant measurement with energy constantly pumped into the system, while TR-MOKE is a time-domain measurement with pulsed excitation. In order to extract the damping parameter, therefore, we directly analyze the transition of the oscillation amplitude in time domain, as demonstrated in various studies [71,104,105,133,158–160].

The background-subtracted signal can be fitted with a damped harmonic oscillation

$$x(t) = A_0 \exp(-\gamma t)\cos(\omega t + \phi), \tag{3.4.1}$$

where $\gamma = 1/\tau$ is the decay constant and ω is the angular frequency of the precession. An effective Gilbert damping parameter α can then be obtained by solving [104,161]

$$\frac{1}{\tau} = \frac{\alpha\gamma}{2(1+\alpha^2)}(H_1 + H_2) \tag{3.4.2a}$$

$$\omega = \frac{\gamma}{1+\alpha^2}\sqrt{H_1 H_2}\,, \tag{3.4.2b}$$

where H_1 and H_2 are defined as in Eq. (2.2.30). At a sufficiently high field where the precession frequency is dominated with the Zeeman term (i.e., when $H_1 \approx H_2$), this is simplified as

$$\alpha \approx \frac{1}{\omega\tau}\,. \tag{3.4.3}$$

Note two points here—the effective damping parameter and the presence of multiple peaks in signal. First, the damping in TR-MOKE signal is also affected by the inhomogeneity of in the sample, namely, the deviation of the material parameters in each position, presence of grains and physical defects, and the nonuniform excitation by the Gaussian pump beam. These factors lead to increase in the decay constant γ apparent in a TR-MOKE signal and results in larger estimate of α, especially at a small field. The intrinsic Gilbert damping can be obtained as a limit in high external field [71,104,162–164]. At high field, the magnetization dynamics is

dominated by the Zeeman energy term, reducing the relative effects of the inhomogeneity. In this field range, direct fitting of the damped oscillation signal reports comparable α values with the FMR measurements [161,165].

Fitting with Eq. (3.4.1) can only be applied reliably when the signal shows a clean damped oscillation with a single frequency component and low noise. Unavoidable noise in the real measurement prevents the reliable fitting with two or more frequency components. To circumvent this problem, we apply a digital filter on the signal and extract an oscillation with a single frequency peak. The Butterworth bandpass filter with phase compensation is applied to the signal. Typically, 3 dB bandpass width of 0.5–8 GHz is used with phase compensation. In order to maintain the shape of the damped oscillation, phase change in each frequency component must be compensated. This can be achieved by applying digital filtering twice to the signal, first in the forward direction and second in the backward direction [157]. The operation is provided as filtfilt() function in Matlab. Digital filtering unavoidably induces artifacts at the beginning and the end of the signal, showing rapid rise at the beginning and decay at the end of the filtered signal. The beginning and the end of the filtered signal must be trimmed and only the middle part should be fitted with Eq. (3.4.1). Fig. 3.14 shows an example of damping analysis with digital filtering applied on a TR-MOKE signal from a CoFeB film. The bandpass filter rejects the noise except for the passband and the resulting oscillation becomes much clearer. Note that, however, when the signal has large additive noise, the presence of the noise results in the fluctuation of the analysis results.

To test the reliability of the above procedure, the analysis has been repeated on an artificially generated signal with Gaussian noise with variance σ^2. With the signal-to-noise ratio defined as

$$SNR = \frac{A_0^2}{2\sigma^2} \text{ or } 10\log\left(\frac{A_0^2}{2\sigma^2}\right)(\text{dB}) \tag{3.4.4}$$

with the amplitude of damped oscillation A_0 defined in (3.4.1). The resulting α_{eff} value is distributed across the predicted one. With SNR = 3 (4.8 dB), the relative error of damping estimate distributes around the zero with the standard deviation of 0.08. Therefore, for analysis of experimental data with relatively low SNR, it is vital to repeat the measurement various times and obtain the trend of the α_{eff}.

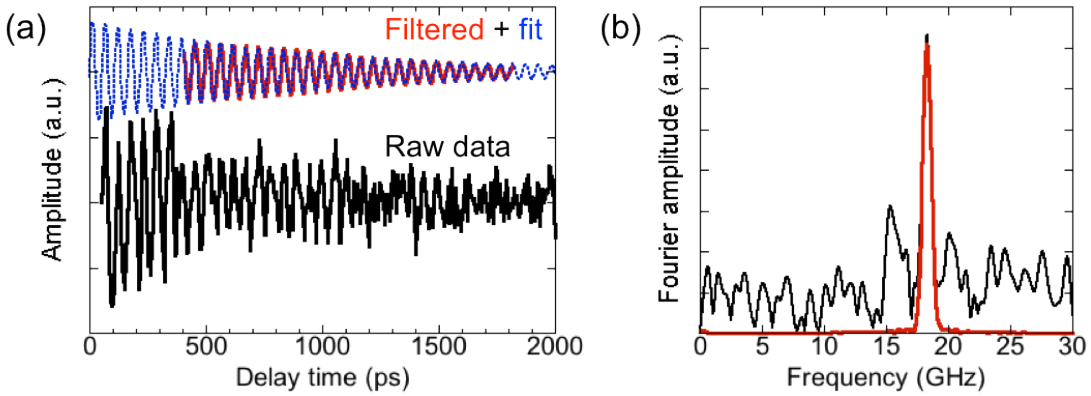

Fig. 3.14. Example of damping fit with digital filtering. The sample is a CoFeB/MgO multilayer stack designed for STT-MRAM application. In (a), a first-order Butterworth filter with the 3 dB passband width of 0.7 GHz centered at 18.3 GHz has been applied with the phase compensation. The filtered time trace has been truncated to exclude the artifacts from digital filtering showing supurious changes in oscillation

amplitude at the beginning and the end of the data. (b) Absolute Fourier amplitude of the raw and filtered traces.

4. Dynamic separation with nanomagnet orientation

In this chapter, we will present the dynamic separation technique applied on arrays of nickel nanomagnets, containing two subarrays of elliptic disks with orthogonal orientations. Even though the spatial resolution of the measurement is nowhere near the nanomagnet dimensions, the distinct dynamic behaviors of the two subgroups of nanomagnets, determined by the orientation of the elliptic disks with respect to the external field, enables separating magneto-optic signal of one subgroup from the other. The effect of the neighboring elements in a particular nanomagnet subgroup is quantified as a function of the array pitch. With micromagnetic modeling of the sample structure, the change in dynamic behavior is explained with the magnetostatic environment each subgroup of nanomagnets is placed in.

4.1 Introduction

Various dynamic measurement techniques have been demonstrated to measure the array magnetization characteristics in wide range of samples. In many of these studies, however, the signal is an ensemble average of many nanomagnets within the detected area. For example, vector-FMR has a micrometer-scale spatial resolution limited by the dipole field profile from the coplanar waveguides [166]. For optical techniques such as TR-MOKE and BLS, this is typically limited by the diffraction limit. While the ensemble signal conveys statistic information about the average properties and the irregularity of the individual elements, such as size, shape,

composition, and crystalline order, it is generally difficult or impossible to decompose the magnetization dynamics of the individual nanomagnet.

A common approach for solving this issue is measurements of a single isolated nanomagnets without the presence of neighboring elements. This provides the insight into the intrinsic response of individual magnets and predicts the collective behavior of the similarly fabricated elements in arrays. Various challenges arise. The signal to noise ratio typically reduces drastically due to the reduced size of the sample, both in optical techniques, such as TR-MOKE and BLS, and in electrical techniques, such as FMR and VSM. Optimization in sample geometry [89,167, 168] is necessary in order to probe small nanomagnets.

Scanning probe microscopy-based techniques is a great way to obtain *static* properties of nanomagnets with high spatial resolution, limited only by the tip radius of the probes. High-resolution MFM with field application (simultaneous or sequential with MFM scans) have been widely used for static characterization of nanostructured magnets [83].

The near-field scanning optical microscopy (NSOM) with fiber probes or solid state pyramid probes have been demonstrated in conjunction with static MOKE measurements too [89,169–171]. With proper choice of the near-field aperture that conserves light polarization, the magnetic domains with opposite magnetization directions were observed with the spatial resolution limited only by the near-field aperture size, typically with diameter of 30–150 nm (for the pyramid probes). The SNR is severely limited by the low throughput of the near-field apertures, typically in

the order of 10^{-6}, and has prohibited the TR-MOKE measurements with near-field optics so far. BLS was demonstrated on a permalloy micromagnet on a CPW in conjunction with NSOM [69].

In this Chapter, we discuss the newly developed dynamic separation technique to probe the individual groups of nanomagnets within densely packed arrays. In this measurement technique, the sample nanomagnet array is composed of two or more types of elements with distinct properties, such as size, shape, orientation, or material, as illustrated in Fig. 4.1. The entire array is measured with TR-MOKE using diffraction limited optics. Although the reflected probe beam shows the polarization change due to many nanomagnets, the distinct nature of individual elements results in the precessional oscillation at different frequencies. With the discrete Fourier transform, one can separate the signal from the individual groups of magnets from each other.

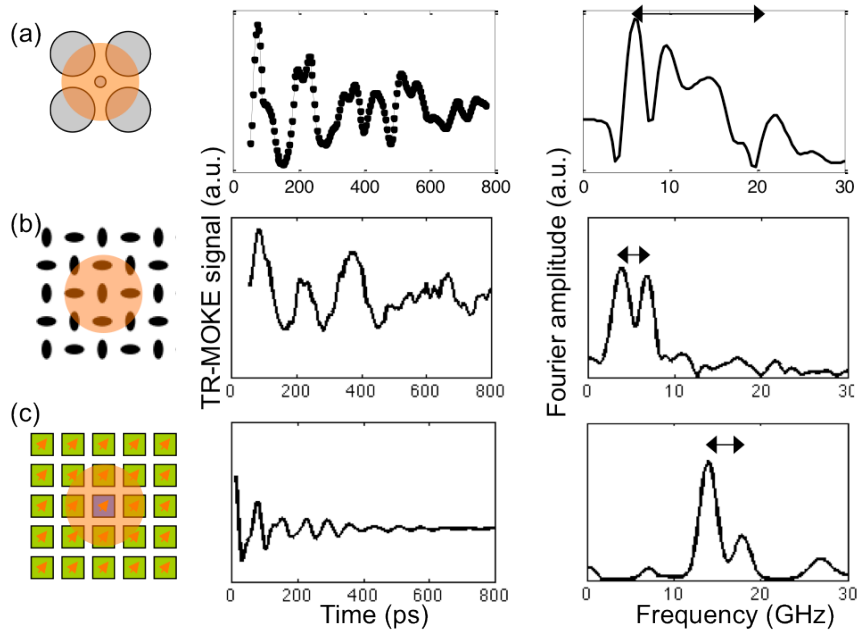

Fig. 4.1. Principle of dynamic separation. The sample arrays consist of two or more types of nanomagnets. Examples of dynamic separation with (a) size, (b) orientation, and (c) material along with a representative TR-MOKE time traces (middle column) and the corresponding Fourier spectra (right column). (a) and (b) shows experimental data measrued on nickel nanomagnet arrays, while (c) shows a micromagnetic simulation results calculated with iron and nickel parameters.

The first demonstration using separation by size was reported in [81]; a 150-nm-thick nickel nanomagnet disk with 150 nm diameter was placed within an array of 500 nm disks and measured with the TR-MOKE with ~ 1 μm probe spot size (Fig. 4.2). The small nickel disk was saturated under the external field between 2.5 and 5.0 kOe, while the larger 500 nm disks were in the vortex state. The TR-MOKE signal showed two frequency peaks clearly separated from each other, demonstrating

the concept of dynamic separation (Fig. 4.2c–e). The frequency difference between the magnetization precession in the smaller 150 nm disk and the vortex core vibration in the 500 nm disks was more than 7 GHz for the entire field range and was greater than the line width of the mode peaks. The effect of the dipole field from the neighbors was quantified with a simpler configuration fabricated with the FIB. A structure of one 150 nm disk between two 500 nm disks were measured with TR-MOKE and the precession frequency of the center 150 nm disk was probed as a function of the edge-to-edge separation. The precession frequency changed by ~5 GHz in the measurements with 100 and 200 nm edge-to-edge separation. This was attributed to the difference of ~300 Oe in dipole field from the neighboring 500 nm disks, calculated in a micromagnetic model.

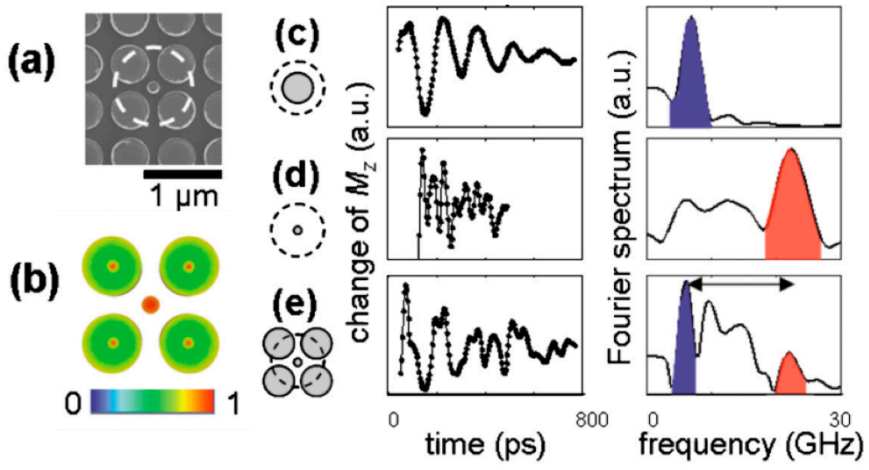

Fig. 4.2. Demonstration of dynamic separation by size. (a) SEM image of a sample array of 150-nm-thick nickel disks. A 150 nm disk was embedded in an array of 500 nm elements. The dashed circle represents the size of the probe spot. (b) Simulated z

component of the magnetization in a ground state, showing the single-domain and vortex states of the small and large nickel disks. (c–d) TR-MOKE time traces and Fourier spectra measured with various configurations represented by the skecthes on the left side. Taken from [81].

In this chapter, the dynamic separation is extended to the orientation of identically shaped nickel nanomagnets with respect to the applied external field. The major findings have been reported in [172]. Unlike in the previous case, the sample arrays consist of the elements with identical shapes, as in more realistic situations, but are oriented in two orthogonal directions.

4.2 Samples and experimental details

The sample arrays of nickel elliptic disks were fabricated at the Molecular Foundry with the electron beam lithography, electron beam evaporation, and liftoff process on an AR coated silicon substrate. Fig. 4.3 shows the SEM images of the fabricated nanomagnets. The major and minor axes are 150 and 85 nm, respectively, as measured with the SEM. Two different configurations of nanomagnet arrays are considered as shown in Fig. 4.3. The first type (Fig. 4.3a) has uniformly oriented elliptic disks and is called the array with "uniform" orientation. The other (Fig. 4.3b) has two subsets of elliptic disks with alternating major axis orientation and is called "alternating" arrays. We define the orientation of the elliptic disks by the angle ϕ between their major axis and the in-plane component $\boldsymbol{H}_{\mathrm{ip}}$ of the applied field $\boldsymbol{H}_{\mathrm{app}}$. Thus, the first type, when $\boldsymbol{H}_{\mathrm{ip}}$ is either parallel or perpendicular to the major axis of

the elliptic disks, is referred to as the "parallel" or "perpendicular" configuration, respectively. Arrays with various center-to-center pitches p were fabricated. For the uniform orientation, p = 212 or 282 nm, whereas the arrays with alternating disks have p = 145, 212, and 282 nm. The smallest p of 145 nm is only plausible in the alternating configuration. During fabrication, care should be taken to ensure that the elements with different orientations have identical shapes.

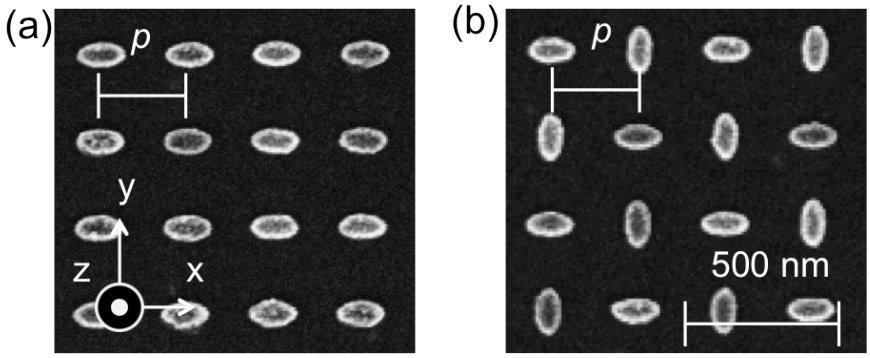

Fig. 4.3. Scanning electron micrographs of 30-nm-thick nickel elliptic disks with (a) uniform and (b) alternating orientation. Pitch p = 282 nm.

The magnetization dynamics in the elliptic disks were measured with the TR-MOKE setup described in section 3.3. The pump and probe pulses are focused onto spots with $1/e^2$ diameter of 10.2 μm and 5.7 μm, respectively, covering more than 300 elliptic disks within the effective probe beam diameter for the largest pitch p = 282 nm.

Micromagnetic simulations with OOMMF were implement for further interpretation of the experimental results. The disk arrays were modeled with cell size

smaller than 5×5×5 nm^3. The unit simulation cell consists of either a single elliptic disk for arrays of uniform orientation or of 2×2 nanomagnets for the alternating arrays (Fig. 4.4 shows examples). Periodic boundary conditions are utilized for accounting for the interelement dipolar coupling, characteristic to densely packed nanomagnet arrays. The saturation magnetization M_S = 341 kA/m and the Landé g factor g = 2.21 are obtained by fitting the precession frequency measured on a simultaneously deposited bare nickel film with Kittel equation (2.2.29) and used without further adjustment for the following analysis throughout this thesis. The somewhat low value of M_S comparing to common literature value (~485 kA/m at 300 K [173]) is attributed to the uncertainty in $\boldsymbol{H}_{app}$ in the setup and oxidization of nickel [174]. After initializing the magnetization state under the static external field $\boldsymbol{H}_{app}$, a small field pulse with the magnitude of 2 Oe and duration of 0.5 ps is applied for exciting the magnetization precession. The subsequent precessional motion is simulated with OOMMF for 2 ns and the z component of the magnetization evolution is analyzed in the same way as the experimental data.

4.3 Results and discussion

Representative results after background correction are presented in Fig. 4.4. At H_{app} = 2.0 kOe (H_{ip} = 1.0 kOe) applied at θ_H = 30° from the surface normal, the parallel (Fig. 4.4a) and perpendicular (Fig. 4.4b) elliptic disks revealed distinctly different precession frequencies at 6.6 and 3.5 GHz, respectively. The frequency discrepancy is explained with the different demagnetization field $\boldsymbol{H}_D$ in the elliptic disks for the two configurations. Fig. 4.4 shows the x component of $\boldsymbol{H}_D$ simulated in

the elliptic disks and surrounding space calculated at H_{app} = 2.0 kOe. At the center of the elliptic disks, $H_{D,x}$ was found to differ by ~340 Oe. The simulated $\boldsymbol{H}_D$ distributions show flexuous fringes at the ellipse edges, especially around the circumference crossing their minor axis. These fringes come from the step-wise change in the cuboid simulation meshes. In about 10 nm, however, $\boldsymbol{H}_D$ distribution becomes smooth and does not affect the simulated magnetization or the dipole coupling to the neighboring elements. In the alternating array (Fig. 4.4c), two clearly separated peaks are observed at similar frequencies. The simulated equilibrium state (Fig. 4.4) shows that $H_{D,x}$ distribution within elliptic disks with different orientations is qualitatively unchanged from the arrays with uniform orientation at p = 212 nm. The two Fourier peaks are attributed to the precession in two sublattices of elliptic disks with the orthogonal orientations. This demonstrates resolving the magnetization response from identically shaped nickel elliptic disks beyond the diffraction limit by means of dynamic separation.

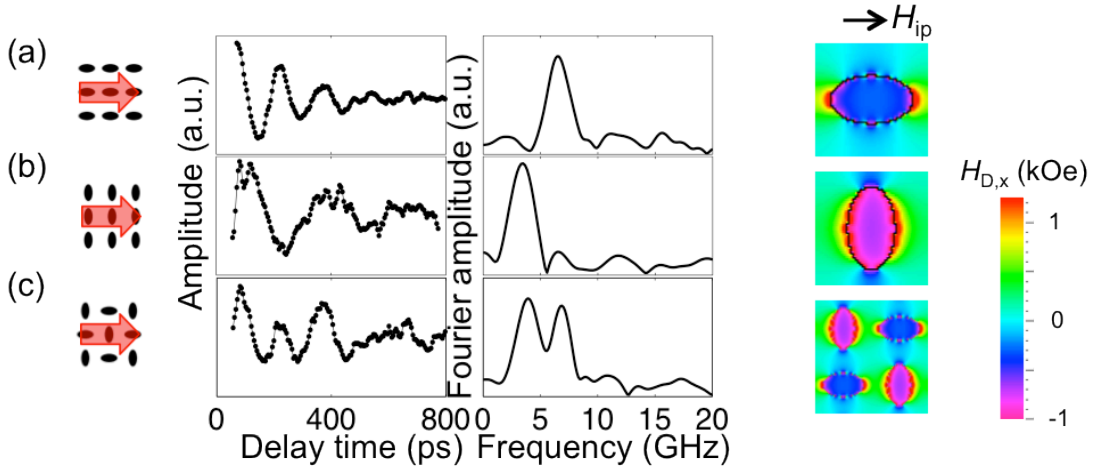

Fig. 4.4. (a–c) Representative TR-MOKE data from the nickel elliptic disks after background correction, measured at H_{app} = 2.0 kOe at θ_H = 30[a] from the surface normal (in-plance component H_{ip} = 1.0 kOe). In the sketches on the left side, the arrows represent the direction of $\boldsymbol{H}_{ip}$. (right) x component of simulated demagnetization field $\boldsymbol{H}_D$ in the ground state at H_{app} = 2.0 kOe (H_{ip} = 1.0 kOe).

To ensure the robustness of the measurements against error in field direction, we rotated the field orientation in xy plane between ϕ = 0°–90° and measured the uniformly oriented array with p = 212 nm. The obtained precession frequency is plotted against ϕ in Fig. 4.5. It remained unchanged within 0.1 GHz for a relatively large range of ϕ = 0°–15° and for ϕ = 75°–90°. The slight error in sample alignment, therefore, does not affect the results.

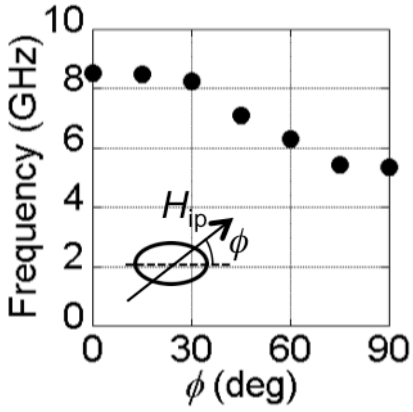

Fig. 4.5. The precession frequency measured on a uniformly ordered array with p = 212 nm as a function of the in-plance field direction ϕ. H_{app} = 2.75 kOe applied at θ_H = 30° from the surface normal.

The TR-MOKE responses measured at various H_{app} were converted to Fourier spectra and are presented in Fig. 4.6. Each spectrum has been normalized for better visualization of the mode frequency. The uniformly oriented elliptic disks parallel (Fig. 4.6a) and perpendicular (Fig. 4.6b) to H_{ip} show clear H_{app} dependence of the well-defined single peak over the wide field range. The observed frequencies were reproduced well with the micromagnetic simulations, shown with the dashed lines. The alternating array, on the other hand, exhibits two precession frequencies, attributed to the two subarrays of elliptic disks parallel and perpendicular to H_{ip} (Fig. 4.6c). The frequency peak positions from Fig. 4.6a and Fig. 4.6b were obtained with Gaussian peak fit and are also shown in Fig. 4.6c with open squares and crosses, respectively. By rotating the field in the xy plane to $\phi = 45°$, the two alternating subarrays become oriented to the same angle with respect to the applied field, resulting in degeneracy of the precession frequencies (Fig. 4.6d). In Fig. 4.6d, the open circles show the frequency peak positions from Fig. 4.6c, measured on the same array with the nondegenerate condition $\phi = 0°$. This verifies that the nanomagnets in the two subarrays are identically shaped. The entire array can be addressed correctively as in standard array measurements if desired.

The upper and lower branches in the alternating array (Fig. 4.6c) represent the subarrays of elliptic disks oriented parallel and perpendicular to $\boldsymbol{H}_{ip}$, respectively, and have similar frequencies observed in the uniformly arranged arrays (Fig. 4.6a and 4.6b). The precession frequencies in the alternating array (Fig. 4.6c) are

approximately 0.4 and 0.5 GHz higher than the corresponding mode frequencies measured in the uniform array (Fig. 4.6a and Fig. 4.6b), respectively. Qualitatively, this does not contradict the assumption that an elliptic disk in the alternating array and its counterpart in the uniformly oriented array experience different magnetostatic environment, predominantly determined by the orientation of its nearest neighbors. The micromagnetic simulations (dashed lines) show good overall agreement with the measured spectra. Small discrepancy between the measurements and simulations are attributed to uncertainty and variations of the nanomagnets' shape and size.

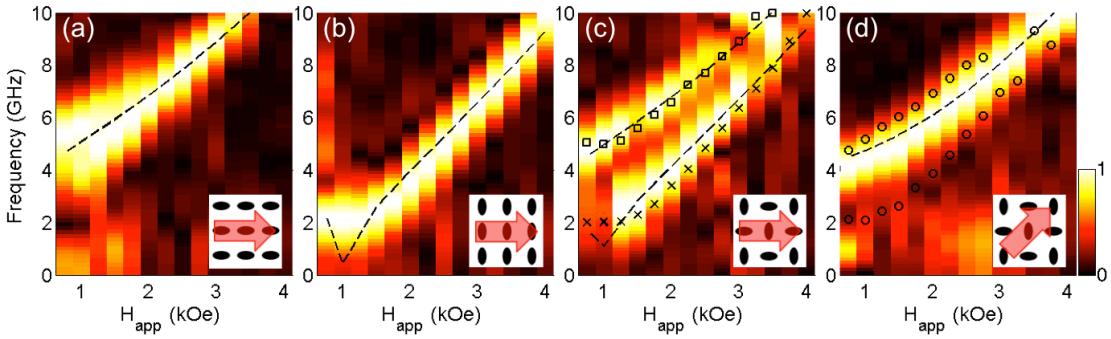

Fig. 4.6. Normalized Fourier spectra measured in nickel elliptic disk arrays with p = 212 nm. Fourier spectra in each pannel is normalized so that the highest peak has the value of 1. In the insets, the red arrow indicates the direction of $\boldsymbol{H}_{\text{ip}}$, the in-plane component of H_{app}.

To quantify the influence of the neighboring elements on the magnetization dynamics in nanomagnet subarrays, we repeated the measurements on a series of arrays with alternating orientation as a function of the center-to-center pitch p. The

resulting time traces were converted to Fourier spectra and are shown in Fig. 4.7 for p = 145, 212, and 282 nm. Each array show two frequency peaks corresponding to the precession of the two subarrays with parallel and perpendicular orientation.

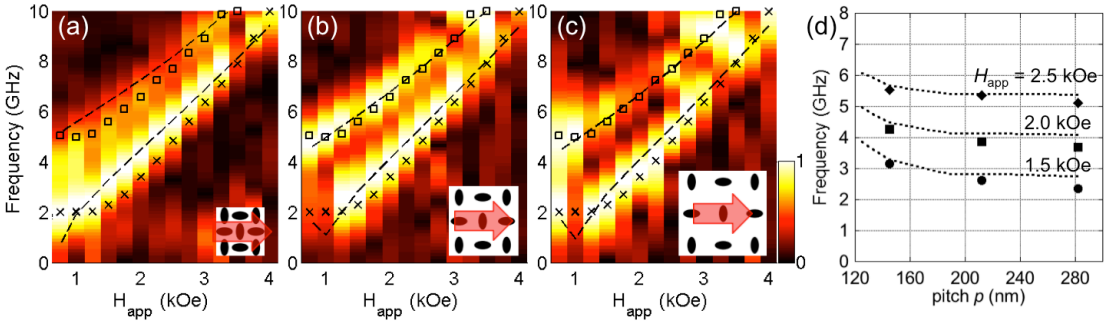

Fig. 4.7. Normalized Fourier spectra of the array of alternating orientation with various pitches p = (a) 145, (b) 212, and (c) 282 nm. Open squares and crosses represent the precession frequencies observed in the uniform array for p = 212 nm with ϕ = 0° and 90°, which have been shown to stay approximately constant for p > 165 nm in the measurements and in micromagnetic simulations. (d) Magnetization precession frequencies in the sublattice with perpendicular orientation in alternating arrays. Symbols are experimental values at various applied fields H_{app} = 1.50–2.50 kOe (in-plane component H_{ip} = 0.75–1.25 kOe), and the dotted lines show the simulated precession frequencies.

In the alternating array with the largest pitch p = 282 nm, the precession frequencies of the two subarrays are in good agreement with the micromagnetic simulations (dashed line). These frequencies are also close to their counterparts in the

uniformly oriented arrays. For p = 212 and 282 nm, the uniformly ordered arrays showed very similar precession frequencies and the values from p = 212 nm array are plotted in Fig. 4.7 with open squares and crosses. As the elliptic disks get closer to the neighboring elements with smaller p, the lower branch of the frequency peaks (subarray of elliptic disks perpendicular to $\boldsymbol{H}_{ip}$) increase monotonically, as seen in Fig. 4.7a–c.

This frequency shift is plotted in Fig. 4.7d along with the simulated precession frequency of the perpendicular subarray with various pitch p for H_{app} = 1.5–2.5 kOe (H_{ip} = 0.75–1.25 kOe). The simulations reproduced monotonically increasing precession frequency with smaller p due to the magnetostatic field from the neighboring nanomagnets, with similar shift for all applied field in both measurements and simulations. The shift is caused by the increased stray field from the neighbors. With the equilibrium magnetization distribution, the dipole field from the neighbors is 70 and 260 Oe for p = 212 and 145 nm, respectively. The simulations were performed for smaller and larger pitches. For p above ~190 nm, the magnetostatic correction to the precession frequency drops below 0.2 GHz in the simulations and becomes effectively negligible. On the other end, the frequency shift is expected to be above 1 GHz only at the pitch below ~140 nm. This corresponds to the separation of only a few nanometers and implausible to fabricate.

The experimental data exhibit a slightly larger frequency shift than the simulations, as observed in typical nanomagnet measurements [81]. We attribute this to the irregularity of shape, size, grain structure, and compositions of the actual

sample. The deviation from the ideal shape modeled in the simulations leads to nonuniform material parameters [76] and can cause significant changes in macroscopically observed magnetization dynamics.

While the dipole coupling with the neighboring nanomagnets resulted in the frequency shift, it turned out much smaller than the previous report with the nickel disks with two different sizes [81]. This is due to the reduced stray field from the thin (30 nm) nanomagnets unlike the thick (150 nm) magnets used in the previous study.

In the alternating array with p = 282 nm, the precession frequency shows pinning at ~9 GHz. We attribute this to the magnetoelastic coupling to surface acoustic waves and will discuss in more detail in Chapter 5.

4.4 Summary

We have demonstrated the dynamic separation method that resolves two different subarrays of nickel elliptic disks beyond the diffraction limit, depending on their orientation. Due to the different magnetostatic environment each nanomagnet is placed in, different subgroups of nanomagnets undergo magnetization precession at different frequencies. These precession modes are clearly separated in frequency domain and one can obtain the magnetization dynamics in each subgroup from a single corrective measurement. The effect of the neighboring elements was quantified by changing the array pitch p. Small but clear frequency shift was observed as a function of the element separation. The micromagnetic simulations reproduced the experimentally observed behaviors and showed the dipole field distribution explains the frequency shift in the arrays of nickel elliptic disks with alternating orientations.

Comparing to the first demonstration of dynamic separation by size [81], the work here handles more realistic array structure with all the elements with the identical shapes. Further work is proposed to handle the identically shaped elements with identical orientation but with different material parameters. While micromagnetic simulations of such structures predict sufficiently large frequency separation, this approach faces a fabrication challenge of embedding nanomagnets made of different materials in dense patterns. The realization of this experiment would yield the insights on the dipolar interelement coupling in practical device structures.

5. Magnetization dynamics coupled with surface acoustic waves

In this chapter, we will review the elastic oscillation modes excited in periodic nanostructures and its influence on the magnetization dynamics through the magnetoelastic coupling. Various examples of elastic mode excitation schemes and their effect on the magnetization responses will be discussed. We will introduce the magnetoelastic energy terms to expand the micromagnetics. At the end of the chapter, a simulation procedure for modeling the magnetoelastically coupled dynamics in nanomagnet arrays will be proposed. The theories and modeling techniques presented in this chapter will be utilized for analysis in Chapters 6 and 7, where we prove that the magnetoelastic coupling can dominate the magnetization dynamics in nanomagnet arrays and demonstrate applications of the effect for characterization and optimization.

5.1 Background

In TR-MOKE and similar pump-probe measurements, it has been repeatedly demonstrated that surface acoustic waves (SAWs) are generated by the optical pump pulses [175–178]. The excited SAWs modulate the reflectivity and are observed as strong oscillations in the TR-MOKE signal, often concealing the magnetization precession. Although the elastic modes can be coupled to the magnetization dynamics via the magnetoelastic effect, the interplay between phononic and magnetic modes generated in a nanostructured array had not been investigated. It was unclear whether

the observed SAW oscillations are a mere measurement shortcoming or indeed a magnetic response dominated by the magnetoelastic coupling. It is critical to answer this question in order to understand the experimental observations and to characterize nanomagnet responses with similar experimental setups. As a preparation for the quantitative investigation, the following sections review preceding studies on the relevant topics.

5.1.1 Magnetoelastic coupling and recent demonstrations in films

Several groups recently reported the experimental investigation of the effect of acoustic waves on the magnetization dynamics in planar films of ferromagnetic metals and semiconductors [147–152,179–186]. These studies demonstrated that the magnetoelastic coupling can be prominent enough to trigger magnetization precessions and even switch the magnetization direction. An example is shown in Fig. 5.1. A pump laser pulse is focused on an aluminum film on the back of a GaAs substrate. The rapid heating of the aluminum film generates the strain pulse, propagating through the substrate and reaching a (Ga,Mn)As film deposited on the front side. A probe laser is guided to the front side and records the magnetization precession of the (Ga,Mn)As film, superimposed with the reflectivity change due to the strain pulse. The strain pulse reaches and gets reflected from the front (Ga,Mn)As film at the time of 0–100 ps. After the strain pulse is reflected (after ~150 ps), a clear magnetization precession is observed with varying frequency with the applied field. Similar measurements were also conducted on a polycrystalline nickel film [151].

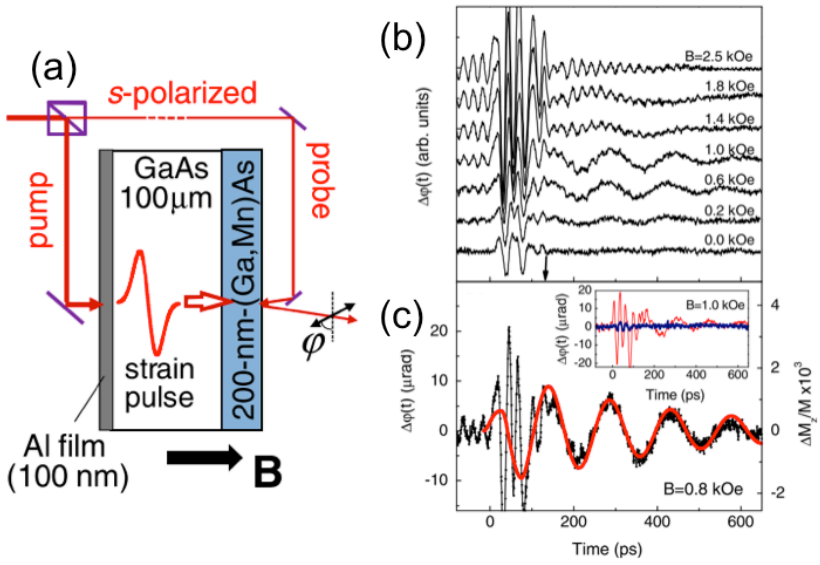

Fig. 5.1. (a) Schematic of pump-probe experiments with strain pulses. (b, c) Evolution of the Kerr rotation angle induced by the strain pulses. The vertical arrow indicates the time when the strain pulse leaves the (Ga,Mn)As layer. Inset: the Kerr rotation when the pump pulse was focused directly to the opposite of the probe pulse (thin red line) and displaced by 100 μm (thick blue line). Taken from [147].

Another configuration involves the surface acoustic waves (SAWs) generated with interdigitated transducers (IDTs) fabricated on piezoelectric substrate. An example is depicted in Fig. 5.2. An IDT is a set of comb-shaped metal strip lines fabricated on a piezoelectric substrate (typically $LiNbO_3$) with typical finger width on a micrometer scale. An RF voltage is applied between the two electrodes. This generates an electric field between the fingers and deforms the piezoelectric substrate with spatial periodicity, launching SAWs propagating perpendicularly to the IDT fingers. The fundamental SAW frequency is determined by the SAW velocity in the

substrate and the period of the IDT, typically in the sub-GHz range. Higher-order SAWs up to ~20th order [183] can also be excited by applying RF voltage at the frequencies of odd harmonics. Magnetic samples are fabricated to the side of the IDT and the SAW travels across the sample, exhibiting absorption of the acoustic energy peaked at the ferromagnetic resonance frequency. In [183] (Fig. 5.2), Weiler *et al* used another IDT on the other side of the nickel film to capture the transmitted SAW power and convert it to AC voltage. This technique provides stationary behavior of the magnetoelastic coupling. Typically, the dimension of the IDT (~ μm) limits the wavelength and the frequency of the SAWs generated to the low gigahertz range.

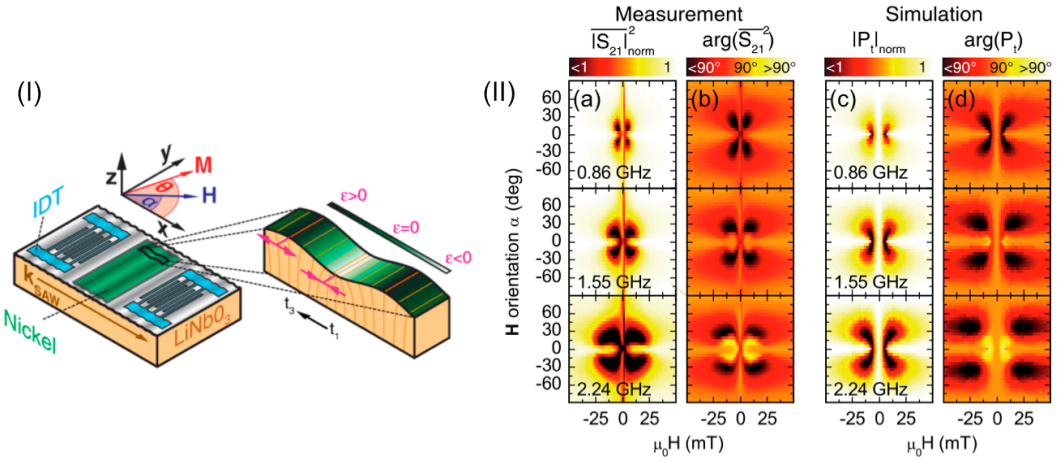

Fig. 5.2. (I) Interdigitated transducers on $LiNbO_3$ substrate and the nickel film fabricated for the elastically-driven ferromagnetic resonance experiments. The close up on the right illustrates the displacement and the strain in the nickel thin film. (II) Evolution of the SAW transmission detected with the second IDT as a function of the

magnitude and orientation of the external magnetic field. Columns (c) and (d) show the simulated SAW power density. Taken from [183].

5.1.2 SAW generation in arrays with a laser pulse

In addition to the IDTs described in the previous section, SAWs can also be generated with rapid heating with pulsed lasers. When a laser pulse is focused on a substrate surface, rapid thermal expansion of the structure launches strain waves. Similarly to the studies reviewed in section 5.1.1, a part of the energy goes to the bulk shockwave modes (mostly bulk longitudinal wave), propagating into the substrate. Additionally, another part is coupled to the pseudo surface acoustic wave modes (e.g., Rayleigh and surface skimming longitudinal waves). The wave propagation can be easily monitored with optical imaging or pump-probe spectroscopy and gives information on the sound velocity in the material. This method has thus been used as an acoustic characterization technique. Fig. 5.3 shows a demonstration of the surface acoustic waves generated in a gold film. A pump pulse of 150 fs pulse width is focused on a spot diameter ~ 2 μm on the gold film. The excited SAWs are monitored with a probe laser pulse with 830 nm center wavelength. Usually, in reflection configuration, the probe beam is most sensitive to the out-of-plane component of the displacement and does not detect the shear strain component effectively. In [187], Saito *et al* shined the probe beam from the backside and enhanced the sensitivity via much larger photoelastic effect on the light transmitted through the glass substrate. Fig. 5.3 clearly shows two concentric circles at the delay time of 11.7 ns. The inner

and outer circle represents the Rayleigh wave (RW) and the surface skimming longitudinal wave (SSLW), respectively. As will be discussed in section 6.2, this observation is essential in understanding the SAW spectra in our array structures.

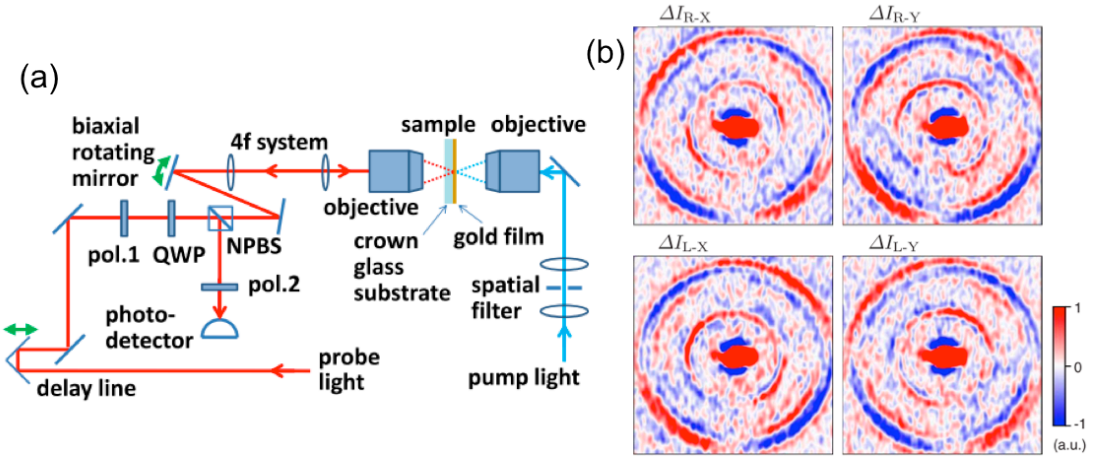

Fig. 5.3. Schematic diagram of the pump-probe experimental setup for SAW imaging through the photoelastic effect of the glass substrate. (b) Images of the optical intensity change at a pump-probe delay time of 11.7 ns, taken with various polarization configuration. The image area is 140 μm × 140 μm. The outer and inner rings represent the SSLW and the RW, respectively. Taken from [187].

The wavenumber and the frequency of the SAWs excited with this method are determined by the acoustic properties of the substrate. The typical SAW wavelength is in micrometers and the frequency is in the megahertz range. SAWs with much smaller wavelength in the gigahertz range can be excited by pulsed laser illumination on a periodic metallic structure. When the pump laser pulse irradiates an array or

grating of metallic elements, the absorbed laser energy causes impulsive thermal expansion of the nanoelements and induces elastic strain in the substrate, spatially modulated by the periodicity of the structure. This launches the SAWs propagating along the surface of the substrate. The SAWs propagate in all lateral directions and form standing waves, whose wavenumbers correspond to the reciprocal lattice points of the array geometry. When we neglect the mass loading from the metallic element, the fundamental SAW has the wavelength equal to the array pitch p and the frequency is determined as

$$f_0 = \frac{v}{p}, \tag{5.1.1}$$

where v is the SAW velocity. In one-dimensional arrays (gratings), there exist harmonic modes with frequencies $2f_0$, $3f_0$, and so on. In two-dimensional arrays, each of the standing SAW modes can be denoted with the indices (hk) on the basis of the primitive reciprocal lattice vectors of the array geometry. In a square array with an array pitch p, the SAWs have the frequency

$$f_{hk} = \sqrt{h^2 + k^2}\,\frac{v}{p}. \tag{5.1.2}$$

For example, the SAWs with the lowest indices (01), (11), (02), and (12) modes (and their degenerated modes) have the frequencies f_0, $\sqrt{2}f_0$, $2f_0$, and $\sqrt{5}f_0$.

Experimental demonstration of laser-excited elastic waves with periodic structures was already utilized in 1990s on one-dimensional gratings as well as two-dimensional arrays of nonmagnetic metallic nanoelements [188]. Lin *et al* shined a picosecond pulsed laser on gold gratings and disk arrays with 400–800 nm pitches,

fabricated on a SiO_2 substrate. In addition to the oscillations due to optical interference with the reflection from propagating elastic wave front, they found a mechanical mode independent of the probe beam incidence angle. They attributed this to the normal vibrational mode of the individual gold elements and not to the propagating SAWs. Even though they were aware of the mode frequency obeying Eq. (5.1.1), they found the perturbation analysis used for predicting RW inappropriate with the large mass loading of gold elements on light SiO_2 substrate and found the normal mode frequency comparable to that of the RW (the element dimension was kept proportional to the pitch).

Later, similar studies with better-controlled parameters have been carried out (e.g., [175–177]). In [176], for example, arrays of aluminum nanoelements with various sizes and pitches were studied with pump-probe spectroscopy. As summarized in Fig. 5.4, they found two families of vibrational modes (Type I and Type II). The Type I mode had large damping and little dependency on the array pitch while the frequency of Type II modes was inversely proportional to the pitch as Eq. (5.1.2). They attribute the Type I to the localized vibration of individual elements and the Type II to the RWs, propagating in various directions in two-dimensional arrays. In Fig. 5.4b, the SAW frequencies linearly trends with $1/p$ at low wavenumber but deviates from linearity at a large wavenumber. In the cases with small mass loading, Eq. (5.1.2) gives a good approximation of the SAW frequencies [175,177].

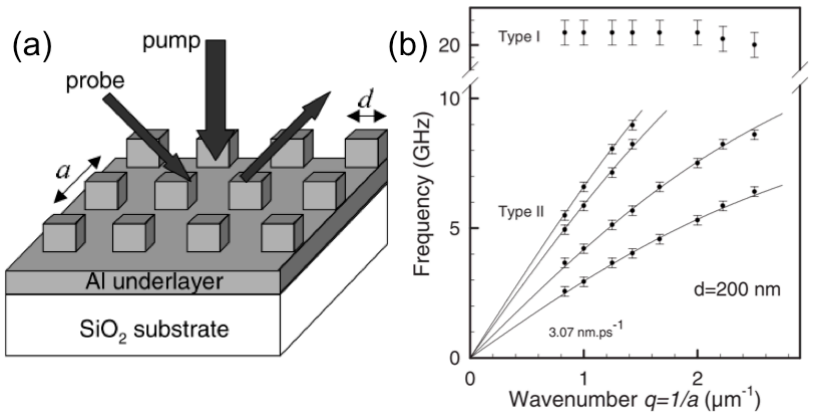

Fig. 5.4. (a) Schematic of SAW generation with ultrafast laser pump pulse in aluminum array nanostructure. (b) Frequency of mechanical modes obtained from aluminum array with d = 200 nm. Taken from [176].

With the development of numerical methods and greater computational power, more detailed analyses of nonuniform structures were made (e.g., [177]). With the finite element analysis of the mechanical eigenmodes, Giannetti *et al* demonstrated that the vibration of the free individual elements has much smaller eigenfrequencies than the observed frequency peaks, corroborating the excitation of the SAWs. The deviation of the frequencies from Eq. (5.1.2) was also computed by several groups. First, the perturbation theory with simplified geometry was used for modeling the change in SAW velocity [177,178,189]. Later, finite element analysis on the mechanical eigenvalue problem was carried out and revealed deviation of the spatial waveforms and frequencies [190,191]. Fig. 5.5 presents an example of nickel strips with p = 1 μm from [190], showing cos-like and sin-like SAW modes with

slightly different frequencies, as well as the frequency shift in sub-gigahertz range due to the mass loading.

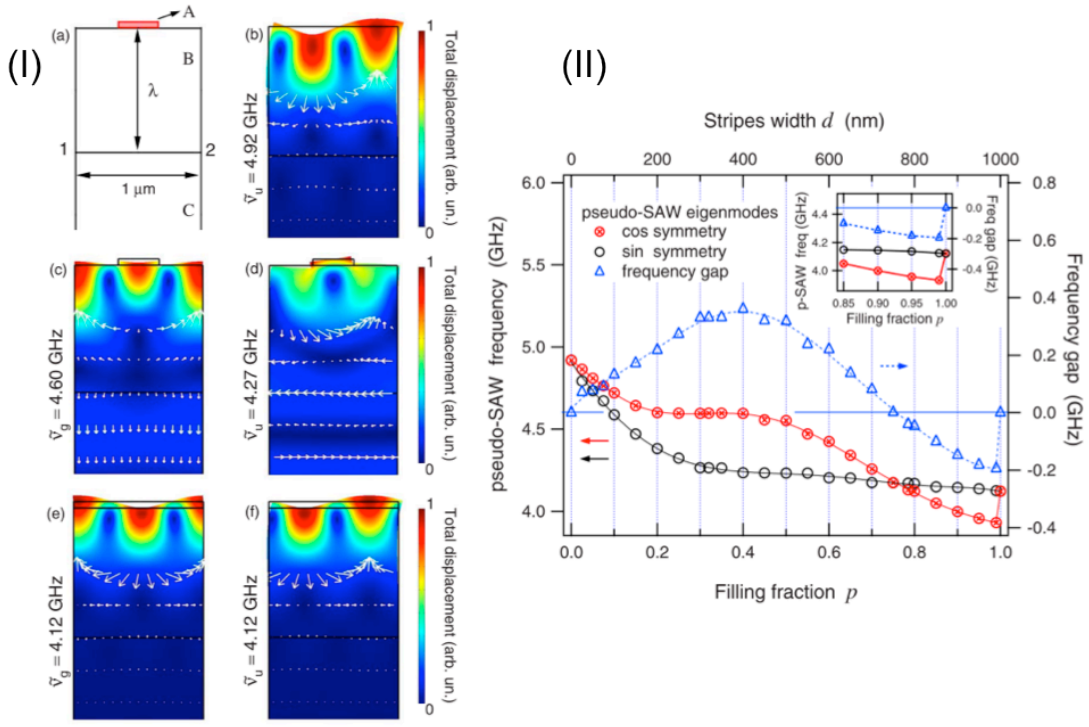

Fig. 5.5. (I) Various displacement eigenmodes simulated for nickel strips with the pitch p = 1 μm. (II) Frequency shift from the unperturbed SAW. Taken from [190].

As reported in [187], the Rayleigh waves (RWs) and the surface-skimming longitudinal wave (SSLW) are the two representative modes generated with pulsed laser illumination. The former has longitudinal and vertical shear components while the latter is dominated by the longitudinal component and has larger velocity. Strictly speaking, the SSLW, also known as the critically refracted longitudinal wave, is a bulk longitudinal wave mode that travels within an effective depth underneath the

surface [192]. Furthermore, both of them, in the presence of the surface perturbation, are also coupled to the bulk modes propagating into the substrate and dissipate energy, unlike the nondissipative surface eigenmodes that will be discussed in section 5.2.2. Nevertheless, when the element is relatively small and light, this additional energy dissipation is small and we loosely refer to them as the SAWs in this thesis.

5.2 Theories of linear elasticity

5.2.1 System of linear elasticity

Following the presentation of [108 pp. 311–314], we review a system of linear elasticity in this section. The elastic motion of a solid, like the assumption of micromagnetics, is treated as a continuous displacement vector $\boldsymbol{u}(\boldsymbol{r}) = \boldsymbol{r} - \boldsymbol{r}_0$ of the point $\boldsymbol{r}$ relative to its original position $\boldsymbol{r}_0$. The elastic strain and stress matrices are defined as

$$\varepsilon_{ij} = \frac{1}{2}\left(\frac{\partial u_i}{\partial x_j} + \frac{\partial u_j}{\partial x_i}\right), \tag{5.2.1}$$

where the indices i, j correspond to the Cartesian axes. For small displacement, Hooke's law

$$\sigma_{pq} = \sum_{l=1}^{3}\sum_{m=1}^{3} c_{pqlm}\varepsilon_{lm} \tag{5.2.2}$$

holds, where σ_{ij} is the Cauchy stress tensor. For an elastically isotropic medium, the system can be characterized with two independent moduli $c_{pppp} \equiv c_{11}$ and $c_{ppqq} \equiv c_{12}$, determining the third modulus as $c_{pqpq} \equiv c_{44} = (c_{11} - c_{12})/2$.

The system is also characterized with a different set of material parameters as

$$\sigma_{ij} = \delta_{ij}\left(\lambda\Delta\cdot\boldsymbol{u} - \frac{3E\alpha_{\mathrm{L}}}{1-2\nu}\Delta T_{\mathrm{l}}\right) + 2\mu\varepsilon_{ij}\,, \tag{5.2.3}$$

where E is the Young's modulus, ν is the Poisson ratio, $\alpha_{\mathrm{L}} \equiv (1/L)(\partial L/\partial T_{\mathrm{l}})$ is the linear thermal expansion coefficient, λ and μ are the Lamé parameters

$$\mu = \frac{E}{2(1+\nu)}, \quad \lambda = \frac{E\nu}{(1+\nu)(1-2\nu)}. \tag{5.2.4}$$

In (5.2.3), the thermal expansion due to the increase in lattice temperature ΔT_{l} is also included. The equation of motion of an elastic structure is expressed as

$$\rho\frac{\partial^2 u_i}{\partial t^2} = \sum_{j=1}^{3}\frac{\partial\sigma_{ji}}{\partial x_j}\,, \tag{5.2.5}$$

where ρ is the density of the material.

5.2.2 Elastic waves near solid surfaces

In the studies of seismology, various families of elastic waves were found to propagate near the surfaces of a solid. In addition to the primary (longitudinal) and secondary (transverse) plane waves, several types of steady elastic waves that are propagating along the free surface and attenuating rapidly along the depth of the half volume were shown to exist. The most common type of such waves is called the *Rayleigh wave* (RW) [193] and its displacement field is depicted in Fig. 5.6. The particle trajectories near the surface are ellipses with the major axis normal to the surface and the minor axis along the propagation direction. The displacement in the x direction is retarded by $\pi/2$ compared with the z direction. At the depth of about one

fifth of the wavelength, its x displacement becomes 0 and changes the rotation direction of the elliptic motion. This is an eigenmode of the system, so in the absence of frictional energy dissipation, the RW energy is perfectly confined near the free boundary.

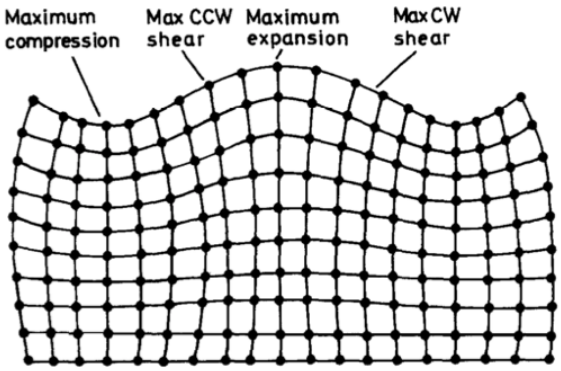

Fig. 5.6. Rayleigh surface wave particle displacement model. Taken from [194].

The Love wave is another example of surface acoustic waves and involves the motion of particles within the surface plane and perpendicular to the wave propagation. At an interface between two different solids, the linear elastic system supports the Stoneley wave. In a thin layer of finite thickness at a surface of half volume, Lamb waves also exist. They all are confined at the interfaces of the solid and exist as nondissipative eigenmodes. The detailed waveforms and dispersion law are found elsewhere [195].

As will be discussed later in Chapter 6, laser-generated RWs and SSLW with various propagation directions turned out to reproduce the observed oscillations very well in our TR-MOKE measurements in nanostructured metallic arrays.

5.3 Magnetoelastic effect

5.3.1 Magnetoelastic energy

The magnetoelastic effect was first known as *magnetostriction* in a narrow sense; a magnetically ordered material exhibits spontaneous strain caused by the magnetization [196]. The effect is characterized by the fractional change in length observed at the magnetization saturation, called the saturation magnetostriction λ_S. For crystals, it is anisotropic and characterized along various crystalline axes (e.g., λ_{100} and λ_{111} for cubic crystals). In a classical sense, the phenomenon can be understood as the deformation of the electron orbits in an effort to reduce the Zeeman energy density. With nonzero spin-orbit coupling, the change in the electron spin direction causes reorientation of the orbits, resulting in the reorientation of the crystalline axes. If the crystalline axes were fully rotated by 90º, this would cause an unrealistically large strain in the order of 10^{-1}. Realistically, magnetostriction is typically in the order of 10^{-5} [197 p. 21]. In typical 3d transition metals, small spin-orbit coupling causes reorientation of the crystalline axes by only a small angle. This energy term also leads to the reconfiguration of the magnetization under stress, called the *inverse magnetostriction*.

To unify these effects and model a magnetoelastic system, the Gibbs energy density is extended to include the magnetoelastic contribution. It is phenomenologically expressed as

$$U_{\mathrm{MEL}} = \frac{B_1}{M_S^2}\sum_p M_p^2 \varepsilon_{pp} + \frac{B_2}{M_S^2}\sum_p \sum_{q \neq p} M_p M_q \varepsilon_{pq}$$

$$+\frac{A_1}{M_S^2}\sum_p\sum_q\sum_{l\neq q}\frac{\partial M_p}{\partial x_q}\frac{\partial M_p}{\partial x_l}\varepsilon_{ql}+\frac{A_2}{M_S^2}\sum_p\sum_q\left(\frac{\partial M_p}{\partial x_q}\right)^2\varepsilon_{qq}\,, \tag{5.3.1}$$

where M_i are the magnetization component along axes x_i, and B_1, B_2, A_1, A_2 are the magnetoelastic constants [108 p. 315]. The latter two terms with A_1 and A_2 are determined by the spatial derivative of the magnetization and called the exchange terms. In most of the empirical studies previously reported, these terms are neglected and only the first two terms with B_1 and B_2 are considered [150,151,183,184,198–202]. As will be discussed in section 5.4, the exchange terms do turn out negligible in our case.

The magnetoelastic coefficients are related to the magnetostriction. In cubic crystals, the fractional elongation at the magnetization saturation along <100> and <111> directions is

$$\left(\frac{\delta l}{l}\right)_{100}\equiv\lambda_{100}=-\frac{2}{3}\frac{B_1}{c_{11}-c_{12}}$$

$$\left(\frac{\delta l}{l}\right)_{111}\equiv\lambda_{111}=-\frac{1}{3}\frac{B_2}{c_{44}}\,, \tag{5.3.2}$$

where c_{11}, c_{12}, and c_{44} are the moduli of elasticity for a cubic system, as described in section 5.2.1. In polycrystals, the bulk magnetostriction constant is obtained by a vector average of the randomly oriented axes as [97 pp. 343–357]

$$\lambda_{\text{poly}}=\frac{2}{5}\lambda_{100}+\frac{3}{5}\lambda_{111}\,. \tag{5.3.3}$$

In elastically isotropic media, including the polycrystals with sufficiently small grains, B_1 and B_2 become identical and can be related to the saturation magnetostriction λ_S and the shear modulus G as

$$B_1 = B_2 = -3\lambda_S G \,. \tag{5.3.4}$$

For hexagonal crystals, four magnetostriction constants λ_A through λ_D as defined in [196] are required for anisotropic parameterization. The macroscopic magnetostriction of polycrystals were derived by Birss as [203]

$$\lambda_{poly} = \frac{4}{15}\lambda_A - \frac{1}{3}\lambda_B - \frac{1}{3}\lambda_C + \frac{4}{5}\lambda_D \,. \tag{5.3.5}$$

In magnetoelastic modeling, two approaches have been proposed; the coupled equations of motion for the magnetoelastic systems and the *effective field approach*. The former is a rigorous expansion of elasticity and micromagnetics to include U_{MEL} but, due to its mathematical complexity, has only been applied to cases with simple configurations, e.g. a saturated isotropic bulk material with the magnetization and wave propagation in the film plane and parallel to each other. The latter, on the other hand, calculates the effective field in micromagnetics with U_{MEL} but neglects its influence on the elastic system, making it much simpler in computation. Since it neglects the energy transfer from the magnetization system to the elastic system, this approach may not be applicable in some cases. As will be discussed in the following sections, our work mostly uses the second approach but we first describe both in more details.

5.3.2 Magnetoelastically coupled system

In the first approach, the system is described with coupled equations of motion for elasticity and micromagnetics. The system has 6 components (u_x, u_y, u_z, M_x, M_y, M_z). In the following, we will derive a linearized equation of motion for small amplitude oscillation around an equilibrium.

Each of these two systems is now extended to include the contribution of the magnetoelastic energy density U_{MEL} in Eq. (5.3.1). In the elasticity, it appears as the Cauchy stress contribution $-\mathrm{d}U_{\mathrm{MEL}}/\mathrm{d}\boldsymbol{x}$. In micromagnetics, it is an effective field contribution $-\mathrm{d}U_{\mathrm{MEL}}/\mathrm{d}\boldsymbol{M}$. Here, let us assume an elastically isotropic material and no energy dissipation. By substituting the additional energy terms (5.3.1) into (2.2.2) and (5.2.5) and leaving up to the first order of $\boldsymbol{u}$ and $\boldsymbol{M}$, we obtain the coupled equations of motion

$$\frac{\partial M_x}{\partial t} = -\gamma \frac{B_2}{M_{\mathrm{S}}}\left(\frac{\partial u_y}{\partial x}+\frac{\partial u_x}{\partial y}\right)M_x - \gamma\left[H_{\mathrm{eff},z} - D\nabla^2 + 2\frac{B_1}{M_{\mathrm{S}}}\left(\frac{\partial u_y}{\partial y}-\frac{\partial u_z}{\partial z}\right)\right]M_y$$
$$+\gamma H_{\mathrm{eff},y}M_z - \gamma B_2\left(\frac{\partial u_z}{\partial y}+\frac{\partial u_y}{\partial z}\right)$$

$$\frac{\partial M_y}{\partial t} = -\gamma \frac{B_2}{M_{\mathrm{S}}}\left(\frac{\partial u_y}{\partial x}+\frac{\partial u_x}{\partial y}\right)M_y - \gamma\left[H_{\mathrm{eff},z} - D\nabla^2 + 2\frac{B_1}{M_{\mathrm{S}}}\left(\frac{\partial u_x}{\partial x}-\frac{\partial u_z}{\partial z}\right)\right]M_x$$
$$+\gamma H_{\mathrm{eff},x}M_z - \gamma B_2\left(\frac{\partial u_z}{\partial x}+\frac{\partial u_x}{\partial z}\right)$$

$$\rho\frac{\partial^2 u_x}{\partial t^2} = c_{44}\nabla^2 u_x + (c_{44}+c_{12})\frac{\partial}{\partial x}\nabla\boldsymbol{u} + \frac{B_1}{M_{\mathrm{S}}^2}\frac{\partial M_x^2}{\partial x} + \frac{B_2}{M_{\mathrm{S}}^2}\left[\frac{\partial}{\partial y}(M_xM_y)+\frac{\partial}{\partial z}(M_xM_z)\right]$$

$$\rho\frac{\partial^2 u_y}{\partial t^2} = c_{44}\nabla^2 u_y + (c_{44}+c_{12})\frac{\partial}{\partial y}\nabla\boldsymbol{u} + \frac{B_1}{M_{\mathrm{S}}^2}\frac{\partial M_y^2}{\partial y} + \frac{B_2}{M_{\mathrm{S}}^2}\left[\frac{\partial}{\partial z}(M_yM_z)+\frac{\partial}{\partial x}(M_yM_x)\right]$$

$$\rho\frac{\partial^2 u_z}{\partial t^2} = c_{44}\nabla^2 u_z + (c_{44}+c_{12})\frac{\partial}{\partial z}\nabla \boldsymbol{u} + \frac{B_1}{M_S^2}\frac{\partial M_z^2}{\partial z} + \frac{B_2}{M_S^2}\left[\frac{\partial}{\partial x}(M_z M_x) + \frac{\partial}{\partial y}(M_z M_y)\right],$$

(5.3.6)

where the third component of the magnetization M_y has been omitted since it can be obtained via the conservation of the magnetization magnitude $|\boldsymbol{M}| = M_S$.

To obtain the dispersion of small amplitude magnetoelastic modes, the coupled equations of motion (5.3.6) are linearized. Here, as a simple example, we assume that the material is saturated along the z axis and the wave vector is parallel to the magnetization. We assume the solution of the form

$$M_p = M_{0p}\exp\left(i(\omega t - \boldsymbol{k}\cdot\boldsymbol{r})\right)$$

$$u_p = u_{0p}\exp\left(i(\omega t - \boldsymbol{k}\cdot\boldsymbol{r})\right) \qquad (5.3.7)$$

for $p = x, y, z$ and substitute them into (5.3.6). Five coupled linear algebraic equations result. Maintaining up to the first order terms in $\boldsymbol{M}$ and $\boldsymbol{u}$, (5.3.6) is linearized as

$$i\omega M_x + \gamma(H_0 + Dk^2)M_y - i\gamma k B_2 u_y = 0$$

$$i\omega M_y + \gamma(H_0 + Dk^2)M_x + i\gamma k B_2 u_x = 0$$

$$(\omega^2\rho - k^2 c_{44})u_x - ik\frac{B_2}{M_S}M_x = 0$$

$$(\omega^2\rho - k^2 c_{44})u_y - ik\frac{B_2}{M_S}M_y = 0$$

$$(\omega^2\rho - k^2 c_{44})u_z = 0 \qquad (5.3.8)$$

Here, the subscript 0 has been omitted from the complex amplitudes M_i and u_i. Note that u_z is decoupled from the rest of the equations and represents a purely elastic

longitudinal wave mode. The other four equations are coupled. Turning the variables to a circularly polarized system $M_\pm = M_x \pm iM_y$ and $u_\pm = u_x \pm iu_y$, representing the right-hand and left-hand circularly polarized waves, the equations become two linear equations

$$A_\pm \begin{bmatrix} M_\pm \\ u_\pm \end{bmatrix} = \begin{bmatrix} i\omega \mp i\omega_{\mathrm{m}} & \mp\gamma k_z B_2 \\ -i\dfrac{k_z B_2}{M_{\mathrm{S}}} & \rho\left(\omega^2 - \omega_{\mathrm{el}}^2\right) \end{bmatrix} \begin{bmatrix} M_\pm \\ u_\pm \end{bmatrix} = \boldsymbol{0}, \tag{5.3.9}$$

where $\omega_{\mathrm{m}} = \gamma(H + Dk^2)$ is the frequency of the unperturbed spin wave and $\omega_{\mathrm{el}} = \sqrt{c_{44}/\rho}\,k$ is the frequency of the unperturbed transverse elastic wave. In order for the above equation to have a single set of solutions, the determinant of the coefficients must vanish (self-consistency condition). From this condition, the dispersion relation is obtained as

$$\det A_\pm = \rho(\omega \mp \omega_{\mathrm{m}})(\omega^2 - \omega_{\mathrm{el}}^2) \mp \frac{\gamma B_2 k^2}{M_{\mathrm{S}}} = 0\,. \tag{5.3.10}$$

The dispersion curve (5.3.10) calculated with nickel parameters under the field of 2.5 kOe is shown in Fig. 5.7. The three magnetoelastically coupled modes are shown. Due to the directionality of the torque on the magnetization (the first term in (2.2.1) and (2.2.2)), the right-hand and left-hand circularly polarized magnetoelastic waves exhibit qualitatively different behaviors. Apart from the crossover point at $k \approx 1.8 \times 10^5$ cm^{-1}, they closely follow the unperturbed spin and elastic modes, whose frequencies are proportional to k^2 and k, respectively.

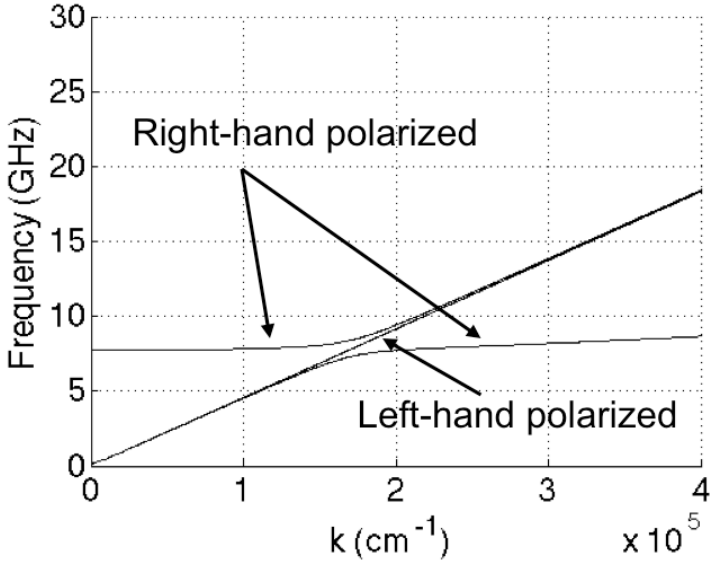

Fig. 5.7. Dispersion curves of the magnetoelastic modes calculated with Eq. (5.3.10) for the applied field H = 2.5 kOe.

This is a rigorous extension of elastic and micromagnetic theories and can correctly predict the coupling phenomena between elasticity and magnetism, including the mode repulsion and the phase change at the crossover points. However, this approach involves complex mathematical formulae that can be analytically solved only in several simple configurations. Particularly, solving the consistency condition for the dispersion curve quickly becomes overcomplicated with nonuniform strain waves or with arbitrary magnetization direction. Therefore, the analysis of the RWs, which inevitably consist of multiple components of displacement, can only approximately be addressed in simple structures, such as films, and with various simplifying assumptions. Ref [183], for example, needed to introduce a "filling factor", which served as a fitting parameter to bring the calculation close to the

experimental results and assume an arbitrarily conjectured wave form to emulate the RWs. Of course, it is possible to build a numerical simulation framework to solve the coupled equation directly, with time integration of Eq. (5.3.6). However, due to the nonlocal characteristic of demagnetization field calculation, this necessitates fundamental modification of known genetic FEM or micromagnetic simulation frameworks and it has not been reported. In addition, the coupled equations approach would compute the elastic motion every time the simulation is done, while the effective field approach, as will be discussed in the next section, calculates the elastic motion only once and repeatedly use it in the following magnetization simulations. An alternative would be to solve Eq. (5.3.8) or its equivalent derived for different configurations of $\boldsymbol{M}$ and $\boldsymbol{k}$ as an eigenvalue problem. As reported for purely magnetic problems [204,205], this may turn out an efficient computation method to simulate the magnetoelastically coupled dynamics in nanostructures.

5.3.3 Effective field approach

The second approach is to obtain the effective field due to the magnetoelastic contribution and include it in the standard micromagnetic calculations. It neglects the influence of the magnetization on the elastic system (sometimes called “backaction”) but has an important advantage; it has simple implementation and, under the restriction of small precession amplitude, we do not even need to modify the existing micromagnetic simulation framework.

The magnetoelastic contribution $\boldsymbol{H}_{\mathrm{MEL}}$ to the effective magnetic field $\boldsymbol{H}_{\mathrm{eff}}$ is obtained via the variational derivative

$$\boldsymbol{H}_{\mathrm{MEL}} = -\frac{1}{\mu_0}\frac{\delta U_{\mathrm{MEL}}}{\delta \boldsymbol{M}} = -\frac{1}{\mu_0}\frac{\partial U_{\mathrm{MEL}}}{\partial \boldsymbol{M}} + \sum_i \frac{\partial}{\partial x_i}\left[\frac{\partial U_{\mathrm{MEL}}}{\left(\partial \boldsymbol{M}/\partial x_i\right)}\right]. \tag{5.3.11}$$

The summation in Eq. (5.3.11) is nonzero only with the presence of the exchange terms (A_1 and A_2 terms) in (5.3.1). When they can be neglected, only the first term in (5.3.11) needs to be evaluated, leading to an $\boldsymbol{H}_{\mathrm{MEL}}$ expression as

$$\boldsymbol{H}_{\mathrm{MEL}} = \begin{bmatrix} -\dfrac{2B_1}{M_S^2}M_x\varepsilon_{xx} - -\dfrac{2B_2}{M_S^2}\left(M_y\varepsilon_{xy} + M_z\varepsilon_{xz}\right) \\ -\dfrac{2B_1}{M_S^2}M_y\varepsilon_{yy} - -\dfrac{2B_2}{M_S^2}\left(M_x\varepsilon_{xy} + M_z\varepsilon_{yz}\right) \\ -\dfrac{2B_1}{M_S^2}M_z\varepsilon_{zz} - -\dfrac{2B_2}{M_S^2}\left(M_x\varepsilon_{xz} + M_y\varepsilon_{yz}\right) \end{bmatrix}. \tag{5.3.12}$$

The magnetization evolution can be calculated with a standard micromagnetic simulation with (5.3.12) as an additional effective field contribution. If the precession amplitude is small, $\boldsymbol{H}_{\mathrm{MEL}}$ can be calculated beforehand with a static $\boldsymbol{M}$, obtained at the equilibrium magnetization distribution. The micromagnetic simulation can be carried out by reading the previously computed $\boldsymbol{H}_{\mathrm{MEL}}$ and no modification to the micromagnetic simulation is necessary. Alternatively, $\boldsymbol{H}_{\mathrm{MEL}}$ can be evaluated at each simulation step. More details in simulation implementation are given in section 5.4.

The simplification of neglecting the backaction has successfully been used to analyze the magnetoelastic dynamics in nickel films [183,184]. In our observations, as will be discussed in Chapter 6, it is also justified by the fact that the nonmagnetic signal shows no observable change at the crossover points, where the coupling between the magnetic and elastic systems becomes the strongest.

5.4 Magnetoelastic simulation procedure

In order to elucidate the magnetoelastic dynamics in arbitrary structures and configurations, we developed a multistep simulation procedure. First, heating of the nanomagnet is modeled with the three-temperature model [136] and computed with finite element method (FEM), as illustrated in section 3.2.1. Second, the subsequent elastic motion due to the thermal expansion is computed with time integration of Eq. (5.2.5). The effective field due to the magnetoelastic energy is then calculated with Eq. (5.3.12) and added in the micromagnetic simulation using OOMMF micromagnetic simulator. Once the material parameters are known, this procedure quantitatively predicts the magnetoelastic effect. Below, each step and its limits are discussed in more detail.

The first step is determining the temperature rise in the nanomagnet after irradiation by the pump pulse, using the three-temperature model introduced in section 3.2.1. The absorbed pump energy density per unit time $P_{\text{abs}}(\boldsymbol{r},t)$ is obtained by calculating the reflection and absorption of the pump with the complex refractive index $\tilde{n} = n + ik$. When the absorbing layer is sufficiently thicker than the optical absorption depth $\zeta = \lambda/4\pi k$, the absorbed power density is modeled as

$$P_{\text{abs}}(z,t) = \frac{1}{\zeta} S(t) e^{-\frac{z}{\zeta}} = (1-R)\frac{1}{\zeta} S_{\text{in}}(t) e^{-\frac{z}{\zeta}}, \tag{5.4.1}$$

where $R = \left|(\tilde{n}-1)/(\tilde{n}+1)\right|$ is the reflectivity of the metal calculated with Snell's law. For the 30-nm-thick nickel ellipses with $\tilde{n} = 1.61 + 2.36i$ at λ = 400 nm, the optical absorption depth is ζ = 13.5 nm and this gives a reasonable approximation of the

absorbed pump power. However, samples often have multiple layers, including the AR coating, seed layer, and capping layer and care should be taken to justify this simple approach. For example, if the AR coating layer under the nanomagnet is transparent at the pump wavelength, it may get reflected at the bottom of the AR coating and alter the distribution of the absorbed pump fluence across the magnetic layer. This can be accurately addressed with the transfer matrix method described elsewhere [167]. In the case of the 30-nm-thick nickel ellipses with a 110 nm hafnium oxide AR coating, this effect turned out to be relatively small (less than 10%) and it is ignored here.

The rate equations (3.2.1) are discretized in space with a tetrahedral finite element mesh and the time evolution is addressed by the explicit Euler method. A time step of 0.1 ps was chosen by checking the consistency of simulation results with various time steps. The resulting temperature evolution in a nickel elliptic disk is shown in Fig. 5.8 for the peak fluence of F = 0.78 mJ/cm^2 and 200 fs FWHM duration of the Gaussian pump pulse. The temperature evolution turned out virtually constant across the lateral direction within the magnet. Therefore, as a measure to reduce the computational time, we further simplified the time evolution of the lattice temperature by fitting it at the top, middle, and bottom of the nanomagnet with equations

$$T_{\mathrm{l,center}} = A_1\left(1-\exp(-t/A_2)\right)+T_{\mathrm{l},0}$$

$$T_{\mathrm{l,top}} = T_{\mathrm{l,center}} + A_3\left(1-\exp(-t/A_4)\right)\exp(-t/A_5)$$

$$T_{\mathrm{l,bototm}} = T_{\mathrm{l,center}} + A_6\left(1-\exp(-t/A_7)\right)\exp(-t/A_8), \qquad (5.4.2)$$

where $T_{l,i}$ are the lattice temperature obtained at the top, center, and bottom of the nickel elliptic disk and A_i are the fitting parameters. Table 5.1 shows representative fitting parameters A_i for nickel and cobalt elliptic disks with F = 0.78 mJ/cm^2. The resulted fitting curves for nickel are also shown in Fig. 5.8. In the subsequent elastic simulation, the vertical distribution of T_l is approximated by linear interpolation of (5.4.2). The lattice temperature T_l is also found proportional to the peak pump fluence, eliminating need for further simulations in case different pump fluence is used. This is done primarily for eliminating the need for simulating the temperature evolution at every step of the following elastic simulation. If higher accuracy in T_l with complex spatial distribution is needed, it can be modified in a way that the temperature simulation records the distribution of T_l at a fixed time step and the following elastic simulation reads those results and interpolates them in order to approximate the T_l distribution.

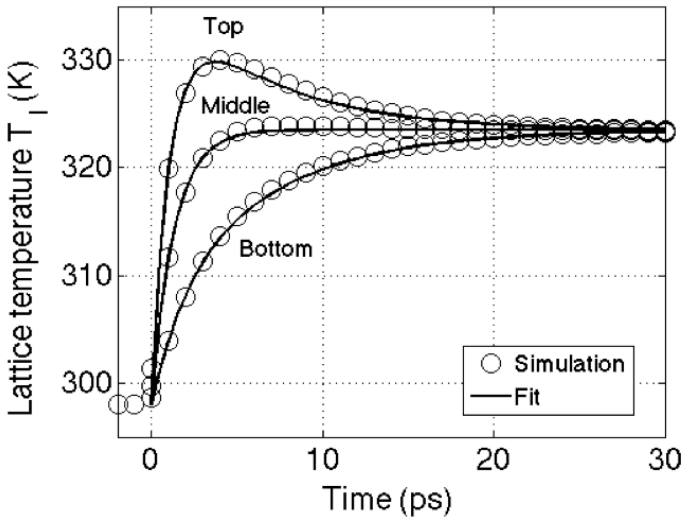

Fig. 5.8. Lattice temperature evolution simulated in a nickel elliptic disk with the pump fluence of F = 0.78 mJ/cm^2 and 200 fs FWHM pulse duration. The solid lines are the fit with Eq. (5.4.2) with the fitting parameters listed in Table 5.1.

	A_1 (K)	A_2 (ps)	A_3 (K)	A_4 (ps)	A_5 (ps)	A_6 (K)	A_7 (ps)	A_8 (ps)
Nickel	25.5	1.31	14.8	0.924	5.97	-17.7	1.41	6.36
Cobalt	61.5	0.327	36.5	0.200	7.15	-32.1	0.254	8.08

Table 5.1. Fitting parameters for approximating the lattice temperature using Eq. (5.4.2). Pump fluence of F = 0.78 mJ/cm^2 and 200 fs FWHM pulse duration is assumed.

Subsequently, excitation of SAWs is simulated using the finite element method. The thermal expansion is included in the equation of motion of linear elasticity (5.2.5) and the time evolution of the displacement is simulated with the explicit Euler method, with time discretization Δt and finite difference approximation

$$\frac{\partial^2 \boldsymbol{u}^k}{\partial t^2} = \frac{\boldsymbol{u}^k - 2\boldsymbol{u}^{k-1} + \boldsymbol{u}^{k-2}}{\Delta t^2}. \tag{5.4.3}$$

The unit cell of a typical simulated structure is shown in Fig. 5.9. It consists of the substrate, a 110-nm-thick AR coating layer (hafnium oxide), and a nickel elliptic disk. The sidewalls of the substrate and AR coating layer adopt the periodic boundary conditions and represents infinite repetition in a rectangular array. As T_l simulated

from the previous step is applied, the nanomagnet expands and launches strain pulses into the substrate and the AR coating layer. Apart from the SAWs, a bulk longitudinal wave is launched into the substrate and eventually gets reflected from the bottom of the simulation structure. In order to avoid the effect of the reflected bulk waves, the substrate is taken to be long enough (12 μm in this case). An alternative modification would add a perfectly matched layer (PML) at the bottom boundary [206]. The SAWs are confined approximately within their wavelength, thus their characteristics are dominated by the elastic properties of the AR coating layer, which has been commercially evaporated on p-doped silicon wafers. In order to determine the material parameter for the AR coating, we assumed a literature value of the density ρ = 9.68 g/cm^3 and ran multiple simulations with various Young's modulus E. The three lowest RW frequencies in the resulted simulations were compared with the experimentally observed values (f = 12.2, 15.8, and 22.3 GHz) and a best value of E = 161 GPa was determined with the least square method. It has been confirmed that change in the Poisson ratio ν makes little difference to the SAW frequencies and we assumed ν = 0.3.

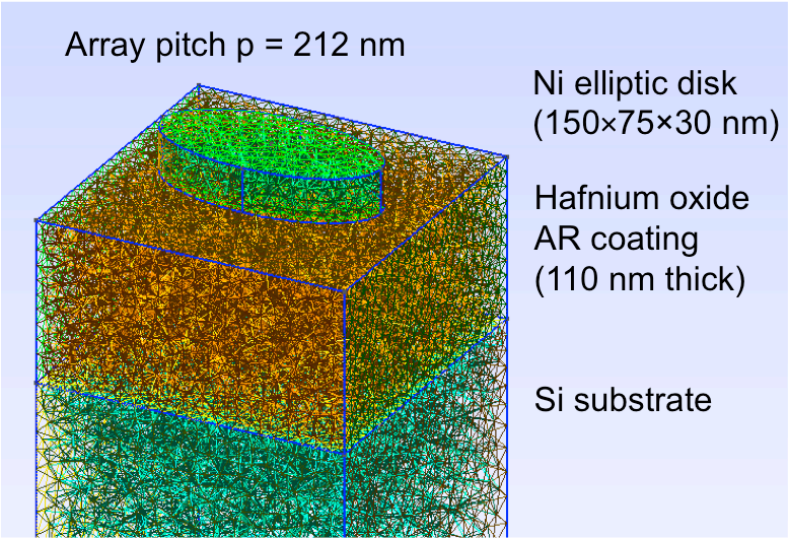

Fig. 5.9. Example of a tetrahedron mesh for elastic simulations. 30-nm-thick nickel elliptic disks with the major and minor diameters of 150 and 75 nm, respectively, on a 110-nm-thick hafnium oxide antireflection coating layer are modeled. The side walls of the substrate utilize the periodic boundary condition and represent an infinite array with the pitch p = 212 nm.

The representative simulation results are shown in Fig. 5.10. Fig. 5.10a shows change in u_z at the center of the magnet and its Fourier transform, as described in section 3.4. With Eq. (5.3.12), $\boldsymbol{H}_{\mathrm{MEL}}$ was calculated at the center of the elliptic disk for H_{app} = 4.0 kOe and its x component is displayed in Fig. 5.10b. Fig. 5.10c–f displays several snapshots of the simulated elastic motion at various time t after pump pulse excitation, with the displacement emphasized by a factor of 1500. In Chapter 6, the results of the elastic simulations will be discussed in more detail in comparison with the experimental results.

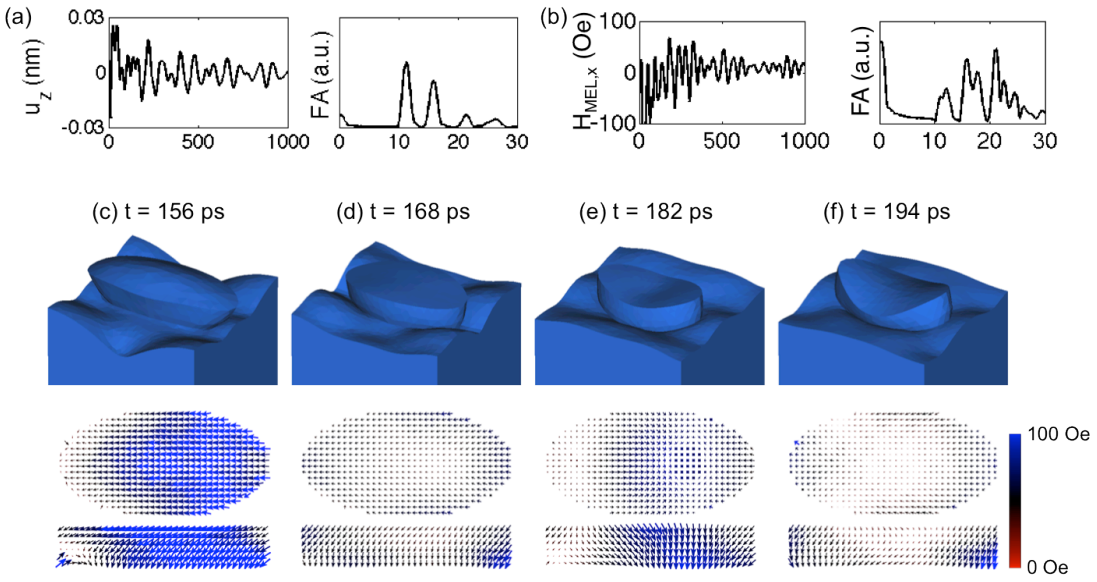

Fig. 5.10. (a) Example of the simulated displacement u_z at the center of the nickel elliptic disk and its absolute Fourier amplitude spectrum. (b) x component of the magnetoelastic field $\boldsymbol{H}_{\mathrm{MEL}}$ calculated with Eq. (5.3.12) at H_{app} = 4.0 kOe applied at θ_{H} = 30º from the surface normal. $\boldsymbol{H}_{\mathrm{MEL}}$ was calculated assuming that the initial magnetization distribution remains near constant throughout the simulation. (c–f) Snapshots of the simulated displacement at t = 156, 168, 182, and 194 ps after pump excitation (top row) and the calculated magnetoelastic field $\boldsymbol{H}_{\mathrm{MEL}}$. The displayed displacement is amplified by a factor of 1500.

Once we have the elastic strain, obtained by Eq. (5.2.1) and the simulated displacement $\boldsymbol{u}$, we can calculate the magnetoelastic contribution to the system with Eq. (5.3.12) and can add it in the micromagnetic simulations. As discussed in section 5.3.3, this approach neglects the backaction of the magnetization dynamics on the

elastic motion. We justify this by an example of the successful magnetoelastic analysis in nickel films [183,184] and by the fact that we found no observable change in the nonmagnetic signal in the experiments, as will be discussed in the next chapter.

Omission of the exchange terms with A_1 and A_2 in U_{MEL} (5.3.1) is justified as follows. The exchange magnetoelastic constant $A_{1,2} = \partial A_{ex} / \partial \varepsilon_{ii}$ is estimated with dependence of the exchange stiffness constant A_{ex} on the normal strain under uniform compression with pressure P. With $A_{ex} = 4JS^2/a$, $T_c = 8JS(S+1)/k_B$ and $dT_c/dP = 3.45\times10^{-9}$ K Pa^{-1} [207], where J is the exchange integral, $S = 1$ is the spin angular momentum quantum number, $a = 0.354$ nm is the lattice constant, and k_B is Boltzmann constant,

$$A_{1,2} = \frac{4S^2}{a}\frac{k_B E}{8S(S+1)(1-2\nu)}\frac{\partial T_C}{\partial P} = 1.77\times10^{-11} \text{ J m}^{-1}. \quad (5.4.4)$$

Using the ground state magnetization simulated for a nickel elliptic disk, additional U_{MEL} terms were calculated and confirmed to be less than a percent of the first two terms in Eq. (5.3.1). Therefore, the exchange terms are negligible in our simulations and $\boldsymbol{H}_{MEL}$ is evaluated with Eq. (5.3.12).

The actual implementation is achieved in two different ways. First, $\boldsymbol{H}_{MEL}$ was calculated using Eq. (5.3.12) assuming magnetization in a ground state and stored in a series of vector field distribution files. Typically, for a simulation for 1 ns, $\boldsymbol{H}_{MEL}$ is evaluated for every 2 ps, generating 500 files. These files are then called from an OOMMF time evolver every 0.2 ps, linearly interpolating the successive two files to

provide smoother evolution in $\boldsymbol{H}_{\mathrm{MEL}}$. This time scale is chosen to be much smaller than the typical period of the magnetization precession (10–200 ps).

In the second implementation, OOMMF's energy object classes were extended to include the magnetoelastic energy contribution, calculating $\boldsymbol{H}_{\mathrm{MEL}}$ at each simulation step. Multiple extension modules were developed to handle various demands for magnetoelastic simulation with time-varying, spatially nonuniform elastic strain. The extension is now publicly available [208]. This makes it unnecessary to store $\boldsymbol{H}_{\mathrm{MEL}}$ distribution in files and saves a lot of disk space (often tens of gigabytes). Greater simulation flexibility and smoother $\boldsymbol{H}_{\mathrm{MEL}}$ evolution are achieved. This implementation is especially advantageous when the magnetization deviates from its equilibrium state during the simulation. It runs at a comparable speed as the former implementation and generate consistent results when the precession amplitude is sufficiently small. In both implementations, as discussed in section 2.3, the speed of micromagnetic simulations is limited by the computation of the long-range demagnetization field and the additional calculation of $\boldsymbol{H}_{\mathrm{MEL}}$ only has a minor impact on the total simulation time.

6. Magnetoelastically coupled magnetization dynamics in nickel nanomagnet arrays

Here, we show that the surface acoustic waves (SAWs) generated in nanostructures are indeed interacting with the magnetization dynamics and that even if you perfectly filter out the nonmagnetic reflectivity change from the TR-MOKE signal, you still see a strong effect of the elastically driven oscillations on magnetization dynamics. The magnetoelastic coupling ”pins” the magnetization precession at the SAW frequencies over a wide field range and causes an enhancement of the Fourier amplitude at the crossover fields, where the intrinsic mode crosses the magnetoelastic modes driven by the SAWs. The nature of these coupled modes is investigated by changing the array geometry. Using finite element analysis of the elastic motion and micromagnetic simulations with a magnetoelastic contribution, the experimental observations are reproduced. The origins and spatial modes are also characterized and discussed in detail. The major findings in this Chapter have been reported in [209].

6.1 Samples and experimental details

To investigate the magnetoelastic dynamics in patterned nanomagnets, various patterns were fabricated at the Molecular Foundry at Berkeley. Nickel and aluminum nanoelements with 30 nm thicknesses were fabricated using electron beam lithography, electron beam evaporation, and liftoff. A commercially deposited 110-nm-thick hafnium oxide AR coating was deposited in order to help maximize the

optical SNR by reducing the reflection from the trench [168]. Elliptic disks with major and minor axes of 140 and 80 nm, respectively, were fabricated with various array pitches p. In section 6.2, these elliptic disks will be discussed for the first demonstration of the magnetization precession magnetoelastically coupled to the SAWs. In section 6.4, nickel squares will also be characterized. Fig. 6.1 shows scanning electron micrographs of representative arrays.

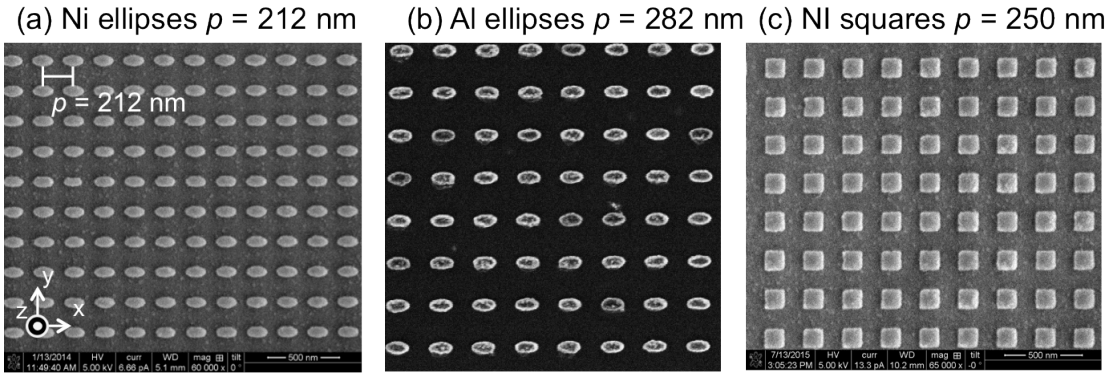

Fig. 6.1. Scanning electron micrographs of nickel and aluminum elliptic disks (a, b) and nickel squares (c).

The magnetization dynamics and nonmagnetic elastic responses were measured with the TR-MOKE system described in section 3.3. The pump and probe beams were focused to the $1/e^2$ diameter of 10.2 and 5.7 μm, respectively, covering more than 300 elliptic disks within the effective probe beam diameter for p = 282 nm. The difference and sum of the two balanced photodetectors were recorded as the magnetic (difference channel) and nonmagnetic (sum channel) signal. In this chapter,

like in Chapter 4, the decaying background in the TR-MOKE time traces has been subtracted from the displayed results.

6.2 Magnetoelastic modes in TR-MOKE measurements

6.2.1 Magnetoelastically coupled modes in nickel elliptic disks

The representative TR-MOKE signal after background correction is presented in Fig. 6.2, taken at H_{app} = 2.5 kOe applied at θ_H = 30° from the surface normal. Fig. 6.2a–c exemplify the optical response from three sample types. The magnetic (difference) and nonmagnetic (sum) signals along with their Fourier spectra are shown. The vertical axes of the magnetic and nonmagnetic signal are identical for each pair. The nickel film (Fig. 6.2a) shows a clean single-frequency damped oscillation, identified as the Kittel mode [210]. The absence of any oscillations in the nonmagnetic signal demonstrates the separation of magnetic and nonmagnetic contribution in the signal. The colormap (Fig. 6.2d) shows the Fourier spectra obtained at various H_{app}. A single magnetic resonance peak appears. The dashed line is the analytic solution of the Kittel mode assuming a Landé factor g = 2.21 and a saturation magnetization M_s = 341.2 emu/cm^3, obtained by the least square method. Using rather low M_s value as a fitting parameter accounts for uncertainties in the magnet size, shape, and the H_{app} value at the probed nanomagnet location in the experiments. Nevertheless, the analytic solution shows good agreement with the experimental results and these parameters are used in subsequent simulations.

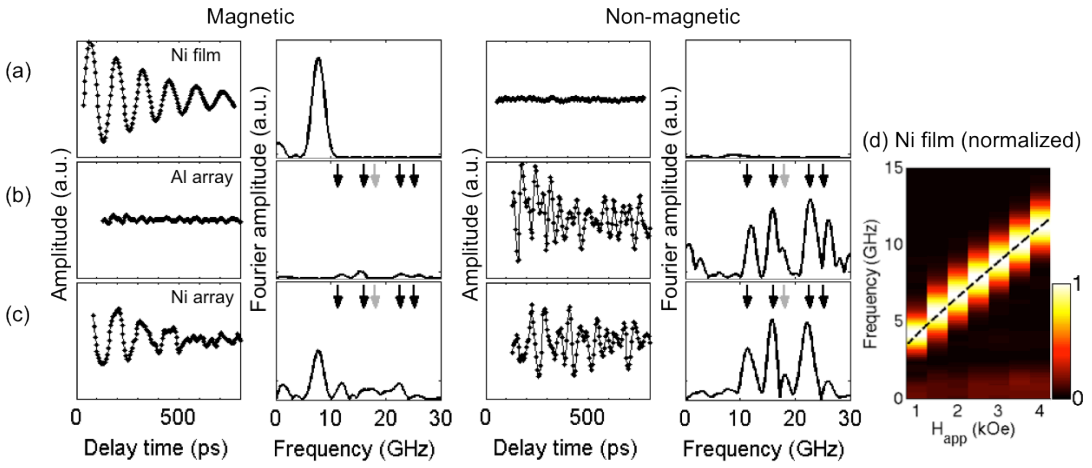

Fig. 6.2. (a–c) Typical TR-MOKE signal from three sample types after background subtraction, measured at the field of H_{app} = 2.5 kOe applied at θ_H = 30° from the surface normal. Black and light gray curves represent the magnetic difference signal and nonmagnetic sum signal, respectively. In the Fourier spectra (right column), the black and light gray arrows indicate the frequencies of the Rayleigh waves and surface skimming longitudinal wave. (d) The Fourier spectra obtained from the planar nickel film at various field H_{app}. The dashed curve represents the fit with the Kittel equation (2.2.29).

The patterned aluminum elliptic disks with p = 212 nm exhibit multiple oscillation modes in the nonmagnetic channel. Only a very small signal is observed in the magnetic channel due to imperfect balancing of the photodetectors. The nonmagnetic oscillations are attributed to the SAWs generated by the pump pulse heating the aluminum elements, as discussed in section 5.1.2. The four black arrows in Fig. 6.2b denote the lowest Rayleigh wave (RW) frequencies, predicted for the RW

velocity v = 2400 m/s with Eq. (5.1.2) and show good agreement with the experiment. Note that the SAW velocity is predominantly determined by the elastic properties of the hafnium oxide AR coating layer, where the majority of the elastic energy is confined. Due to the elliptic shape of the nanoelements, SAW modes along x and y directions are nondegenerate. However, the splitting is smaller than the linewidth of the Fourier peaks and cannot be seen here. As will be discussed later, the non-degeneracy was confirmed in the simulations (section 6.2.2) and also in more recent measurements with longer scans (section 6.4). In addition to the RWs, an additional peak at 17.6 GHz is observed (shown with a gray arrow in Fig. 6.2b). This mode is attributed to the surface skimming longitudinal wave (SSLW) as described in section 5.1.2.

Fig. 6.2c shows the response of the patterned nickel elliptic disks. Here, we observe oscillations in both the magnetic and nonmagnetic channels. The nonmagnetic signal resembles that of the nonmagnetic aluminum array (Fig. 6.2b) and is attributed to the SAWs. These SAW frequencies agree with those observed in the lighter aluminum array and validates the assumption of negligible mass loading [177,190,191, also discussed in section 5.1.2]. The magnetic signal, on the other hand, is attributed to the interplay between the Kittel mode shifted from the film response due to the demagnetization field inside the nanomagnets and the SAWs. The presence of the peaks at the SAW frequencies shows that the excited magnetic response is determined by the elastic characteristics of the substrate material and the geometric design of the nanomagnet array, apart from the magnetostatic effect.

We carried out a series of TR-MOKE scans at varying H_{app}. Fig. 6.3 displays the Fourier spectra of the sum and difference channels. As expected, the nonmagnetic frequencies (Fig. 6.3a) were independent of the field, while the magnetic signal shows an unexpected and complex response. Fig. 6.3b shows the normalized Fourier spectra, in which the highest Fourier amplitude is assigned a value of 1 for better visualization of the mode structure. In contrast to the single continuous peak of the film (Fig. 6.2d), a fragmented multimode response is seen at fields $H_{app} > 2.5$ kOe, while at lower fields, the spectra are dominated by a single Kittel mode, qualitatively resembling the film response. The low-field response was well reproduced with micromagnetic simulations including only the magnetic contributions (dashed line). At higher fields, however, we find an extended band at 12.2 GHz where the magnetic response is "pinned" over a wide range of more than 2.0 kOe. A similar pinning is observed at 15.8, 17.7, and 22.3 GHz as well. This demonstrates the generation of magnetic oscillations at frequencies far removed from the intrinsic magnetic response. In a non-normalized display of the same Fourier spectra (Fig. 6.3c), the crossover point of the Kittel mode and these bands exhibits the highest Fourier amplitude. This enhancement of the Fourier amplitude at the crossover is manifestation of prolonged oscillation mode in the time domain, driven by the energy pumped from the elastic system. These frequencies coincide with the nonmagnetic SAW frequencies and suggest strong coupling between the mechanical and magnetic modes at the crossover points. The solid and dashed arrows identify the RWs and SSLW, respectively, and will be discussed in the following.

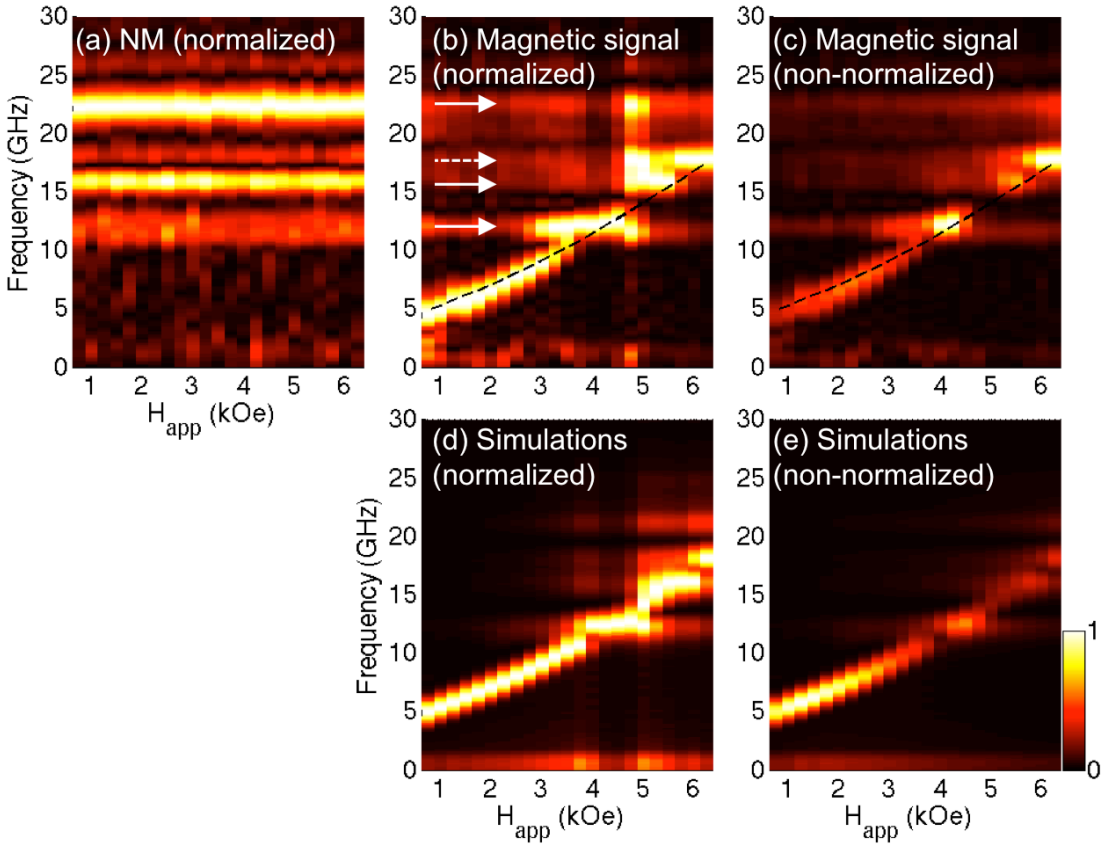

Fig. 6.3. Fourier spectra of the magnetization precession of nickel elliptic disks with p = 212 nm in TR-MOKE measurements and in simulations. In (b) and (d), the Fourier spectra have been normalized, assigning the value of one to the highest point in each spectrum. The solid and dashed arrows in (b) represents the frequencies of the Rayleigh waves and the surface skimming longitudinal wave.

To elucidate the experimental observations, the magnetoelastic simulation was run as described in section 5.4. With $B_1 = B_2 = 7.85$ MJ/m^3 [184] for polycrystalline nickel with a pump fluence of 0.78 J/cm^2, the calculated $\boldsymbol{H}_{\mathrm{MEL}}$ has an oscillation

amplitude of ~170 Oe at the center of the elliptic disk at 100 ps after the excitation, mainly along the major axis of the ellipse (see Fig. 5.10b–f). The simulated magnetization dynamics in the presence of $\boldsymbol{H}_{\mathrm{MEL}}$ was Fourier-transformed and the resulting spectra are shown in Fig. 6.3d and 6.3e. The simulated Fourier spectra are in excellent qualitative agreement with the measurements, reproducing the key features. Namely, the simulations correctly reproduced the mode pinning at 12.4, 16.0, 17.9 and 21.1 GHz over a wide range of applied fields and show an increased Fourier amplitude at the crossover points, as can be seen in the non-normalized plots (Fig. 6.3e). It also reproduces the mode at 17.9 GHz, which we attribute to the SSLW described in section 5.1.2. Later, we will confirm this assignment with space-time discrete Fourier transform analysis of the simulated displacement.

The tunability of the SAW frequency and thus the pinning region was demonstrated by using nickel elliptic disks with larger array pitch of p = 282 nm. TR-MOKE measurements and simulations were carried out in the same way as the previous sample and are shown in Fig. 6.4. Both RWs and SSLW shifted their frequency downward as predicted by Eq. (5.1.2) and were again correctly reproduced by the magnetoelastic simulations. Consequently, the enhancement of the Fourier amplitude and the pinning are observed at different SAW frequencies under different applied fields. The RWs and SSLW are identified as solid and dashed arrows in Fig. 6.4.

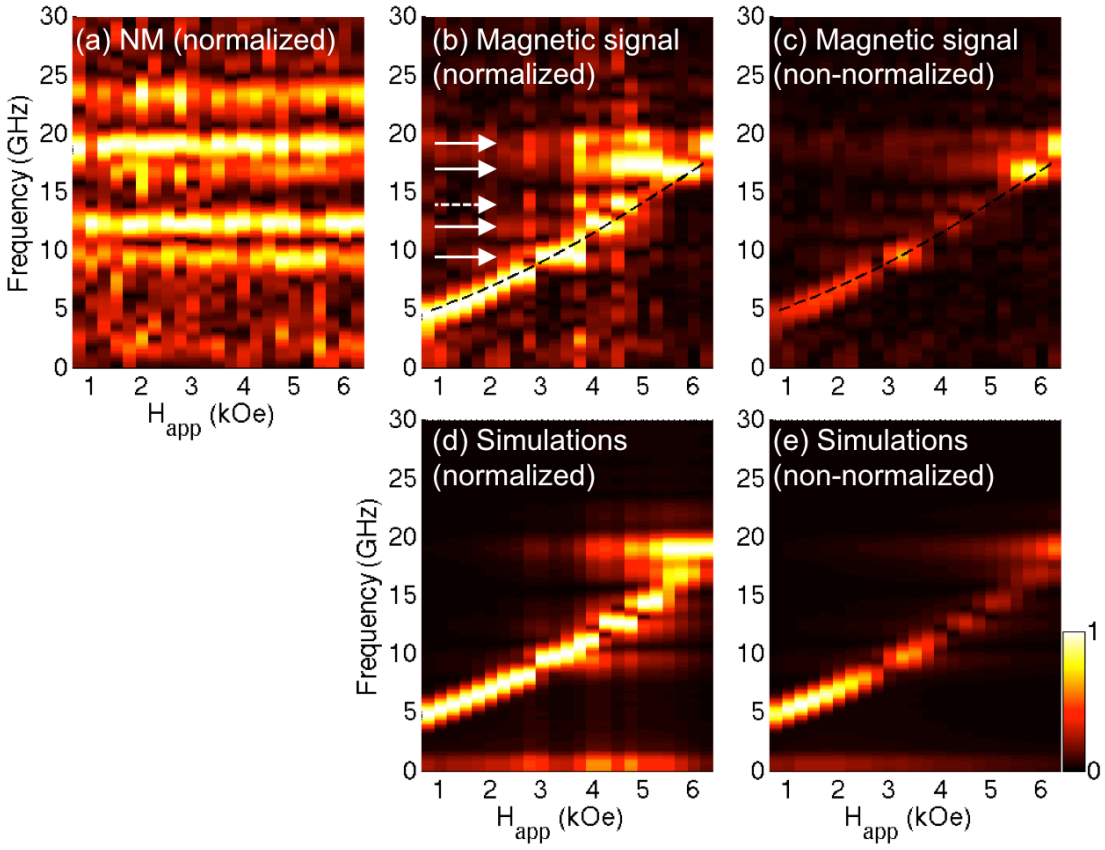

Fig. 6.4. Fourier spectra of the magnetization precession of nickel elliptic disks with p = 282 nm in TR-MOKE measurements and in simulations. In (b) and (d), the Fourier spectra have been normalized, assigning the value of one to the highest point in each spectrum. The solid and dashed arrows in (b) represents the frequencies of the Rayleigh waves and the surface skimming longitudinal wave.

6.2.2 Spatial waveforms of SAWs

In contrast to the strong dependence on the array pitch, we found no dependence of the magnetic spin wave spectra on optical pump power over a wide

range in experiments and simulations. This observation is consistent with the linear dependence of the induced strain on pump power.

To understand the nature of these modes, we have performed further analysis on the simulated displacement $\boldsymbol{u}$. First, spatiotemporal discrete Fourier transform (DFT) of the simulated $\boldsymbol{u}$ is carried out. Here, the coordinates are defined as in Fig. 6.1. $\boldsymbol{u}$ at the top of the AR coating is taken along x, y, and z direction through (0,0,0). Two-dimensional Fourier transform

$$F(k_x,k_y)=\frac{1}{N}\sum_{p=0}^{N-1}\sum_{q=0}^{N-1}f(x,y)\exp\left(-\frac{i2\pi(k_x x+k_y y)}{N}\right) \tag{6.2.1}$$

is applied to the displacement $\boldsymbol{u}(\boldsymbol{r},t)$ with zero padding and the Hamming window function applied in the time domain but not in the spatial domain.

Fig. 6.5 shows an example of this analysis on nickel elliptic disks with p = 212 nm. The wavenumbers k_i are normalized to $2\pi/p$ so k_i represents the order of the spatial mode in the x_i direction. Each SAW frequency is decomposed into spatial modes (hk) with $h = k_x$ and $k = k_y$ as depicted in Fig. 6.5a. For example, the three lowest visible peaks in the Fourier spectrum of the overall displacement evolution (Fig. 6.5b) are decomposed to the (10) and (01) modes, (11) mode, and (20) and (02) modes, respectively. The (10) mode shows further splitting due to the asymmetry of the sample structure in x and y direction. With a scan length of 1 ns used in the experiments and simulations, this cannot be resolved in the Fourier spectrum. It also reveals the spatial mode of (21) and (12) modes, which show non-degeneracy at 25

and 27 GHz. These peaks, however, can only seen as a broadened peak in the Fourier spectrum of the entire signal (Fig. 6.5b).

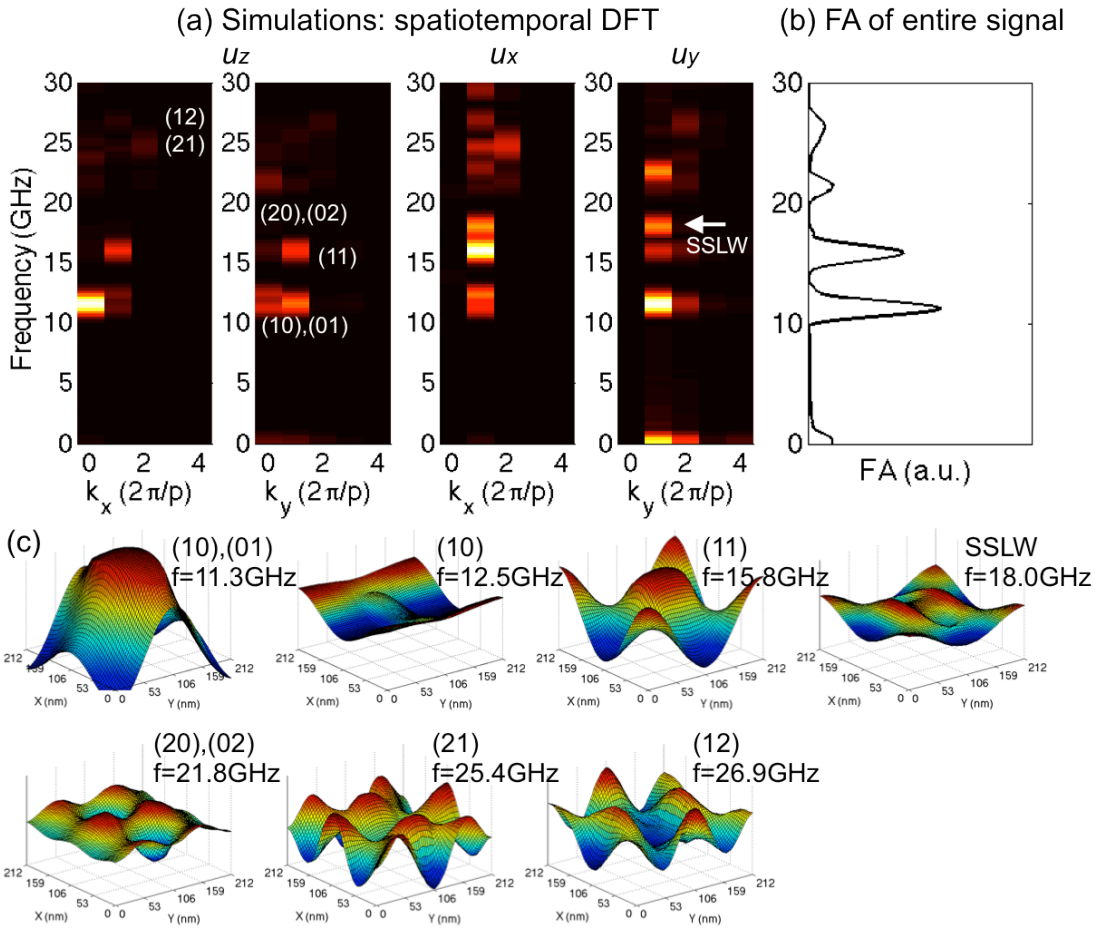

Fig. 6.5. (a) Space-time discrete Fourier transfomr of nickel elliptic disks with p = 212 nm. (b) Absolute Fourier amplitude of the overall displacement evolution u_z at the center of the elliptic disk. (c) Snapshots of each SAW mode obtained by applying the Butterworth filter in the time domain to the displacement $u_z(\boldsymbol{r},t)$.

The spatial waveform of each mode was obtained by applying the Butterworth digital filter to the displacement. The Butterworth filter with a passband centered at a given mode frequency was applied to the time evolution of u_z at each point. The snapshots of the filtered displacement evolution is displayed in Fig. 6.5c, representing each SAW mode. The lower branch of the (10) mode and the (01) mode are degenerate and are represented in the first plot in Fig. 6.5c. The upper branch of the (10) mode, on the other hand, shows the spatial mode with the largest amplitude in the substrate by the elliptic disk, propagating along its major axis.

The spatiotemporal Fourier spectra of u_z show a small peak at 18 GHz, not visible in Fig. 6.5b. This peak appears stronger in u_x and u_y along the x and y directions (Fig. 6.5a). These frequencies obey Eq. (5.1.1) and change linearly with $1/p$ but remain virtually unchanged in simulations with different AR coating thicknesses, magnet sizes, magnet densities, and shapes. Furthermore, this mode was observed even in the simulations without the magnets as seen in Fig. 6.6, where the Gaussian-shaped initial displacement is set for starting the elastic motion. Even though the simulated structure has no periodicity, the periodicity of the initial displacement launches SAWs and we observe various elastic modes, whose frequencies are determined by the speed of the RWs and the SSLW in the structure. As in the elliptic disks in Fig. 6.5, multiple RWs and SSLW peaks are decomposed into spatial modes with various wavenumbers. Unlike Fig. 6.5, the x and y directions were degenerate. These observations rule out the possibility that the 18 GHz mode is localized in the structure and indicate that this oscillation mode is the SSLW that is

dominated by the longitudinal component of displacement and confined to the vicinity of the surface like RWs but having 1.5–2 times as large a velocity as the RWs.

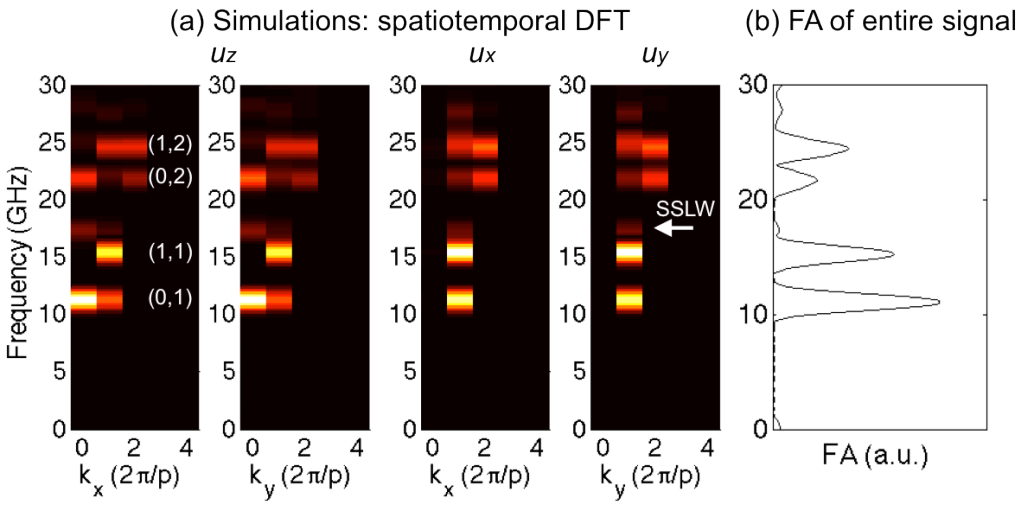

Fig. 6.6. (a) Space-time discrete Fourier transfomr of the hafnium oxide AR coating in the absense of nanomagnets. The initial displacement was given as a Gaussian profile with 30 μm FWHM. (b) Absolute Fourier spectrum of the overall displacement evolution at the center of the structure.

Finally, the nature of the 18.0 GHz mode is further analyzed by intentionally exciting longitudinal waves along the minor axis of the elliptic disk. Here, the initial displacement is set to be $u_{x0} = 0$, $u_{y0} = \sin(2\pi y/p)\exp(-z/z_0)$ with z_0 = 200 nm. As shown in Fig. 6.7, the 18.0 GHz mode is selectively excited. The filtered spatial

mode (Fig. 6.7b) clearly shows that the mode has large longitudinal component (u_y) along the propagation direction.

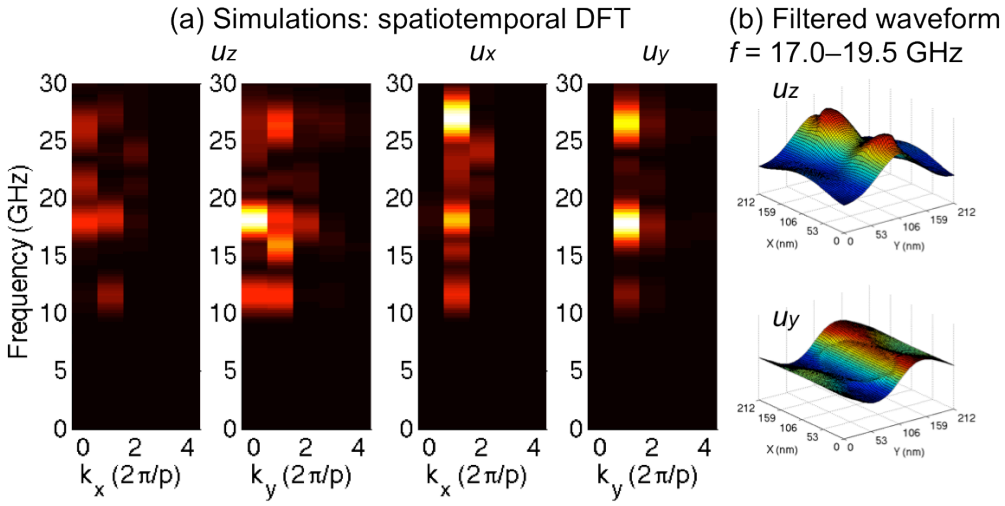

Fig. 6.7. (a) Space-time discrete Fourier transfomr of nickel elliptic disks with p = 212 nm with sinusoidal wave-like initial excitation. (b) Snapshots of each SAW mode obtained by applying the Butterworth filter in the time domain to the displacement $\boldsymbol{u}(\boldsymbol{r},t)$.

6.3 Nonlocal excitation of magnetization precession with propagating SAWs

As discussed in the previous sections, the $1/p$ dependence of the frequencies, multiple frequency components corresponding to different wavenumbers, and the presence of the SSLW mode observed both in experiments and simulations, indicate the excitation of propagating SAWs and not localized mechanical vibrations. Here,

we confirm this claim with a direct observation of the propagating nature of the excitation scheme by probing a region spatially separated from the pump spot.

The sample is fabricated like the nickel nanomagnets in the previous sections but the pattern consists of nickel squares and bars as shown in Fig. 6.8. The pump pulses were focused on the bars of 100 nm width and 200 nm pitch. Approximately 2 μm apart from the bars, two arrays of the 100 nm nickel squares were prepared with pitch p = 150 and 200 nm. The thermally expanding nickel bars act as the transducer of the elastic strain. They are expected to generate the SAW at a frequency determined by their pitch p, following the SSLW pulse with broad spectrum, which propagates faster. The SAWs travel perpendicular to the bars and enter the array. By adjusting the last mirror for the pump beam before it is combined with the probe beam, the probe beam is shifted from the position of the pump onto the array, as depicted in Fig. 6.8. Since the pump and probe beams are not overlapped, the thermal excitation of the magnetization precession will not be probed. Instead, the traveling SAWs eventually reach the probed region and, if they have sufficient amplitude, excite the magnetization precession in the nickel squares via the magnetoelastic effect. The pump and probe beams are focused to spot sizes of 1.6 and 3.0 μm $1/e^2$ diameter, respectively, a few time smaller than in the previous sections. This is to ensure the clear separation of the pump and probe spots with a reasonably small center-to-center distance between them, which determines the delay of excitation. The distance is limited by the dissipation of the excitation power; as the probe spot is

further separated from the pump spot, the SAWs power density dissipates and only a small fraction of the pumped energy reaches the probed region.

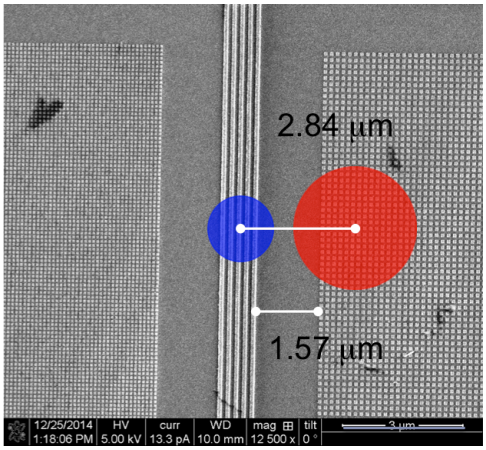

Fig. 6.8. Scanning electron micrograph of nickel bars (100 nm wide on 200 nm pitch) and arrays (100 nm squares on 150 nm pitch). The blue and red circles represent the approximate position and size of the pump and probe spots. The distance between the ends of the bars and the array is 1.57 μm. A Rayleigh wave with velocity v = 2400 m/s travels this distance in 655 ps.

On the nickel array with p = 150 nm pitch, TR-MOKE measurements were carried out. Representative traces and corresponding Fourier spectra are shown in Fig. 6.9 for H_{app} = 2.0 and 5.5 kOe, applied at θ_H = 30° from the surface normal. Both difference and sum signals show delayed excitation starting at ~500 ps. The finite size of the pump and probe spots and the broad pulse width of the traveling SAW cause a slow rising of the precession and excitation of the SAWs in the array. The Fourier spectra of the time section t = 900–1900 ps are shown in Fig. 6.9. They show

qualitatively similar features as in the previous sections—a field-dependent magnetic mode and its pinning and enhancement at crossover points with the SAW frequencies of the array. In addition, the spectra show a strong low frequency component due to the large excitation pulse for 500–1000 ps. In Fig. 6.9c and 6.9d, the pinning frequency is 16 GHz, determined by the pitch of the array p = 150 nm and not of the bars. Pinning with smaller Fourier amplitude is observed at 12 GHz too, corresponding to the first order SAW of the 200 nm pitch bars, but only with the absolute Fourier amplitude of about 1/3 of the 16 GHz peak.

In Fig. 6.10, representative sectioned time traces and corresponding absolute Fourier amplitude spectra are shown for the magnetic signal. By sliding the analyzing time window, the time evolution of the frequency peaks was obtained. Magnetic signals measured at H_{app} = 2.0 and 5.5 kOe show increase in the Fourier amplitude peaking around 500–1500 ps and decaying subsequently. This reflects the delayed excitation with an elastic pulse. As seen in Fig. 6.9c, the Kittel mode is expected at ~ 5 GHz for H_{app} = 2.0 kOe but it appears very weak in the sectioned Fourier spectra (Fig. 6.10a). At H_{app} = 5.5 kOe, in contrast, strong frequency peaks at 16 GHz and at higher frequencies were observed, reflecting the SAW frequencies determined by the array pitch p = 150 nm Fig. 6.10b). The delayed excitation of the magnetization precession is clearly seen in Fig. 6.10c. The absolute Fourier amplitude of the signal in each time section is obtained as a function of the analyzed time. Comparing to the standard TR-MOKE measurements with overlapped beams (solid lines), the signal with propagating SAWs (dashed lines) progressively increases its amplitude for the

time section t = 600–1100 ps, as the SAWs reach the probe region. It then reduces its magnitude over time. We also investigated another array with the identical element size and the array pitch p = 200 nm, matching that of the bars, obtaining qualitatively similar observations. Overall, the TR-MOKE signals with shifted pump and probe beams prove that the SAWs propagate in lateral directions and can be sufficiently strong to excite the magnetization precession.

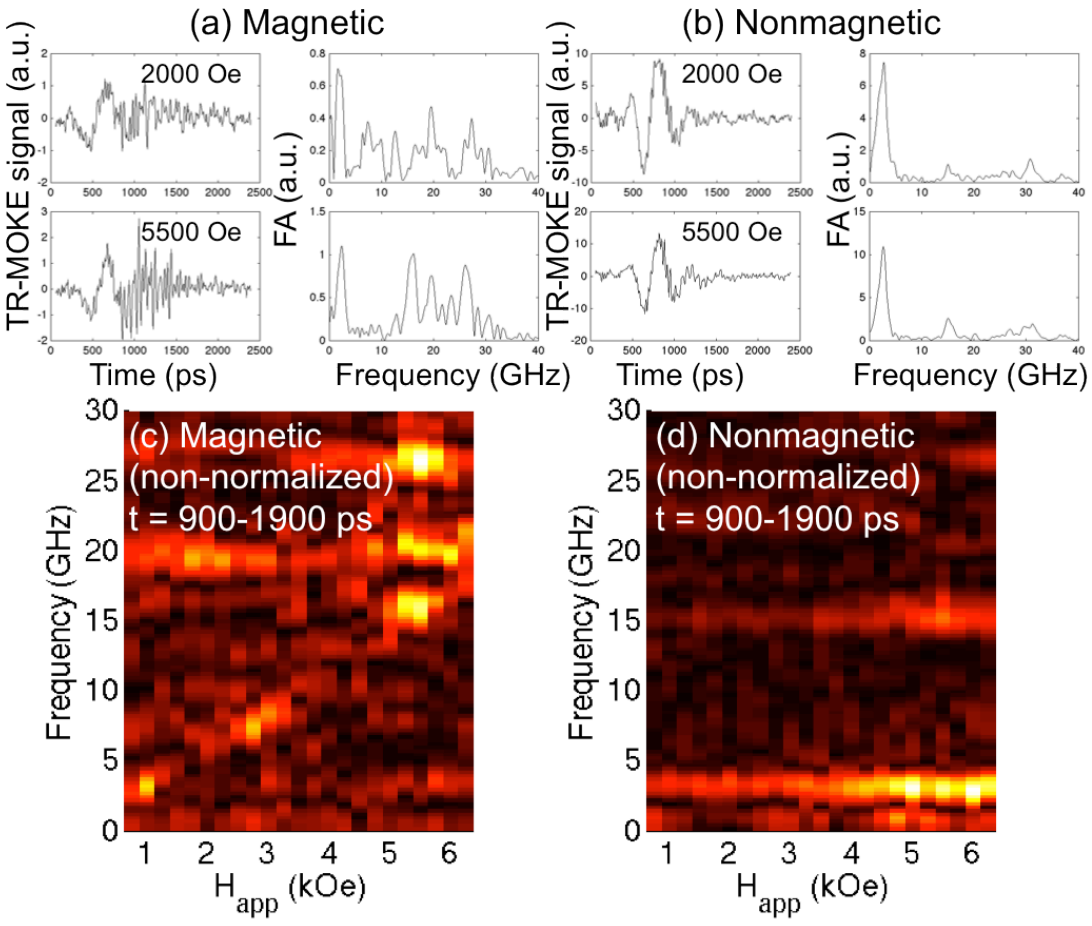

Fig. 6.9. (a, b) Time traces and Fourier spectra of the entire TR-MOKE signal with shifted pump and probe spots. The pump laser was focused on 100 nm bars with 200

nm pitch and the dynamics of 100 nm squares on 150 nm pitch was probed. The magnetic (a) and nonmagnetic (b) signals show delayed excitation. An excitation pulse with low frequency arrives at the probe region at around 500 ps and excites the precession and the surface acoustic waves in the array. (c, d) Absolute Fourier amplitude spectra of the magnetic (c) and nonmagnetic (d) signals. Time sections of t = 900–1900 ps are analyzed.

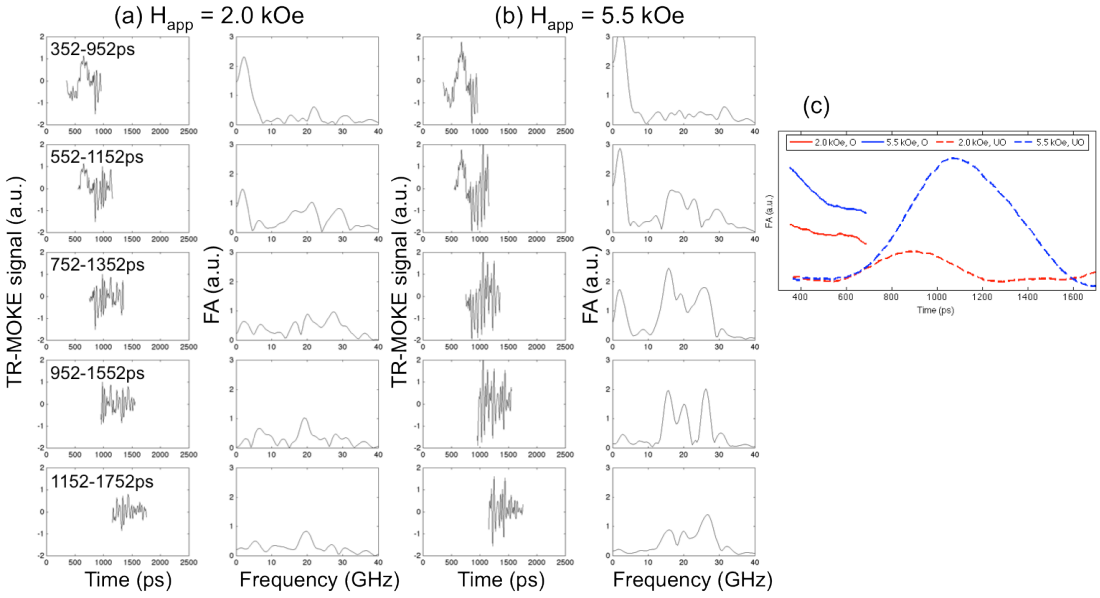

Fig. 6.10. (a, b) Sectioned time traces and the corresponding Fourier spectra of the magnetic signal, measured with shifted pump and probe spots. The pump laser was focused on 100 nm bars with 200 nm pitch and the dynamics of 100 nm squares on 150 nm pitch was probed. (c) Absolute Fourier amplitude (FA) traced at the fundamental SAW frequency at 16 GHz obtained by sliding the analyzed time section. The horizontal axis shows the center of analyzed time windows (600 ps

long). Solid lines represent the time evolution of the FA measured with overlapping (O) pump and probe beams (not shown). The dashed lines represent measurements with unoverlapped (UO) beams, whose subset is shown in (a, b). The overlapped data (O, solide lines) has been scaled for better visualization.

6.4 Demonstration in other shapes and longer scans

This section supplements the experimental results reported in section 6.2. First, the nickel elliptic disks with an array pitch p = 212 nm were measured again with a longer delay stage. A newer setup enabled TR-MOKE scans with up to 4 ns delay between the pump and probe. Fig. 6.11 presents the Fourier spectra of the same sample measured for a delay time up to 2.5 ns.

As discussed in section 6.2, the Fourier spectra show a clear magnetic mode with the frequency increasing with the applied field H_{app}. It crosses and is pinned at the SAW frequencies, with enhanced Fourier amplitude at the crossover. Due to the longer scan length, the frequency resolution of the Fourier spectra is better than the spectra shown in Fig. 6.3. Most remarkably, the crossover of the magnetic mode with the fundamental SAW around 11 GHz is now split into two closely located modes due to the asymmetry of the elliptic disks in x and y directions, as predicted in the simulations and shown as the (10) modes in Fig. 6.5. This demonstrates the reproducibility of SAW generation with a pulsed laser and the reliability of the magnetoelastic simulation procedure described in section 5.4.

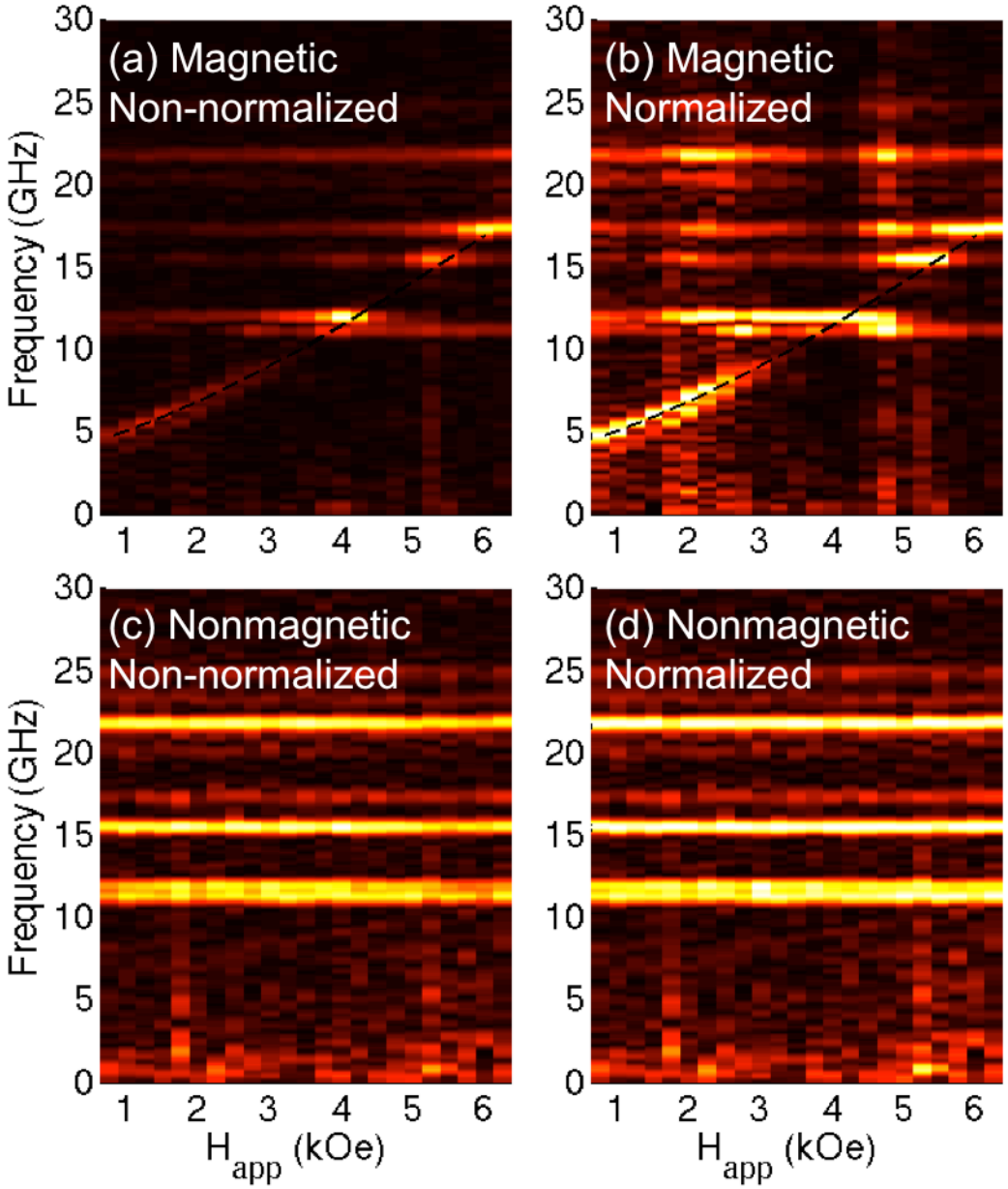

Fig. 6.11 Fourier spectra of 2.5 ns scans on nickel elliptic disks, p = 212 nm.

Another nickel nanomagnet array with different shape was also measured. 125 nm nickel squares with the pitch p = 250 nm (Fig. 6.1c) were characterized using the same experimental procedure and the resulted Fourier spectra are shown in Fig. 6.12.

Unlike the elliptic disks (Fig. 6.11), the array of square nanomagnets showed only one fundamental SAW mode at 10.1 GHz. The magnetic response exhibits both center and edge modes and makes two crossovers with a SAW mode. This is most clearly seen at 10 GHz at 3 and 3.75 kOe in Fig. 6.12a, as indicated by two upward arrows.

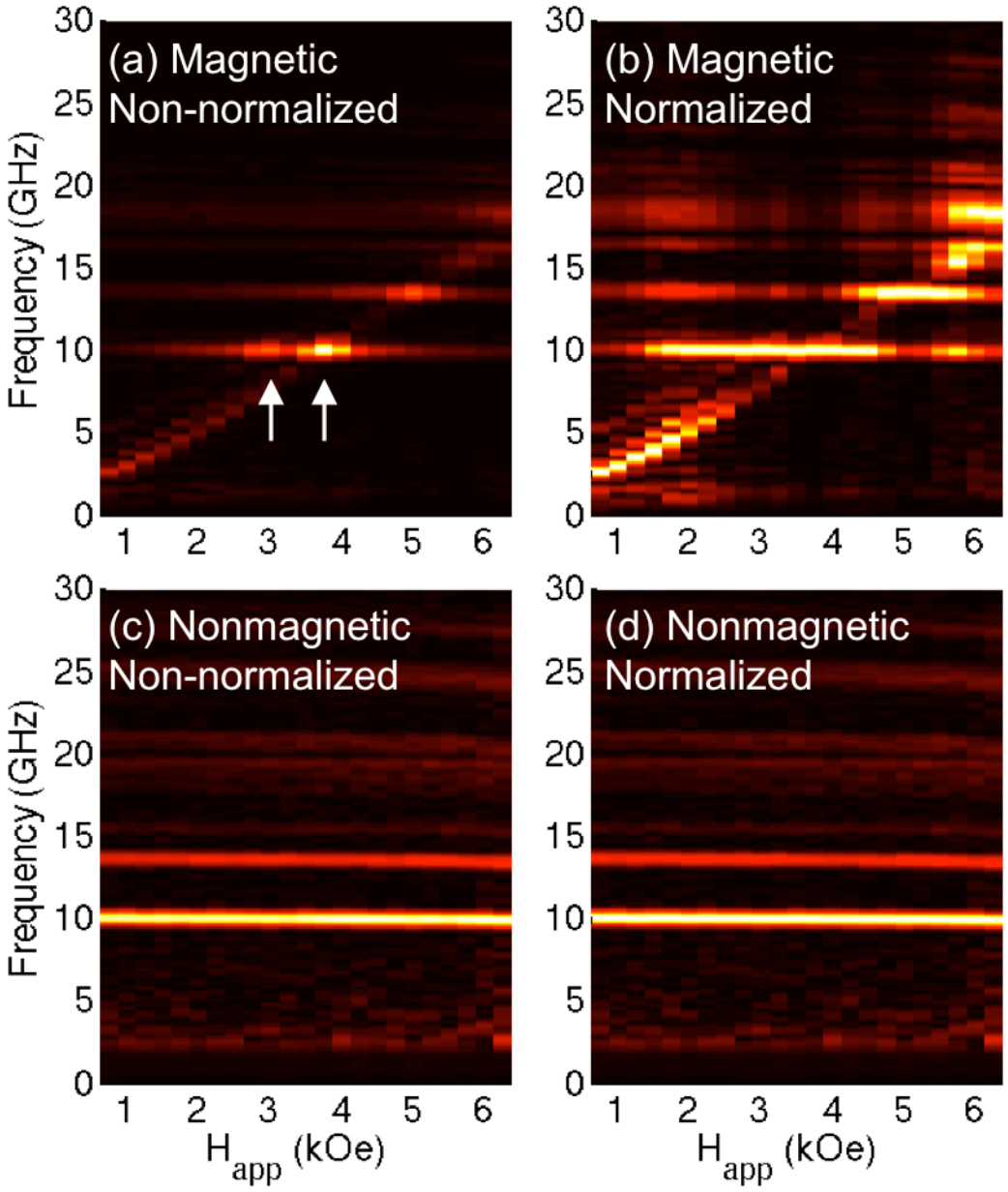

Fig. 6.12 Fourier spectra of 2.5 ns scans on 125 nm nickel squares, p = 250 nm. In (a), the arrows indicate the position of crossover of the center and edge modes with the fundamental SAW mode.

6.5 Summary

We have investigated the magnetoelastic response of densely packed nickel nanomagnet arrays strongly coupled to propagating SAWs via the magnetoelastic effect. Both mechanical and magnetic oscillation modes are excited by an optical pump pulse and are found to be strongly coupled to one another. When the intrinsic oscillation frequencies of the two modes are brought near degeneracy by adjusting the applied field, the magnetization precession is pinned at the SAW frequencies and exhibits an enhancement in the Fourier amplitude, reflecting prolonged oscillation modes in the time domain, driven by the effective magnetoelastic field. Even when the magnetostatic interelement interaction is negligible, the array geometry can crucially determine the magnetic response via the elastic mode, primarily determined by the array pitch and the elastic properties of the substrate material. The finite element analysis of the elastic motion and micromagnetic simulations taking the magnetoelastic coupling into account are in excellent agreement with the experimental observations, reproducing the correct frequencies of the RWs and SSLW, the pinning of the magnetic modes the SAW frequencies, and the Fourier amplitude enhancement at the crossover fields.

7. Pinning width of the magnetoelastically driven magnetization precession

In this chapter, we will discuss the range of the applied field where the magnetization precession is pinned by the magnetoelastic coupling with surface acoustic waves. By characterizing various materials with different magnetic and magnetoelastic parameters, we have characterized this pinning width as a function of these parameters. We found that it depends on the damping parameter. This ensures a new and accurate method to quantify the phenomenological damping parameter of patterned nanomagnets where fitting of time traces is restricted by the presence of multiple magnetoelastic modes. Moreover, this technique provides exciting possibilities for determining damping which is notoriously difficult in nanopatterned magnetic structures. We demonstrate this damping characterization in nickel, cobalt, and TbFe nanomagnet arrays and verify its validity by comparison to fitting of time traces and by micromagnetic simulations.

7.1 Introduction

The damping characteristics of nanostructured magnets determine critical operational characteristics of spintronic devices and its experimental characterization is of great practical interest for their development. To list a few examples, in spin transfer torque magnetic random access memories (STT-MRAMs), the damping parameter is directly proportional to the threshold switching current density and limits the energy consumption of the device [15,211]. It also plays an important role in

heat-assisted magnetic recording, determining the critical device characteristics such as the switching time [23] and transition jitters [212].

Along with the ferromagnetic resonance (FMR), commonly used for damping characterization, the time-resolved magneto-optic Kerr effect (TR-MOKE) has successfully been demonstrated to estimate the damping parameters in several ferromagnetic films [91,104,133,162–164,213,214] and isolated individual nanomagnets [71]. By fitting TR-MOKE time traces with a damped harmonic oscillation as discussed in section 3.4, an effective damping parameter is obtained. In contrast to the FMR measurements, the time-domain optical technique probes a smaller region of samples with high spatial resolution [161,165]. However, the analysis is complicated by the presence of extrinsic damping mechanisms, dominating the energy dissipation at low applied field. An accurate estimate of the intrinsic Gilbert damping can only be achieved at large fields [71,104,162–164]. In patterned nanomagnet arrays, as seen in Chapter 6, the presence of multiple SAW-driven magnetoelastic modes further complicates the time-domain damping analysis, making it very challenging, if not impossible.

In this Chapter, we present a novel empirical method to measure the Gilbert damping in patterned nanomagnet arrays, utilizing the strong magnetoelastic interaction demonstrated in Chapter 6. The pinning width ΔH_P in various materials of large magnetoelastic coefficients B_i (i = 1 and 2 denoting coefficients for normal and shear strain, as defined in Eq. (5.3.1)) were investigated, in order to quantify the effect of the magnetoelastic coefficients over the magnetization dynamics. However,

as will be discussed in the following sections, it was found that the pinning width ΔH_P depends only on the damping parameter α, but not on B_i. Conversely, this provides a convenient method to characterize the damping from complicated magnetoelastic dynamics of nanomagnets.

Specifically, nanomagnet arrays of cobalt and TbFe alloy were prepared in addition to the nickel samples. Table 7.1 summarizes the characteristics of the parameters. They were chosen for their large magnetoelastic coefficients B_i about three times as large as that of nickel (B_i = 7.85 [184], 25.6 [215], and -22.5 [216] MJ/m^3 for nickel, cobalt, and TbFe, respectively). Like the nickel nanomagnets characterized in Chapter 6, 30-nm-thick nickel and cobalt squares, with an average element size of 125 and 160 nm, respectively, were fabricated with the electron-beam lithography, electron-beam evaporation and liftoff process on an AR coated silicon wafer. Although identical pitches were used, the actual size of the nanoelements turned out slightly different for different materials as shown in Fig. 7.1. An 18.7-nm-thick $Tb_{0.25}Fe_{0.75}$ film with 5 nm Pt capping layer was deposited on a 100 nm SiO_2 layer and was milled into an array of 150 nm dots using a focused ion beam. Despite the milling pattern with square elements, the actual sample turned out to have rounder corners as shown in Fig. 7.1c. As will be discussed below, the magnetization dynamics in these nanomagnets was dominated by the Kittle (center) mode and the difference in the shape of individual nanomagnets made a negligible effect.

	magnetoelastic coefficients B_i	damping α
Nickel	low	low

Cobalt	high	low
TbFe	high	low

Table 7.1. Qualitative summary of the magnetoelastic coefficients B_i and the damping parameter α of the sample materials.

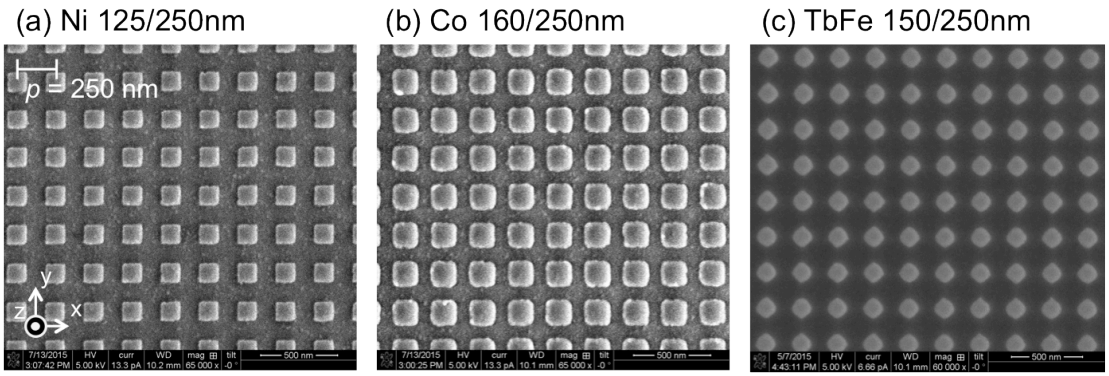

Fig. 7.1. Scanning electron micrographs of nickel (a), cobalt (b), and TbFe (c) arrays. Nickel and cobalt arrays were fabricated with electron beam lithography and liftoff process. The TbFe dots were milled using a focused ion beam.

7.2 Theory of magnetization precession magnetoelastically driven by SAWs

As discussed in section 5.4, the magnetoelastic contribution in TR-MOKE measurements on nanomagnet arrays works as a driving effective field $\boldsymbol{H}_{\mathrm{MEL}}$ oscillating at the SAW frequencies determined by the array geometry and the elastic properties of the materials. As explained in Chapter 6, the backaction of the

magnetization dynamics on the elastic system is negligible in this measurement setup and a simple model with additional effective field terms suffices to interpret TR-MOKE spectra. The SAWs have a slower damping rate than the decay rate of the magnetization precession for the materials discussed in this chapter. Therefore, the magnetoelastic field can be treated as a pseudo-steady AC field. We assume the slowly varying envelope approximation and the linearity of the system. Under these assumptions, the magnetoelastic field is modeled as an AC driving field with steady magnitude in the time scale on the problem and the multiple frequency components of the SAWs can be treated separately. We obtain the linewidth of the magnetoelastically coupled mode driven by a SAW by deriving the magnetic susceptibility χ [108 pp. 17-22]. Despite the exotic mechanical nature of the excitation field, the mathematical discussion below is commonly encountered in characterization of the FMR linewidth. First, we linearize the Landau-Lifshitz-Gilbert equation without allowance of the damping term and derive the frequency dependence of the χ for the small amplitude limit. Then, we will introduce the damping in the form of the LLG equation (2.2.2) and modify the frequency dependence of χ.

The magnetization $\boldsymbol{M}$ and the effective field $\boldsymbol{H}_{\text{eff}}$ (2.2.6) are decomposed into the steady equilibrium part and the alternating part as

$$\boldsymbol{M} = \boldsymbol{M}_0 + \Delta\boldsymbol{M}(t)$$

$$\boldsymbol{H} = \boldsymbol{H}_{\text{eff},0} + \Delta\boldsymbol{H}(t)\,, \tag{7.2.1}$$

Furthermore, we assume sinusoidal time-dependence of $\boldsymbol{M}_{\mathrm{AC}}$ and $\boldsymbol{H}_{\mathrm{eff,AC}}$ with complex amplitudes $\boldsymbol{M}_{\mathbf{AC}}$ and $\boldsymbol{H}_{\mathrm{eff,AC}}$ as

$$\tilde{\boldsymbol{M}}_{\mathrm{AC}} = \boldsymbol{M}_{\mathrm{AC}} \exp(i\omega t)$$

$$\tilde{\boldsymbol{H}}_{\mathrm{eff,AC}} = \boldsymbol{H}_{\mathrm{eff,AC}} \exp(i\omega t) \tag{7.2.2}$$

whose real parts are $\Delta\boldsymbol{M}(t)$ and $\Delta\boldsymbol{H}(t)$. Assuming $H_{\mathrm{eff,AC}} << H_{\mathrm{eff},0}$ and $M_{\mathrm{AC}} << M_0$, the LLG equation (2.2.2) without the damping term

$$\frac{\partial \boldsymbol{M}}{\partial t} = -\gamma \boldsymbol{M} \times \boldsymbol{H}_{\mathrm{eff}} \tag{7.2.3}$$

is linearized as

$$\frac{\partial \boldsymbol{M}_{\mathrm{AC}}}{\partial t} + \gamma \boldsymbol{M}_{\mathrm{AC}} \times \boldsymbol{H}_{\mathrm{eff},0} = -\gamma \boldsymbol{M}_0 \times \boldsymbol{H}_{\mathrm{eff,AC}} \tag{7.2.4}$$

by neglecting the products of the alternating parts. We have also used the relation $\boldsymbol{M}_0 \times \boldsymbol{H}_{\mathrm{eff},0} = 0$ at the equilibrium. With the complex amplitudes (7.2.2), Eq. (7.2.4) becomes

$$i\omega \boldsymbol{M}_{\mathrm{AC}} + \gamma \boldsymbol{M}_{\mathrm{AC}} \times \boldsymbol{H}_{\mathrm{eff},0} = -\gamma \boldsymbol{M}_0 \times \boldsymbol{H}_{\mathrm{eff,AC}} . \tag{7.2.5}$$

As (7.2.5) shows, only the components of $\boldsymbol{H}_{\mathrm{eff,AC}}$ perpendicular to the directions of $\boldsymbol{M}_0$ and $\boldsymbol{H}_{\mathrm{eff},0}$ drive the magnetization. Here, we define the z axis as the direction of $\boldsymbol{M}_0$ and $\boldsymbol{H}_{\mathrm{eff},0}$ and (7.2.5) can be projected on to the Cartesian axes. The solution of the system is

$$M_{\mathrm{AC},x} = \chi H_{\mathrm{eff,AC},x} + i\chi_a H_{\mathrm{eff,AC},y}$$

$$M_{\mathrm{AC},y} = -i\chi_a H_{\mathrm{eff,AC},x} + \chi H_{\mathrm{eff,AC},y}$$

$$M_{\mathrm{AC},z} = 0 , \tag{7.2.6}$$

or in tensor form $\boldsymbol{M}_{\mathrm{AC}} = \vec{\vec{\chi}}\boldsymbol{H}_{\mathrm{eff,AC}}$ with

$$\vec{\vec{\chi}} = \begin{bmatrix} \chi & i\chi_a & 0 \\ -i\chi_a & \chi & 0 \\ 0 & 0 & 0 \end{bmatrix}, \tag{7.2.7}$$

where

$$\chi = \frac{\gamma^2 M_S H_{\mathrm{eff},0}^2}{\gamma^2 H_{\mathrm{eff},0}^2 - \omega^2}$$

$$\chi_a = \frac{\gamma M_S \omega}{\gamma^2 H_{\mathrm{eff},0}^2 - \omega^2} \tag{7.2.8}$$

and $\omega_{\mathrm{H}} = \gamma H_{\mathrm{eff},0}$.

With the damping in the Gilbert form (2.2.2), the Landau-Lifshitz-Gilbert equation can be linearized as

$$i\omega\boldsymbol{M}_{\mathrm{AC}} + \gamma\boldsymbol{M}_{\mathrm{AC}} \times \boldsymbol{H}_{\mathrm{eff},0} + \frac{i\alpha\omega}{M_{\mathrm{S}}}\boldsymbol{M}_{\mathrm{AC}} \times \boldsymbol{M}_0 = \gamma\boldsymbol{M}_0 \times \boldsymbol{H}_{\mathrm{eff,AC}}. \tag{7.2.9}$$

(7.2.9) can be obtained by replacing $\omega_{\mathrm{H}} = \gamma H_{\mathrm{eff},0}$ in (7.2.5) with $\gamma H_{\mathrm{eff},0} + i\alpha\omega$. Therefore, the solution of (7.2.9) is obtained by the same replacement. The magnetic susceptibility now becomes complex ($\chi = \chi' + i\chi''$ and $\chi_a = \chi_a' + i\chi_a''$) as

$$\chi' = \frac{\gamma M_{\mathrm{S}}\omega_{\mathrm{H}}[\omega_{\mathrm{H}}^2 - (1-\alpha^2)\omega^2]}{[\omega_{\mathrm{H}}^2 - (1+\alpha^2)\omega^2]^2 + 4\alpha^2\omega^2\omega_{\mathrm{H}}^2}$$

$$\chi'' = \frac{\alpha\gamma M_{\mathrm{S}}\omega[\omega_{\mathrm{H}}^2 + (1+\alpha^2)\omega^2]}{[\omega_{\mathrm{H}}^2 - (1+\alpha^2)\omega^2]^2 + 4\alpha^2\omega^2\omega_{\mathrm{H}}^2}$$

$$\chi_a' = \frac{\gamma M_{\mathrm{S}}\omega[\omega_{\mathrm{H}}^2 - (1+\alpha^2)\omega^2]}{[\omega_{\mathrm{H}}^2 - (1+\alpha^2)\omega^2]^2 + 4\alpha^2\omega^2\omega_{\mathrm{H}}^2}$$

$$\chi_a'' = 2\alpha\gamma M_{\mathrm{S}}\omega^2\omega_{\mathrm{H}}. \tag{7.2.10}$$

The resonance condition is given by

$$\omega = \frac{\omega_{\mathrm{H}}}{1+\alpha^2} \tag{7.2.11}$$

and gives

$$\chi''_{\mathrm{res}} = \frac{\gamma M_0}{2\alpha\omega}$$

$$\chi''_{a,\mathrm{res}} = \frac{\gamma M_0}{2\alpha\omega_{\mathrm{H}}} \approx \chi''_{\mathrm{res}}\,. \tag{7.2.12}$$

Around the resonance, the magnetic susceptibility (7.2.10) is approximated as

$$\frac{\chi'}{\chi''_{\mathrm{res}}} \approx \frac{\chi'_a}{\chi''_{\mathrm{res}}} \approx \frac{\beta}{1+\beta^2}$$

$$\frac{\chi''}{\chi''_{\mathrm{res}}} \approx \frac{\chi''_a}{\chi''_{\mathrm{res}}} \approx \frac{1}{1+\beta^2}\,, \tag{7.2.13}$$

where $\beta = (H_{\mathrm{eff},0} - \omega/\gamma)/(\alpha\omega)$ for a constant $\omega = 2\pi f_{\mathrm{SAW}}$. (7.2.13) represents a Lorentzian resonance curve. At a sufficiently large external field $\boldsymbol{H}_{\mathrm{app}}$ where the change in $\boldsymbol{H}_{\mathrm{eff},0}$ is equal to that of $\boldsymbol{H}_{\mathrm{app}}$, Eq. (7.2.13) predicts a Lorentz resonance curve of the SAW-driven magnetoelastic mode with the *pinning width*

$$\Delta H_{\mathrm{P}} = \frac{4\pi\alpha f_{\mathrm{SAW}}}{\gamma}\,, \tag{7.2.14}$$

defined as the full width half maximum (FWHM) of the imaginary part χ''. Therefore, when the magnetization is driven by a pseudo-steady SAW and when we can neglect its spatially nonuniform distribution, the pinning linewidth ΔH_{P} depends only on the damping parameter α and not on the magnitude of $\boldsymbol{H}_{\mathrm{MEL}}$. Thus, ΔH_{P} does

not depend on the magnetoelastic coefficients B_i. Conversely, Eq. (7.2.14) can be used to obtain the damping parameter as

$$\alpha = \frac{\gamma \Delta H_{\mathrm{P}}}{4\pi f_{\mathrm{SAW}}}. \tag{7.2.15}$$

The subsequent sections demonstrate the validity of (7.2.15) and establish it as the basis for experimentally characterizing α in nanopatterned samples, avoiding the difficulties associated with a conventional time-domain method.

7.3 TR-MOKE results

7.3.1 Fourier spectra of TbFe, nickel, and cobalt arrays

Fig. 7.2 shows representative TR-MOKE signals obtained from the TbFe array, measured at the field orientation of $\theta_{\mathrm{H}} = 60°$ from the surface normal. The top row presents the time traces after background correction and the corresponding Fourier amplitude spectra measured at the applied field of $H_{\mathrm{app}} = 2.25$ kOe. Similar to the TR-MOKE results in Chapter 6, the sum channel shows prolonged oscillations, mainly corresponding to the nonmagnetic SAW peak at $f_{\mathrm{SAW}} = 17.8$ GHz. This frequency is determined by the velocity of the SAWs in the substrate layer (100 nm SiO_2). The time trace of the magnetic (difference) signal shows a heavily damped oscillation with a field-dependent frequency in the first ~250 ps, corresponding to the Kittel mode at 9.1 GHz. We note that the intrinsic Kittel mode could not be observed in the unpatterned TbFe film, suggesting that this magnetic mode in the nanomagnet array is magnetoelastically excited by the thermal expansion of the nanomagnets,

rather than the effective field pulse associated with the spin temperature. After it decays, the SAW-coupled magnetoelastic mode dominates the magnetization response, resulting in the peak at 17.8 GHz in the Fourier spectrum. The Fourier amplitude (FA) spectra with varying field H_{app} are summarized in the bottom row. Again, as discussed in Chapter 6, the sum signal spectra are independent of the applied field and the difference signal shows the magnetic response strongly altered by the SAWs. When the intrinsic Kittel mode seen at the low field range crosses the 17.8 GHz SAW frequency, a wide pinning of the precession and strong enhancement of the Fourier amplitude is observed. The light silicon oxide layer is affected more by mass loading of the nanomagnets and results in some low amplitude SAW modes below 15 GHz.

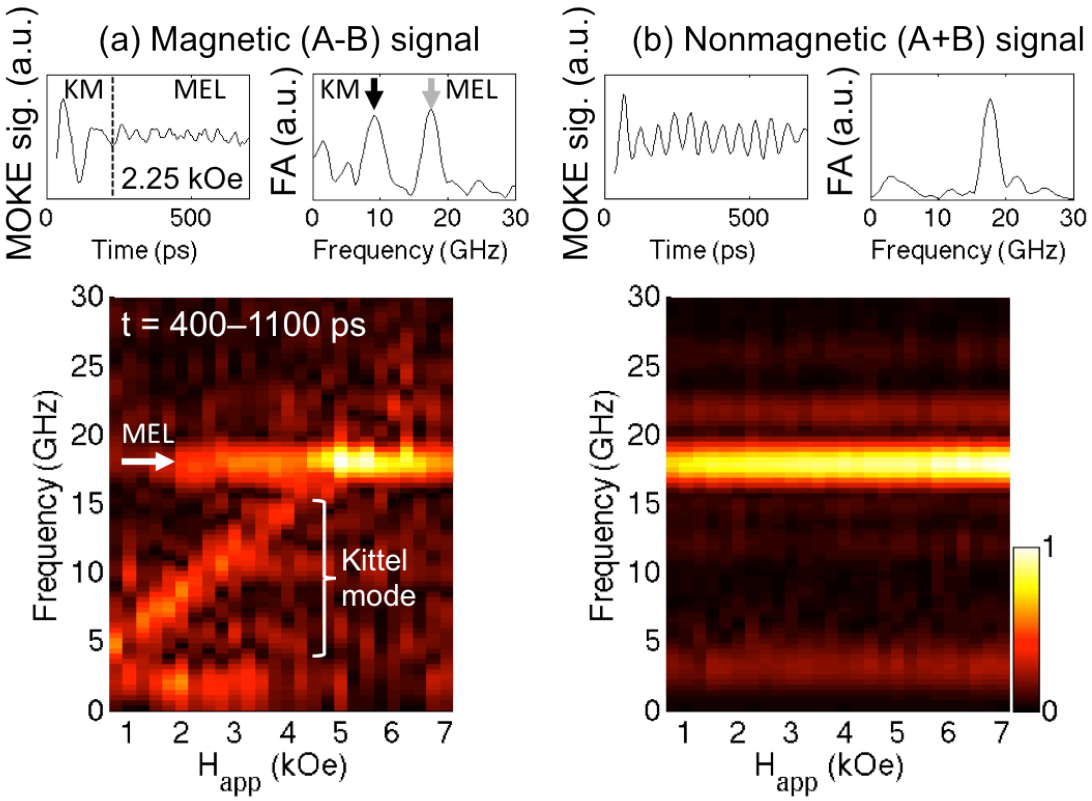

Fig. 7.2. (Top) Representative TR-MOKE time traces after background correction and the corresponding Fourier amplitude spectra, measured on the TbFe arrays at H_{app} = 2.25 kOe applied at θ_H = 60° from the surface normal. (Bottom) Fourier amplitude spectra at varying H_{app}.

To quantify the range of H_{app} where the precession is dominated by the magnetoelastic field $\boldsymbol{H}_{MEL}$ from SAWs, we analyzed sections of the TR-MOKE time traces after the intrinsic magnetic mode has damped out. Namely, Fourier transform was applied to time sections of t = 400–1100 ps as shown in Fig. 7.3. The starting time of the analyzed sections is more than four times as late as the characteristic decay time of the intrinsic magnetic modes and ensures that the magnetization

dynamics are exclusively driven by the pseudo-steady magnetoelastic field $\boldsymbol{H}_{\mathrm{MEL}}$ in the analyzed time sections. This observation provides stronger evidence of the magnetoelastically coupled dynamics beyond leakage of SAW oscillations observed in the A-B signal due to imperfect setup alignment. When this condition is not met, the Fourier amplitude of the intrinsic magnetic mode is superimposed as well and makes the pinning appear wider. While the Fourier spectra (Fig. 7.3a, b) do not show the intrinsic Kittel mode with varying frequency, the magnetoelastic mode pinned at f_{SAW} remains in the spectra due to its longer decay time and shows enhanced amplitude at the crossover field. The complex Fourier amplitude of the magnetic signal $\hat{w}_{\mathrm{M}} = |\hat{w}_{\mathrm{M}}|\exp(i\phi_{\mathrm{M}})$ at varying H_{app} was traced at f_{SAW} = 17.8 GHz as indicated with the dashed line in Fig. 7.3a. To adjust the phase relative to the nonmagnetic signal and to compensate for small drifts in the laser power, $\hat{w}_{\mathrm{M}}$ was scaled to the likewise traced nonmagnetic signal $\hat{w}_{\mathrm{NM}} = |\hat{w}_{\mathrm{NM}}|\exp(i\phi_{\mathrm{NM}})$ as

$$\hat{w}_{\mathrm{M,adj}}\Big|_{f=f_{\mathrm{SAW}}} = \frac{\hat{w}_{\mathrm{M}}}{\hat{w}_{\mathrm{NM}}}\Bigg|_{f=f_{\mathrm{SAW}}} = \frac{\hat{w}_{\mathrm{M}}}{|\hat{w}_{\mathrm{NM}}|}\exp(-i\phi_{\mathrm{NM}})\Bigg|_{f=f_{\mathrm{SAW}}}. \tag{7.3.1}$$

The real and imaginary parts are normalized to the range of [-1,1] and plotted in Fig. 7.3c. Instead of simply tracing the Fourier amplitudes $\hat{w}_{\mathrm{M}}$ at f_{SAW}, one can also integrate it over some frequency range (~ 1 GHz) but it does not improve the noisiness of the outcome in Fig. 7.3c. By minimizing the sum of the square error with the Lorentzian shape for both real and imaginary parts, the pinning width ΔH_{P} = 3154 Oe was obtained. Note that the absolute Fourier amplitude, as presented in Fig. 7.3a, has a somewhat wider peak at f_{SAW} and one has to decompose it to the real and

imaginary parts for accurate estimation. By substituting this ΔH_P value to Eq. (7.2.15), the Gilbert damping is estimated to be α = 0.25 for the patterned TbFe nanomagnets. This number coarsely agrees with the expected damping in literature [106] and demonstrates the extraction of damping values from complicated magnetoelastically-driven magnetization dynamics.

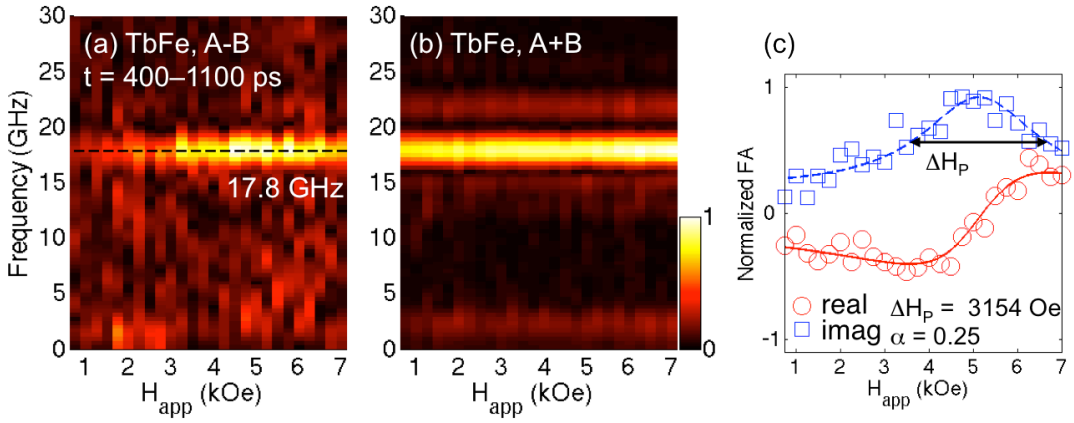

Fig. 7.3. (a, b) Absolute Fourier amplitude apectra of the magnetic (a) and (b) nonmagnetic signals, measured on the TbFe milled dots with the field applied at θ_H = 60° from the surface normal. The time section t = 400–1100 ps was analyzed. The horizontal dashed line indicates the fundamental SAW frequency at f_{SAW} = 17.8 GHz. (c) Normalized complex Fourier amplitude of the magnetic signal traced at f_{SAW}, after phase adjustment and scaling with the nonmagnetic signal. The circles and squares represent the real and imaginary parts, respectively. The solid and dashed lines are Lorentzian fits. The obtained pinning width ΔH_P and the Gilbert damping estimated with Eq. (7.2.15) are also displayed.

To rule out the possibility that the large magnetoelastic coefficients B_i of TbFe contribute to the large ΔH_P, we investigated different materials with various B_i and α, namely the polycrystalline nickel and cobalt nanomagnets presented in section 7.1 (Fig. 7.1 and Table 7.1). While nickel is less magnetoelastic (B_i = 7.85 MJ/m^3), cobalt has large magnetoelastic coefficients (B_i = 25.6 MJ/m^3 [215]) comparable to TbFe (B_i = -22.5 MJ/m^3). 30-nm-thick nickel and cobalt squares with average sizes of 125 and 160 nm, respectively, and array pitch p = 250 nm were deposited with the e-beam lithography, e-beam evaporation, and liftoff process on a substrate with a 110-nm-thick hafnium oxide antireflection (AR) coating. The nickel and cobalt arrays were measured under the field applied at θ_H = 30° and characterized in the same manner as the TbFe. Time sections of t = 1750–2450 ps were analyzed, where the precession was exclusively driven by the SAWs. Again, the starting time of the analyzed time sections was chosen to be more than four times larger than the characteristic exponential decay time of the magnetization precession observed in the films.

The resulting Fourier spectra for the nickel and cobalt arrays are presented in Fig. 7.4 and 7.5. Fig. 7.4c and 7.5c show the complex Fourier amplitudes traced at the fundamental SAW frequency f_{SAW} = 10.1 GHz. The difference in the fundamental SAW frequencies in each array (f_{SAW} = 10.1 GHz for nickel and cobalt and 17.8 GHz for TbFe) is attributed to the SAW velocity in different substrates structures (a 100-nm-thick SiO_2 for the TbFe array instead of the 110-nm-thick hafnium oxide AR coating layer in nickel and cobalt arrays). After adjusting its phase and magnitude

with the sum signal, the real and imaginary parts exhibit Lorentzian curves around the crossover field. As seen in Fig. 7.4c, the complex Fourier amplitude of the nickel array at f_{SAW} was fitted well with two equal-width Lorentzian peaks, corresponding to the crossover of the edge and center modes. For the cobalt array (Fig. 7.5), the fit was carried out with more measurements with smaller H_{app} steps than in the nickel array, in order to resolve the narrower pinning width ΔH_P with smaller signal to noise ratio. The pinning width for the nickel and cobalt arrays were found similar at ΔH_P = 388 and 385 Oe, respectively, despite the B_i of cobalt being more than three times as large as that of nickel. They both are distinctly smaller than the ΔH_P = 3154 Oe observed in the TbFe array, which has a comparable B_i as Co. Therefore, as predicted by Eq. (7.2.14), ΔH_P is characterized by the damping parameter α and not by B_i. Substituting the observed ΔH_P values in Eq. (7.2.15), the damping parameters were estimated as α = 0.059 for both nickel and cobalt nanomagnets and found close to the expected value.

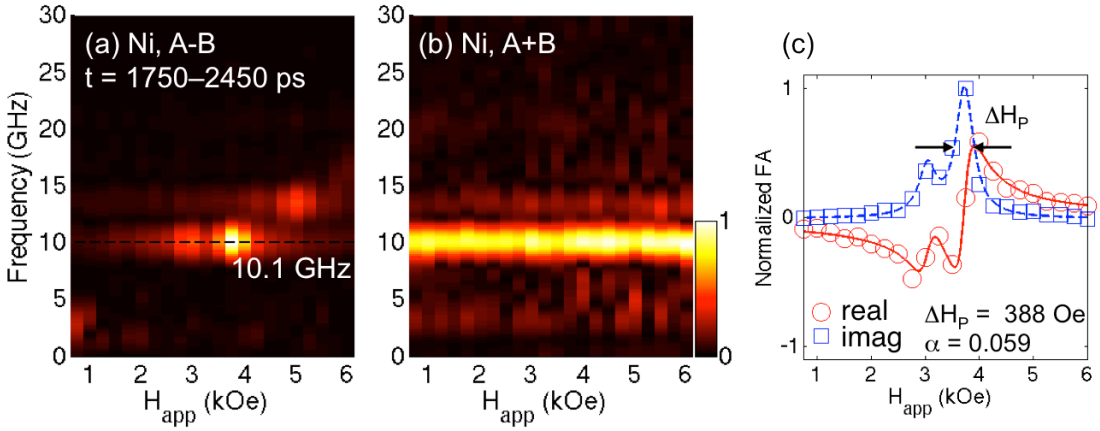

Fig. 7.4. (a, b) Absolute Fourier amplitude spectra of the magnetic (a) and (b) nonmagnetic signals measured on the nickel squares with the field applied at θ_H = 30º. Time section t = 1750–2450 ps was analyzed. The dashed line indicates the fundamental SAW frequency at f_{SAW} = 10.1 GHz. (c) Normalized complex Fourier amplitude of the magnetic signal traced at f_{SAW}, after phase adjustment and scaling with the nonmagnetic signal. The circles and squares represent the real and imaginary parts, respectively. The solid and dashed lines are Lorentzian fits. Two equal-width Lorentzian peaks were assumed for the fit, corresponding to the crossover of the center and edge modes. The obtained pinning width ΔH_P and the Gilbert damping parameter α estimated with Eq. (7.2.15) are also displayed.

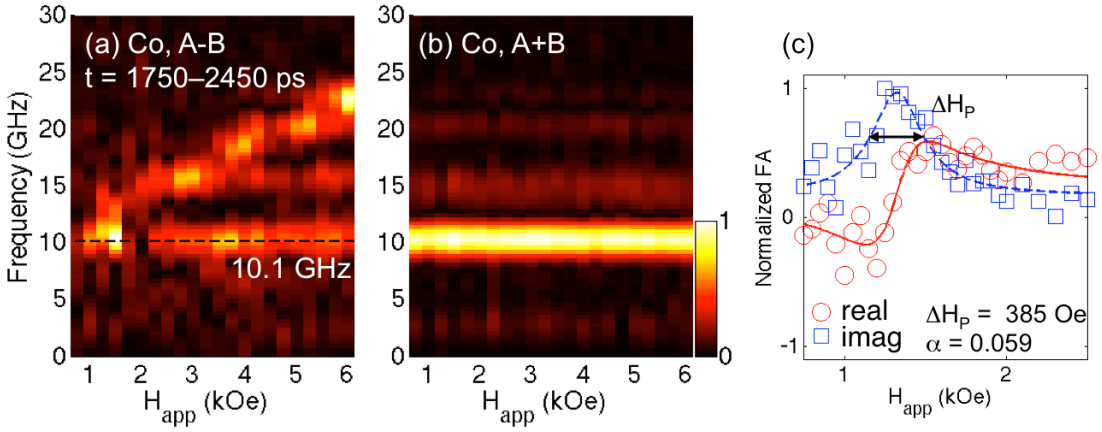

Fig. 7.5. (a, b) Absolute Fourier amplitude spectra of the magnetic (a) and (b) nonmagnetic signals measured on the cobalt squares with the field applied at θ_H = 30º. Time section t = 1750–2450 ps was analyzed. The dashed line indicates the fundamental SAW frequency at f_{SAW} = 10.1 GHz. (c) Normalized complex Fourier

amplitude of the magnetic signal traced at f_{SAW}, after phase adjustment and scaling with the nonmagnetic signal. The circles and squares represent the real and imaginary parts, respectively. The solid and dashed lines are Lorentzian fits. The obtained pinning width ΔH_P and the Gilbert damping parameter estimated with Eq. (7.2.15) are also displayed.

7.3.2 Comparison to damping analysis by fitting time traces

For verification of the damping estimate with the pinning width ΔH_P as described in the previous section, we compared the results to the damping estimate by fitting the time traces with the damped harmonic oscillation. As illustrated in Fig. 7.2a, the intrinsic magnetic oscillation of TbFe appears only in the first few 100 ps due to its large damping. In this case, we can only use a short time section for fitting and digital filtering described in section 3.4 is prone to induce an error by changing the waveform of the beginning of the time traces via the end effect, which is always found in the filtered signal. Instead of filtering, separation of the intrinsic magnetic mode from the SAW-coupled magnetoelastic oscillations was achieved by analyzing only the first few 100 ps of the time traces. Without digital filtering and background correction, the beginning part of time traces was fitted with a damped harmonic oscillation with the exponentially decaying background term and a constant offset

$$y(t) = A\exp\left(-\frac{t}{\tau}\right)\cos\left(2\pi ft + \phi\right) + A_1\exp\left(-\frac{t}{\tau_1}\right) + A_0 . \tag{7.4.1}$$

Fig. 7.6a presents the fitting examples of TbFe time traces.

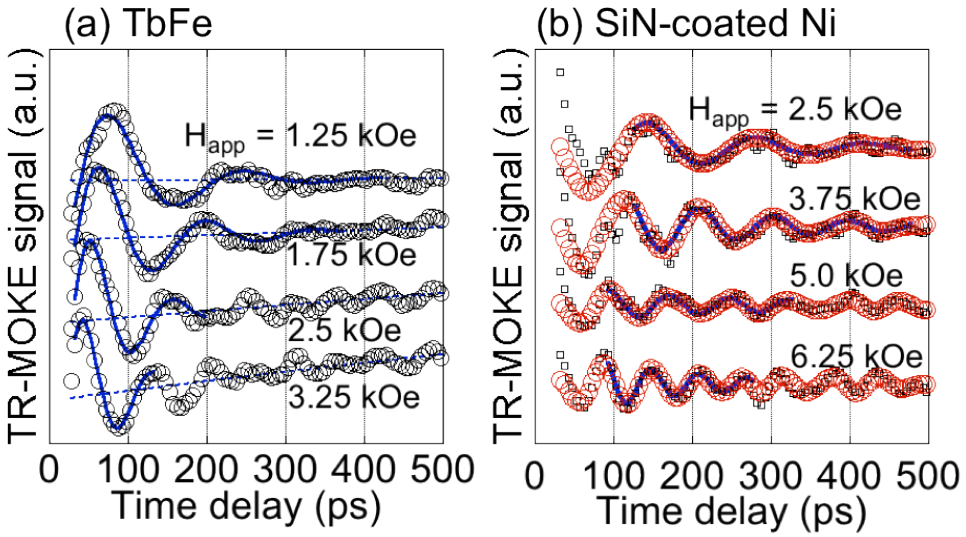

Fig. 7.6. (a) Representative time traces and fits of TbFe array. No background correction and filtering were applied in order to maintain the waveform in the first few 100 ps. (b) Representative time traces and fits of a SiN-coated nickel array. A 65 nm SiN coating was deposited to suppress SAW excitation. Butterworth filtering with 3 dB passband width of 6 GHz was applied (red open circles) before fitting with a damped oscillation (blue solid curves). The open squares represent the raw data.

Fitting of time traces for the nickel and cobalt arrays requires more elaborate care. Due to their relatively small damping, the intrinsic magnetic precession could not be separated from the SAW-driven magnetoelastic oscillations even with filtering, unlike TbFe where the intrinsic magnetic precession distinctly dominates the first few 100 ps of the magnetic signal. Their apparent damping obtained from time-domain analysis appeared much smaller than the expected value, especially at the crossover

field. The oscillation magnitude sometimes even increased over time, resulting in the negative apparent damping. To avoid this problem, a 65 nm silicon nitride coating was deposited on the nickel array. The added dielectric layer suppresses the excitation of SAWs and enables more reliable characterization of the Gilbert damping from the TR-MOKE time traces. The signal, however, degraded because of a broken AR condition due to the additional layer. There is room for optimizing the MOKE signal taking this suppression dielectric layer into account. Fig. 7.6b shows representative fits of the time traces of the coated nickel array. The Butterworth filter (3 dB passband width of 6 GHz) was applied in order to reject the noise and small remnant leakage of SAWs in the difference channel, as well as to eliminate the low frequency component induced by an error in background correction. Filtered data was fitted with a damped harmonic oscillation

$$y(t) = A\exp\left(-\frac{t}{\tau}\right)\cos\left(2\pi ft + \phi\right) + A_0 . \qquad (7.4.2)$$

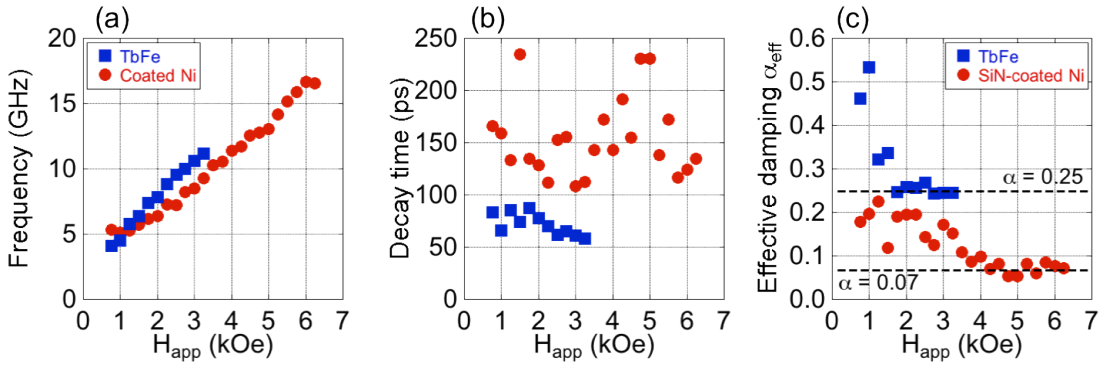

Fig. 7.7. Fitting results of the coated nickel and TbFe time traces and estimate of the effective damping. (a, b) Frequency (a) and decay time (b) obtained by the fit of the

coated Ni and TbFe time traces. (c) Estimated effective damping α_{eff} by the fitting results. The horizontal dashed lines indicate the intrinsic damping values estimated as the limit of α_{eff} at sufficiently high H_{app}.

Fig. 7.7 shows the fitted frequency f and decay time τ for the coated nickel and TbFe nanomagnets. Using these fitting results, the effective damping parameter $\alpha_{eff} = 1/(2\pi f\tau)$ [104] was calculated and is presented in Fig. 7.7c. α_{eff} in both coated nickel and TbFe turned out large for the low field range. This is due to extrinsic damping effects, such as the anisotropy dispersion [162,163] or incoherent spin waves [104,164], and is commonly observed in TR-MOKE time traces. At high fields, however, α_{eff} converges to a constant values of 0.25 at $H_{app} > 1.75$ kOe for TbFe and 0.07 at $H_{app} > 4.0$ kOe for the coated nickel. These values are expected to be close to the intrinsic Gilbert damping [162,163] and are in excellent agreement with the estimate by the pinning width characterization, obtained in the previous section. Above $H_{app} = 3.5$ kOe, the magnitude of the intrinsic magnetic oscillation in TbFe time traces became small and we could not fit them reliably. Nevertheless, α_{eff} stays at a constant value for $H_{app} = 1.75$–3.25 kOe and indicates that it has reached the intrinsic value. TbFe measurements were repeated at the field orientation of $\theta_H = 30°$ at which the nickel and cobalt arrays were characterized. The fitting of time traces yielded similar results of α_{eff} converging at 0.25 at sufficiently large H_{app}.

7.4 Demonstration of the concept with simulations

For further verification of the damping estimate with the pinning width characterization, a series of micromagnetic simulations with varying parameters was carried out. An array of 125×125×30 nm^3 squares on a 110 nm hafnium oxide AR coating layer with 250 nm pitch is simulated with the magnetoelastic field from SAWs as described in section 5.4. The elastic parameters were taken from the nickel arrays on hafnium oxide AR coating layer. M_s = 350 kA/m and the free electron gyromagnetic ratio $\gamma = 2.211\times10^5$ m/A/s were used. The Gilbert damping α and the magnetoelastic coefficients B_i were changed in order to investigate the effect of each parameter. The time evolution of m_z is computed for 2.5 ns and the Fourier transform was performed with the time section of t = 1750–2450 ps as in the same manner as the experiments in section 7.3.1.

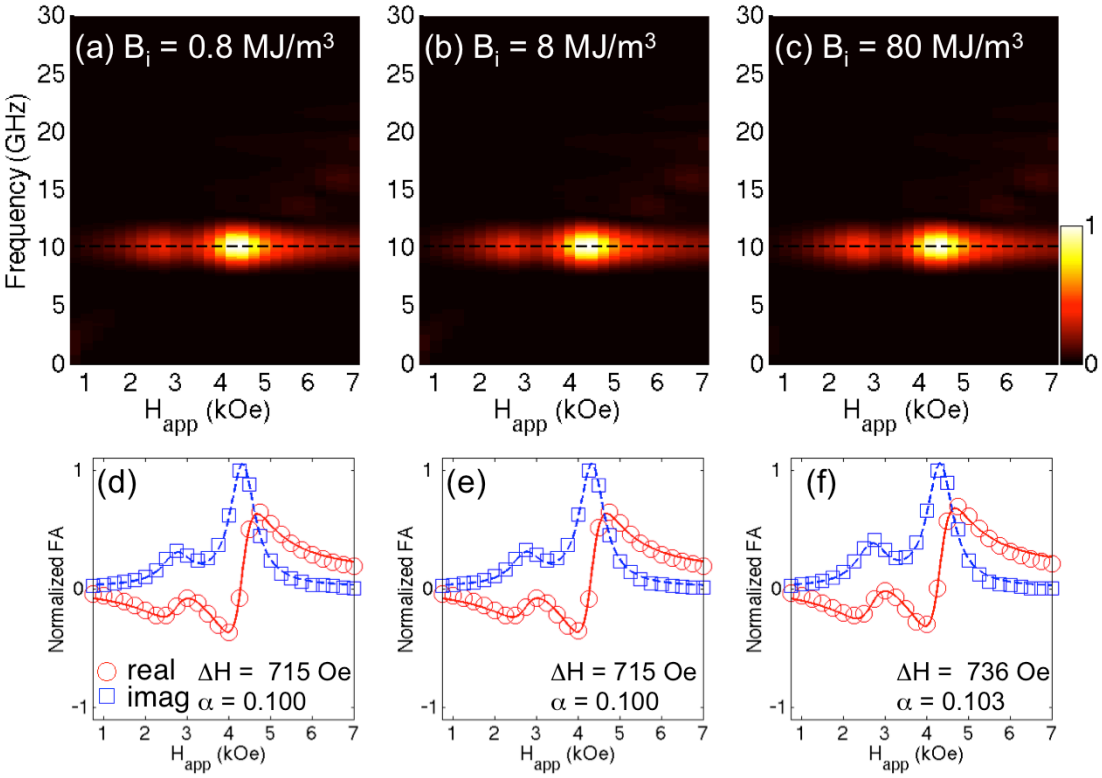

Fig. 7.8. (a–c) Simulated absolute Fourier spectra for various magnetoelastic coefficients B_i, while keeping an identical value of α = 0.1. A time section of t = 1750–2450 ps was analyzed. (d–f) Calculated complex Fourier amplitude at f_{SAW} (symbols) and the fit with two Lorentzian peaks (lines).

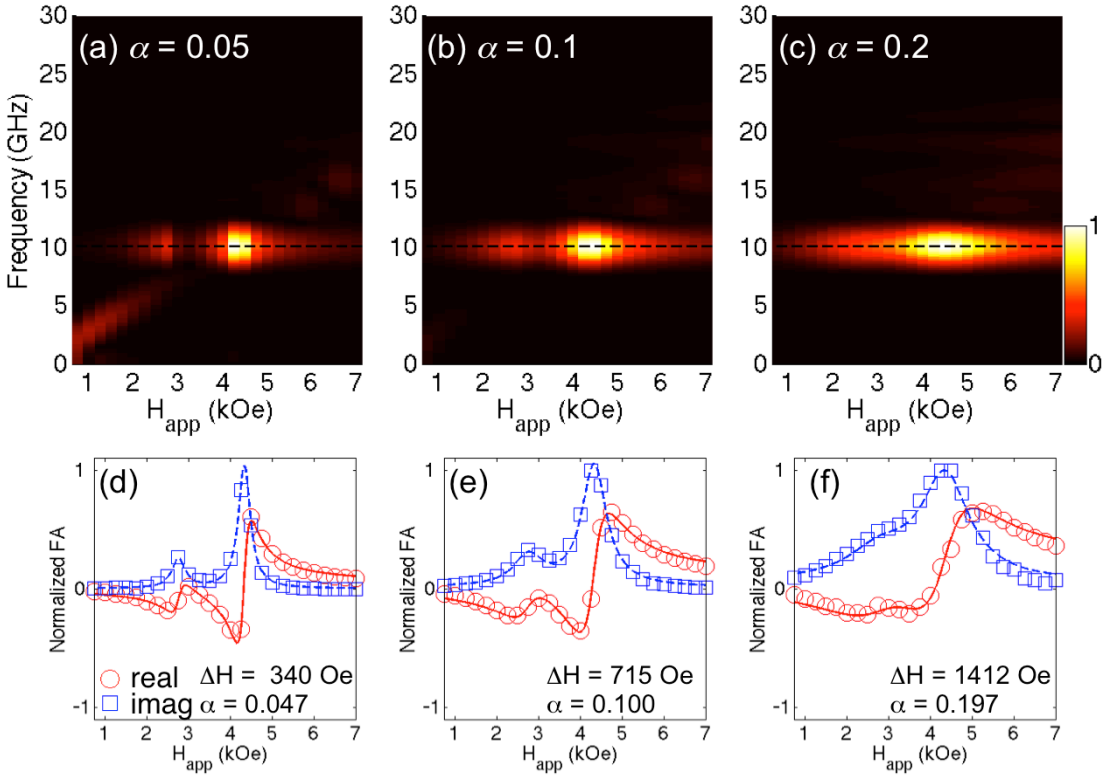

Fig. 7.9. (a–c) Simulated absolute Fourier spectra for various damping parameters α, while keeping identical magnetoelastic coefficients B_i = 8 MJ/m^3. A time section of t = 1750–2450 ps was analyzed. (d–f) Calculated complex Fourier amplitude at f_{SAW} (symbols) and the fit with two Lorentzian peaks (lines).

Fig. 7.8 shows the simulated spectra of m_z with varying B_i = 8×10^4–8×10^7 J/m^3 and constant α = 0.1. As in the colormaps in Fig. 7.8a–c, the spectra show pinning at f_{SAW} = 10.1 GHz SAW frequency. The two peaks at 3.25 and 4.75 kOe mark the crossover of the edge mode and center mode with the fundamental SAW frequency. The bottom row presents the complex Fourier amplitudes at f_{SAW}, after adjustment of their phase and magnitude, as described in section 7.3.1 but using the

driving displacement u_z at the center of the squares instead of the nonmagnetic signal as in the experiments. The obtained pinning width ΔH_P and the damping estimated by Eq. (7.2.15) are also shown. In Fig. 7.9, the magnetoelastic response was simulated with varying Gilbert damping α while keeping $B_i = 8\times10^6$ J/m^3 constant. In contrast to the above results with varying B_i (Fig. 7.8), the pinning width ΔH_P shows clear dependence on α. The resulted pinning width ΔH_P and the damping estimate are summarized in Fig. 7.10. They show that ΔH_P is proportional to α but unaffected by changes in B_i over three orders of magnitude, as suggested by the observations in experimental data on nickel, cobalt, and TbFe in section 7.3. It also shows that the estimated α closely agrees with the Gilbert damping values specified in the simulations and further verifies the accuracy of damping characterization with the pinning width ΔH_P.

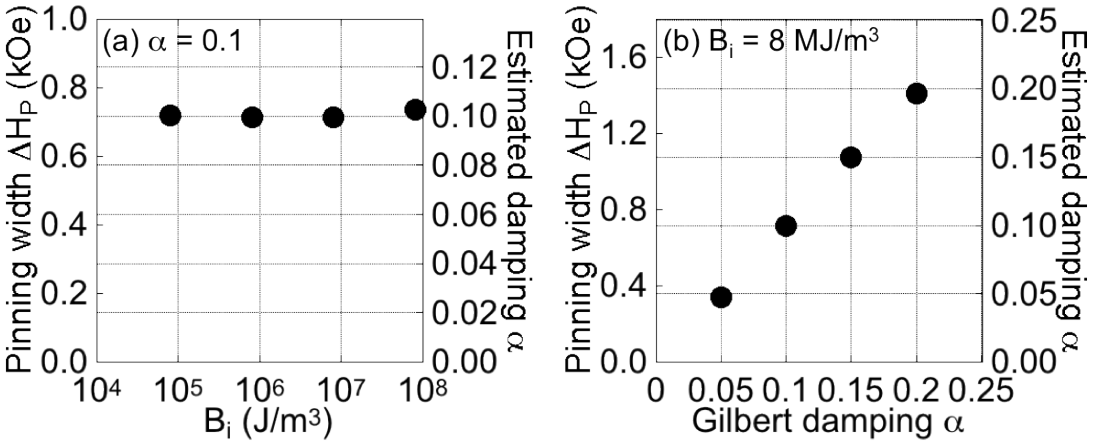

Fig. 7.10. Plots of estimated pinning width ΔH_P and α as functions of the magnetoelastic coefficients B_i and the Gilbert damping α specified in the simulations.

From ΔH_P, α was estimated with Eq. (7.2.15) and displayed with the second vertical axes.

7.5 Summary

The magnetoelastic dynamics of the patterned nanomagnets of various materials were investigated. Contrary to the original expectation that the high magnetoelastic coefficients B_i would lead to strong dominance of the SAWs over a wider field range, the pinning width of the precession frequency was found independent of B_i. Instead, it was shown to depend solely on the phenomenological damping parameter α of the nanomagnets. The finding was supported by the magnetic susceptibility for small amplitude oscillation with pseudo-steady $\boldsymbol{H}_{MEL}$ as the driving field as well as by micromagnetic simulations. Conversely, this demonstrates accurate estimation of the intrinsic damping in patterned nanomagnet arrays where the SAWs heavily complicate magnetization dynamics and other experimental techniques are restrictive.

8. Summary

In this thesis, we discussed the measurements and modeling of the nanopatterned transition metal magnet arrays, with the emphasis on the magnetostatic and magnetoelastic effects in closely located nanomagnets. Dynamics of nanomagnet arrays, distinctly different from the bulk materials, were probed using all-optical TR-MOKE setup, complemented with micromagnetic modeling.

In Chapter 4, we discussed the magnetization response and the magnetostatic interelement interactions probed with the dynamic separation technique. Using the frequency-domain information, the magneto-optical signals, composed of responses from many nanomagnets, were separated into subgroups of nanomagnets. We characterized arrays of identically shaped nanomagnets, oriented along orthogonal directions. Responses of individual subgroups were resolved beyond the diffraction-limited spatial resolution. With micromagnetic simulations, the magnetostatic effect of one subgroup to the other was modeled, correctly reproducing the experimental observations. Relatively small effect of the dipole field from the neighboring elements was attributed to the smaller total magnetic moment of thinner nanomagnets than our previous reports [81]. The technique demonstrated the ability of differentiating the identical nanomagnets within arrays. Suggested future work involves elements with identical shape and orientation, made of different materials, for characterizing a single magnet embedded in a dense array. If the difficulty for fabricating such array is resolved, single nanomagnets may be evaluated in a realistic magnetostatic environment.

The following chapters were devoted for characterization of the magnetoelastic dynamics in nanostructures. Preceding studies on magnetoelastic dynamics were limited to simple configurations due to mathematical complexity. By carefully eliminating intermixing of magnetic and nonmagnetic TR-MOKE signals, we proved strong coupling between the magnetic and elastic oscillation modes, simultaneously excited by the pump laser pulse. A numerical approach was developed for modeling their coupled response. By including an additional magnetoelastic contribution, micromagnetic simulations reproduced experimental findings with excellent accuracy. This demonstration provided crucial pieces of knowledge and implications about the ultrafast magnetization dynamics in nanomagnet arrays. First of all, the strong magnetoelastic effect indicates the importance of elastic design via sample geometry. For suppressing or avoiding this effect in order to observe the purely magnetic response, one must be aware of the eminent presence of the magnetoelastic coupling. Conversely, the magnetoelastic effect can also be utilized for signal enhancement and magnetization manipulation, as demonstrated in the last chapter. Finally, the numerical simulation procedure developed for this analysis is applicable to a broader range of problems with arbitrary structures.

Utilizing the validated measurement and modeling techniques for magnetoelastic dynamics, we developed a novel experimental method to characterize the phenomenological damping parameter of nanomagnet arrays. The magnetoelastic effective field acted as a pseudo-steady alternating field and drove the magnetization precession. By scanning the external field, the Fourier amplitude of the

magnetoelastic mode exhibited a Lorentz resonance curve and the damping parameter was accurately characterized from its linewidth. The validity of the method was verified through comparison to another experimental method and micromagnetic modeling with magnetoelastic contributions. The new method maintains advantages of TR-MOKE—a high spatial resolution and high sensitivity for small-sized samples—while avoiding the usual difficulties associated with the time-domain analysis. This technique can be used for evaluating critical operation characteristics of spintronic devices. For example, damping evaluation in CoFeB magnetic tunneling junctions will yield an important insight about their performance under the influence of small size and fabrication defects.

References

[1] T. Valet, and a Fert, “Theory of the perpendicular magnetoresistance in magnetic multilayers,” *Phys. Rev. B* **48**, 7099–7113 (1993).

[2] A. Fert, J.-L. Duvail, and T. Valet, “Spin relaxation effects in the perpendicular magnetoresistance of magnetic multilayers,” *Phys. Rev. B* **52**, 6513–6521 (1995).

[3] M. N. N. Baibich, J. M. M. Broto, A. Fert, F. N. Van Dau, and F. Petroff, “Giant Magnetosresistance of (001)Fe/(001)Cr Magnetic Superlattices,” *Phys. Rev. Lett.* **61**, 2472–2475 (1988).

[4] G. Binasch, P. Grünberg, F. Saurenbach, and W. Zinn, “Enhanced magnetoresistance in layered magnetic structures with antiferromagnetic interlayer exchange,” *Phys. Rev. B* **39**, 4828–4830 (1989).

[5] T. Miyazaki, and N. Tezuka, “Giant magnetic tunneling effect in Fe/Al2O3/Fe junction,” *J. Magn. Magn. Mater.* **139**, L231–L234 (1995).

[6] J. S. Moodera, L. R. Kinder, T. M. Wong, and R. Meservey, “Large magnetoresistance at room temperature in ferromagnetic thin film tunnel junctions,” *Phys. Rev. Lett.* **74**, 3273–3276 (1995).

[7] S. N. Piramanayagam, “Perpendicular recording media for hard disk drives,” *J. Appl. Phys.* **102**, 011301 (2007).

[8] S. Iwasaki, “Perpendicular Magnetic Recording,” *IEEE Trans. Magn.* **16**, 71–76 (1980).

[9] R. Wood, “Future hard disk drive systems,” *J. Magn. Magn. Mater.* **321**, 555–561 (2009).

[10] J. K. W. Yang, Y. Chen, T. Huang, H. Duan, N. Thiyagarajah, H. K. Hui, S. H. Leong, and V. Ng, “Fabrication and characterization of bit-patterned media beyond 1.5 Tbit/in2.,” *Nanotechnology* **22**, 385301 (2011).

[11] C. Chappert, A. Fert, and F. N. Van Dau, “The emergence of spin electronics in data storage.,” *Nat. Mater.* **6**, 813–823 (2007).

[12] R. E. Fontana, G. M. Decad, and S. R. Hetzler, “Volumetric density trends (TB/in.3) for storage components: TAPE, hard disk drives, NAND, and Blu-ray,” *J. Appl. Phys.* **117**, 17E301 (2015).

[13] L. Néel, Ann. Geophys. (C.N.R.S.) **5**, 99 (1949).

[14] W. F. Brown, “Thermal fluctuations of a single-domain particle,” *Phys. Rev.* **130**, 1677–1686 (1963).

[15] J. Z. Sun, “Spin-current interaction with a monodomain magnetic body: A model study,” *Phys. Rev. B* **62**, 570–578 (2000).

[16] G. Fiedler, J. Fidler, J. Lee, T. Schrefl, R. L. Stamps, H. B. Braun, and D. Suess, “Direct calculation of the attempt frequency of magnetic structures using the finite element method,” *J. Appl. Phys.* **111**, 093917 (2012).

[17] C. A. Ross, H. I. Smith, T. Savas, M. Schattenburg, M. Farhoud, M. Hwang, M. Walsh, M. C. Abraham, and R. J. Ram, “Fabrication of patterned media for high density magnetic storage,” *J. Vac. Sci. Technol. B Microelectron. Nanom. Struct.* **17**, 3168 (1999).

[18] B. D. Terris, and T. Thomson, “Nanofabricated and self-assembled magnetic structures as data storage media,” *J. Phys. D. Appl. Phys.* **38**, R199–R222 (2005).

[19] A. Kikitsu, “Prospects for bit patterned media for high-density magnetic recording,” *J. Magn. Magn. Mater.* **321**, 526–530 (2009).

[20] M. A. Seigler et al., “Heat Assisted Magnetic Recording with a Fully Integrated Recording Head,” *Proc. SPIE* **6620**, edited by B. Bell and T. Shimano, 66200P (2007).

[21] M. H. Kryder, E. C. Gage, T. W. McDaniel, W. A. Challener, R. E. Rottmayer, G. Ju, Y.-T. Hsia, and M. F. Erden, “Heat Assisted Magnetic Recording,” *Proc. IEEE* **96**, 1810–1835 (2008).

[22] W. A. Challener et al., “Heat-assisted magnetic recording by a near-field transducer with efficient optical energy transfer,” *Nat. Photonics* **3**, 220–224 (2009).

[23] X. Wang, K. Gao, H. Zhou, A. Itagi, M. Seigler, and E. Gage, “HAMR Recording Limitations and Extendibility,” *IEEE Trans. Magn.* **49**, 686–692 (2013).

[24] D. Weller, G. Parker, O. Mosendz, E. Champion, B. Stipe, X. Wang, T. Klemmer, G. Ju, and A. Ajan, “A HAMR media technology roadmap to an areal density of 4 Tb/in2,” *IEEE Trans. Magn.* **50**, 1–8 (2014).

[25] T. Rausch, A. S. Chu, P.-L. Lu, S. Puranam, D. Nagulapally, T. Lammers, J. W. Dykes, and E. C. Gage, “Recording Performance of a Pulsed HAMR Architecture,” *IEEE Trans. Magn.* **51**, 1–5 (2015).

[26] J. M. Daughton, “Magnetic tunneling applied to memory (invited),” J. Appl. Phys. 81, 3758 (1997).

[27] S. Tehrani et al., “Magnetoresistive random access memory using magnetic tunnel junctions,” *Proc. IEEE* **91**, 703–714 (2003).

[28] B. N. Engel et al., “A 4-Mb toggle MRAM based on a novel bit and switching method,” *IEEE Trans. Magn.* **41**, 132–136 (2005).

[29] D. Apalkov et al., “Spin-transfer torque magnetic random access memory (STT-MRAM),” *J. Emerg. Technol. Comput. Syst.* **9**, 13:1 (2013).

[30] S. S. P. Parkin, C. Kaiser, A. Panchula, P. M. Rice, B. Hughes, M. Samant, and S.-H. Yang, “Giant tunnelling magnetoresistance at room temperature with MgO (100) tunnel barriers.,” *Nat. Mater.* **3**, 862–867 (2004).

[31] S. Yuasa, T. Nagahama, A. Fukushima, Y. Suzuki, and K. Ando, “Giant room-temperature magnetoresistance in single-crystal Fe/MgO/Fe magnetic tunnel junctions,” *Nat. Mater.* **3**, 868–871 (2004).

[32] D. D. Djayaprawira, K. Tsunekawa, M. Nagai, H. Maehara, S. Yamagata, N. Watanabe, S. Yuasa, Y. Suzuki, and K. Ando, “230% room-temperature magnetoresistance in CoFeB/MgO/CoFeB magnetic tunnel junctions,” *Appl. Phys. Lett.* **86**, 092502 (2005).

[33] J. Hayakawa, S. Ikeda, F. Matsukura, H. Takahashi, and H. Ohno, “Dependence of giant tunnel magnetoresistance of sputtered CoFeB/MgO/CoFeB magnetic tunnel junctions on MgO barrier thickness and annealing temperature,” *Japanese J. Appl. Physics, Part 2 Lett.* **44**, 2–5 (2005).

[34] Z. Diao, D. Apalkov, M. Pakala, Y. Ding, A. Panchula, and Y. Huai, “Spin transfer switching and spin polarization in magnetic tunnel junctions with MgO and AlO_x barriers,” *Appl. Phys. Lett.* **87**, 232502 (2005).

[35] J. Hayakawa, S. Ikeda, Y. M. Lee, F. Matsukura, and H. Ohno, “Effect of high annealing temperature on giant tunnel magnetoresistance ratio of CoFeB/MgO/CoFeB magnetic tunnel junctions,” *Appl. Phys. Lett.* **89**, 232510 (2006).

[36] Y. M. Lee, J. Hayakawa, S. Ikeda, F. Matsukura, and H. Ohno, “Effect of electrode composition on the tunnel magnetoresistance of pseudo-spin-valve magnetic tunnel junction with a MgO tunnel barrier,” *Appl. Phys. Lett.* **90**, 23–25 (2007).

[37] J. C. Slonczewski, “Current-driven excitation of magnetic multilayers,” *J. Magn. Magn. Mater.* **159**, L1–L7 (1996).

[38] L. Berger, “Emission of spin waves by a magnetic multilayer traversed by a current,” *Phys. Rev. B* **54**, 9353–9358 (1996).

[39] E. B. Myers, “Current-Induced Switching of Domains in Magnetic Multilayer Devices,” *Science* **285**, 867–870 (1999).

[40] J. Katine, F. Albert, R. Buhrman, E. Myers, and D. Ralph, “Current-driven magnetization reversal and spin-wave excitations in Co /Cu /Co pillars,” *Phys. Rev. Lett.* **84**, 3149–3152 (2000).

[41] Y. Huai, F. Albert, P. Nguyen, M. Pakala, and T. Valet, “Observation of spin-transfer switching in deep submicron-sized and low-resistance magnetic tunnel junctions,” *Appl. Phys. Lett.* **84**, 3118 (2004).

[42] W. Zhao, S. Chaudhuri, C. Accoto, J.-O. Klein, D. Ravelosona, C. Chappert, and P. Mazoyer, “High Density Spin-Transfer Torque (STT)-MRAM Based on Cross-Point Architecture,” *2012 4th IEEE Int. Mem. Work.* **0**, 1–4, IEEE (2012).

[43] S. Ikeda, K. Miura, H. Yamamoto, K. Mizunuma, H. D. Gan, M. Endo, S. Kanai, J. Hayakawa, F. Matsukura, and H. Ohno, “A perpendicular-anisotropy CoFeB-MgO magnetic tunnel junction.,” *Nat. Mater.* **9**, 721–724 (2010).

[44] S. S. P. Parkin, M. Hayashi, L. Thomas, C. M. Lewandowski, S. S. P. Parkin, M. Hayashi, and L. Thomas, “Magnetic domain-wall racetrack memory.,” *Science* **320**, 190 (2008).

[45] H. Kubota et al., “Quantitative measurement of voltage dependence of spin-transfer torque in MgO-based magnetic tunnel junctions,” *Nat. Phys.* **4**, 37–41 (2008).

[46] A. M. Deac, A. Fukushima, H. Kubota, H. Maehara, Y. Suzuki, S. Yuasa, Y. Nagamine, K. Tsunekawa, D. D. Djayaprawira, and N. Watanabe, “Bias-driven high-power microwave emission from MgO-based tunnel magnetoresistance devices,” *Nat. Phys.* **4**, 803–809 (2008).

[47] A. A. Tulapurkar, Y. Suzuki, A. Fukushima, H. Kubota, H. Maehara, K. Tsunekawa, D. D. Djayaprawira, N. Watanabe, and S. Yuasa, “Spin-torque diode effect in magnetic tunnel junctions.,” *Nature* **438**, 339–342 (2005).

[48] C. D. Stanciu, F. Hansteen, A. V. Kimel, A. Kirilyuk, A. Tsukamoto, A. Itoh, and T. Rasing, “All-Optical Magnetic Recording with Circularly Polarized Light,” *Phys. Rev. Lett.* **99**, 047601 (2007).

[49] C. Stanciu, A. Tsukamoto, A. Kimel, F. Hansteen, A. Kirilyuk, A. Itoh, and T. Rasing, “Subpicosecond Magnetization Reversal across Ferrimagnetic Compensation Points,” *Phys. Rev. Lett.* **99**, 217204 (2007).

[50] S. Alebrand, A. Hassdenteufel, D. Steil, M. Cinchetti, and M. Aeschlimann, "Interplay of heating and helicity in all-optical magnetization switching," *Phys. Rev. B* **85**, 092401 (2012).

[51] T. A. Ostler et al., "Ultrafast heating as a sufficient stimulus for magnetization reversal in a ferrimagnet.," *Nat. Commun.* **3**, 666 (2012).

[52] K. Vahaplar et al., "All-optical magnetization reversal by circularly polarized laser pulses: Experiment and multiscale modeling," *Phys. Rev. B* **85**, 104402 (2012).

[53] M. Savoini et al., "Highly efficient all-optical switching of magnetization in GdFeCo microstructures by interference-enhanced absorption of light," *Phys. Rev. B* **86**, 140404 (2012).

[54] L. Le Guyader et al., "Demonstration of laser induced magnetization reversal in GdFeCo nanostructures," *Appl. Phys. Lett.* **101**, 022410 (2012).

[55] A. Hassdenteufel, B. Hebler, C. Schubert, A. Liebig, M. Teich, M. Helm, M. Aeschlimann, M. Albrecht, and R. Bratschitsch, "Thermally assisted all-optical helicity dependent magnetic switching in amorphous Fe(100-x)Tb(x) alloy films.," *Adv. Mater.* **25**, 3122–3128 (2013).

[56] C. Schubert, A. Hassdenteufel, P. Matthes, J. Schmidt, M. Helm, R. Bratschitsch, and M. Albrecht, "All-optical helicity dependent magnetic switching in an artificial zero moment magnet," *Appl. Phys. Lett.* **104**, 082406 (2014).

[57] A. Hassdenteufel, J. Schmidt, C. Schubert, B. Hebler, M. Helm, M. Albrecht, and R. Bratschitsch, "Low-remanence criterion for helicity-dependent all-optical magnetic switching in ferrimagnets," *Phys. Rev. B* **91**, 104431 (2015).

[58] T.-M. Liu et al., "Nanoscale Con fi nement of All-Optical Magnetic Switching in TbFeCo - Competition with Nanoscale Heterogeneity," *Nano Lett.* **15**, 6862 (2015).

[59] S. Mangin et al., "Engineered materials for all-optical helicity-dependent magnetic switching.," *Nat. Mater.* **13**, 286–292 (2014).

[60] R. F. L. Evans, T. A. Ostler, R. W. Chantrell, I. Radu, and T. Rasing, "Ultrafast thermally induced magnetic switching in synthetic ferrimagnets," *Appl. Phys. Lett.* **104**, 082410 (2014).

[61] I. Radu et al., "Transient ferromagnetic-like state mediating ultrafast reversal of antiferromagnetically coupled spins.," *Nature* **472**, 205–208 (2011).

[62] J. Mentink, J. Hellsvik, D. Afanasiev, B. Ivanov, A. Kirilyuk, A. Kimel, O. Eriksson, M. Katsnelson, and T. Rasing, "Ultrafast Spin Dynamics in Multisublattice Magnets," *Phys. Rev. Lett.* **108**, 057202 (2012).

[63] A. N. Slavin, S. O. Demokritov, and B. Hillebrands, "Nonlinear Spinwaves in One- and Two-Dimensional Magnetic Waveguides," 35–66 (2002).

[64] C. Bayer et al., "Spin-wave excitations in finite rectangular elements of Ni80Fe20," *Phys. Rev. B* **72**, 064427 (2005).

[65] V. V. Kruglyak, A. Barman, R. J. Hicken, J. R. Childress, and J. A. Katine, "Picosecond magnetization dynamics in nanomagnets: Crossover to nonuniform precession," *Phys. Rev. B* **71**, 220409 (2005).

[66] C. Bayer, J. Jorzick, S. Demokritov, A. N. Slavin, K. Y. Guslienko, D. V Berkov, N. L. Gorn, M. P. Kostylev, and B. Hilebrands, "Spin-wave excitations in finite rectangular elements," [Spin Dynamics in Confined Magnetic Structures II, Topics in Applied Physics], edited by B. Hillebrands and A. Thiaville, 57–103, (Springer, Berlin, Heidelberg 2006).

[67] M. L. Schneider, T. Gerrits, A. B. Kos, and T. J. Silva, "Experimental determination of the inhomogeneous contribution to linewidth in Permalloy films using a time-resolved magneto-optic Kerr effect microprobe," *J. Appl. Phys.* **102**, 053910 (2007).

[68] J. M. Shaw, H. T. Nembach, T. J. Silva, S. E. Russek, C. Jones, N. Clark, T. Leo, and D. J. Smith, "Effect of microstructure on magnetic properties and anisotropy distributions in Co/Pd thin films and nanostructures," *Phys. Rev. B* **80**, 184419 (2009).

[69] J. Jersch, V. E. Demidov, H. Fuchs, K. Rott, P. Krzysteczko, J. Münchenberger, G. Reiss, and S. O. Demokritov, "Mapping of localized spin-wave excitations by near-field Brillouin light scattering," *Appl. Phys. Lett.* **97**, 152502 (2010).

[70] A. Barman, V. Kruglyak, R. Hicken, J. Rowe, A. Kundrotaite, J. Scott, and M. Rahman, "Imaging the dephasing of spin wave modes in a square thin film magnetic element," *Phys. Rev. B* **69**, 174426 (2004).

[71] A. Barman, S. Wang, J. Maas, A. R. Hawkins, S. Kwon, J. Bokor, A. Liddle, and H. Schmidt, "Size dependent damping in picosecond dynamics of single nanomagnets," *Appl. Phys. Lett.* **90**, 202504 (2007).

[72] J. Walowski, M. D. Kaufmann, B. Lenk, C. Hamann, J. McCord, and M. Münzenberg, "Intrinsic and non-local Gilbert damping in polycrystalline nickel

studied by Ti : sapphire laser fs spectroscopy," *J. Phys. D. Appl. Phys.* **41**, 164016 (2008).

[73] K.-D. D. Lee, J.-W. W. Kim, J.-W. W. Jeong, and S.-C. C. Shin, "Nonuniform apparent relaxation from dephasing of magnetostatic wave modes in a confined microdisk," *J. Appl. Phys.* **106**, 113904 (2009).

[74] O. Ozatay et al., "Sidewall oxide effects on spin-torque- and magnetic-field-induced reversal characteristics of thin-film nanomagnets.," *Nat. Mater.* **7**, 567–573 (2008).

[75] H. T. Nembach, J. M. Shaw, T. J. Silva, W. L. Johnson, S. A. Kim, R. D. McMichael, and P. Kabos, "Effects of shape distortions and imperfections on mode frequencies and collective linewidths in nanomagnets," *Phys. Rev. B* **83**, 094427 (2011).

[76] J. M. Shaw, H. T. Nembach, and T. J. Silva, "Roughness induced magnetic inhomogeneity in Co/Ni multilayers: Ferromagnetic resonance and switching properties in nanostructures," *J. Appl. Phys.* **108**, 093922 (2010).

[77] J. Shaw, S. Russek, T. Thomson, M. Donahue, B. Terris, O. Hellwig, E. Dobisz, and M. Schneider, "Reversal mechanisms in perpendicularly magnetized nanostructures," *Phys. Rev. B* **78**, 024414 (2008).

[78] J. Shaw, M. Olsen, J. Lau, M. Schneider, T. Silva, O. Hellwig, E. Dobisz, and B. Terris, "Intrinsic defects in perpendicularly magnetized multilayer thin films and nanostructures," *Phys. Rev. B* **82**, 144437 (2010).

[79] P. S. Keatley, V. V. Kruglyak, A. Neudert, E. A. Galaktionov, R. J. Hicken, J. R. Childress, and J. A. Katine, "Time-resolved investigation of magnetization dynamics of arrays of nonellipsoidal nanomagnets with nonuniform ground states," *Phys. Rev. B* **78**, 214412 (2008).

[80] A. A. Awad, G. R. Aranda, D. Dieleman, K. Y. Guslienko, G. N. Kakazei, B. A. Ivanov, and F. G. Aliev, "Spin excitation frequencies in magnetostatically coupled arrays of vortex state circular Permalloy dots," *Appl. Phys. Lett.* **97**, 132501 (2010).

[81] Z. Liu, R. Brandt, Y. Yahagi, B. Hansen, B. Harteneck, J. Bokor, A. R. Hawkins, and H. Schmidt, "Detecting single nanomagnet dynamics beyond the diffraction limit in varying magnetostatic environments," *Appl. Phys. Lett.* **98**, 52502 (2011).

[82] K. J. J. Kirk, J. N. N. Chapman, S. McVitie, P. R. R. Aitchison, and C. D. W. D. W. Wilkinson, "Interactions and switching field distributions of nanoscale magnetic elements," *J. Appl. Phys.* **5105**, 10–13 (2000).

[83] M. C. Abraham, H. Schmidt, T. A. Savas, H. I. Smith, C. A. Ross, and R. J. Ram, "Magnetic properties and interactions of single-domain nanomagnets in a periodic array,"*J. Appl. Phys.* **89**, 5667 (2001).

[84] O. Hellwig, A. Berger, T. Thomson, E. Dobisz, Z. Z. Bandic, H. Yang, D. S. Kercher, and E. E. Fullerton, "Separating dipolar broadening from the intrinsic switching field distribution in perpendicular patterned media," *Appl. Phys. Lett.* **90**, 2005–2008 (2007).

[85] A. Barman, and S. Barman, "Dynamic dephasing of magnetization precession in arrays of thin magnetic elements," *Phys. Rev. B* **79**, 144415 (2009).

[86] V. V. Kruglyak, P. S. Keatley, A. Neudert, R. J. Hicken, J. R. Childress, and J. A. Katine, "Imaging Collective Magnonic Modes in 2D Arrays of Magnetic Nanoelements," *Phys. Rev. Lett.* **104**, 027201 (2010).

[87] B. Rana, D. Kumar, S. Barman, S. Pal, R. Mandal, Y. Fukuma, Y. Otani, S. Sugimoto, and A. Barman, "Anisotropy in collective precessional dynamics in arrays of Ni80Fe20 nanoelements," *J. Appl. Phys.* **111**, 07D503 (2012).

[88] W. Kim, T.-D. Lee, J.-E. Lee, S.-C. Oh, K.-H. Shin, H.-J. Suh, and K.-J. Lee, "Enhanced switching current density due to resonant precession in current-induced magnetization switching," *Appl. Phys. Lett.* **90**, 212504 (2007).

[89] N. Qureshi, S. Wang, M. A. Lowther, A. R. Hawkins, S. Kwon, A. Liddle, J. Bokor, and H. Schmidt, "Cavity-enhanced magnetooptical observation of magnetization reversal in individual single-domain nanomagnets.," *Nano Lett.* **5**, 1413–1417 (2005).

[90] A. Barman, S. Wang, J. D. Maas, A. R. Hawkins, S. Kwon, A. Liddle, J. Bokor, and H. Schmidt, "Magneto-optical observation of picosecond dynamics of single nanomagnets," *Nano Lett.* **6**, 2939–2944 (2006).

[91] Z. Liu, R. Sydora, and M. Freeman, "Shape effects on magnetization state transitions in individual 160-nm diameter Permalloy disks," *Phys. Rev. B* **77**, 174410 (2008).

[92] P. S. Keatley, P. Gangmei, M. Dvornik, R. J. Hicken, J. R. Childress, and J. A. Katine, "Large amplitude magnetization dynamics and the suppression of edge modes in a single nanomagnet," *Appl. Phys. Lett.* **98**, 082506 (2011).

[93] R. Brandt, F. Ganss, R. Rückriem, T. Senn, C. Brombacher, P. Krone, M. Albrecht, and H. Schmidt, "Three-dimensional shape dependence of spin-wave modes in single FePt nanomagnets," *Phys. Rev. B* **86**, 094426 (2012).

[94] V. Uhlíř, M. Urbánek, L. Hladík, J. Spousta, M.-Y. Im, P. Fischer, N. Eibagi, J. J. Kan, E. E. Fullerton, and T. Sikola, "Dynamic switching of the spin circulation in tapered magnetic nanodisks.," *Nat. Nanotechnol.* **8**, 341–346 (2013).

[95] S. Tamaru, K. Yakushiji, A. Fukushima, S. Yuasa, and H. Kubota, "Ultrahigh Sensitivity Ferromagnetic Resonance Measurement Based on Microwave Interferometer," *IEEE Magn. Lett.* **5**, 1–4 (2014).

[96] A. Aharoni, Introduction to the Theory of Ferromagnetism, 2nd ed. (Oxford University Press, Oxford, 1996).

[97] S. Chikazumi, Physics of Ferromagnetism (Oxford University Press, Oxford, 1997).

[98] U. Mizutani, Introduction to the Electron Theory of Metals (Cambridge University Press, Cambridge, 2001).

[99] R.M. White, Quantum Theory of Magnetism, 3rd ed. Springer Series in Solid State Sciences vol. 32 (Springer, Berlin, Heiderlberg, 2007).

[100] L. Landau, and E. Lifshits, "on the Theory of the Dispersion of Magnetic Permeability in Ferromagnetic Bodies," *Phys. Z. Sowjetunion* **8**, 153 (1935).

[101] T. L. Gilbert, "A Lagrangian Formulation of the Gyromagnetic Equation of the Magnetization Field," *Phys. Rev.* **100**, 1243 (1955).

[102] T. L. Gilbert, "Classics in Magnetics A Phenomenological Theory of Damping in Ferromagnetic Materials," *IEEE Trans. Magn.* **40**, 3443–3449 (2004).

[103] A. Barman, S. Wang, O. Hellwig, A. Berger, E. E. Fullerton, and H. Schmidt, "Ultrafast magnetization dynamics in high perpendicular anisotropy $[Co/Pt]_n$ multilayers," *J. Appl. Phys.* **101**, 09D102 (2007).

[104] G. Malinowski, K. C. Kuiper, R. Lavrijsen, H. J. M. Swagten, and B. Koopmans, "Magnetization dynamics and Gilbert damping in ultrathin Co48Fe32B20 films with out-of-plane anisotropy," *Appl. Phys. Lett.* **94**, 102501 (2009).

[105] S. Mizukami, E. P. Sajitha, D. Watanabe, F. Wu, T. Miyazaki, H. Naganuma, M. Oogane, and Y. Ando, "Gilbert damping in perpendicularly magnetized Pt/Co/Pt films investigated by all-optical pump-probe technique," *Appl. Phys. Lett.* **96**, 152502 (2010).

[106] Y. Ren, Y. L. Zuo, M. S. Si, Z. Z. Zhang, Q. Y. Jin, and S. M. Zhou, "Correlation between ultrafast demagnetization process and gilbert damping in amorphous TbFeCo films," *IEEE Trans. Magn.* **49**, 3159–3162 (2013).

[107] J. A. Osborn, "Demagnetizing Factors of the General Ellipsoid," *Phys. Rev.* **67**, 351–357 (1945).

[108] A. G. Gurevich and G. A. Melkov, Magnetization Oscillations and Waves (CRC Press, Boca Raton, 1996).

[109] J. Fidler, and T. Schrefl, "Micromagnetic modelling-the current state of the art," *J. Phys. D* **33**, R135 (2000).

[110] M. E. Schabes, and H. N. Bertram, "Magnetization processes in ferromagnetic cubes," *J. Appl. Phys.* **64**, 1347–1357 (1988).

[111] Y. Nakatani, Y. Uesaka, and N. Hayashi, "Direct Solution of the Landau-Lifshitz-Gilbert Equation for Micromagnetics," *Jpn. J. Appl. Phys.* **28**, 2485–2507 (1989).

[112] T. R. Koehler, and D. R. Fredkin, "Finite element methods for micromagnetics," *IEEE Trans. Magn.* **28**, 1239–1244 (1992).

[113] S. W. Yuan, and H. N. Bertram, "Fast adaptive algorithms for micromagnetics," *IEEE Trans. Magn.* **28**, 2031–2036 (1992).

[114] D. V. Berkov, K. R. Ramstöck, A. Hubert, K. Ramstöcck, and A. Hubert, "Solving micromagnetic problems. Towards an Optimal Numerical Method," *Phys. Stat. Sol.* **137**, 207 (1993).

[115] K. Fabian, A. Kirchner, W. Williams, F. Heider, T. Leibl, and A. Huber, "Three-dimensional micromagnetic calculations for magnetite using FFT," *Geophys. J. Int.* **124**, 89–104 (1996).

[116] D. V. Berkov, and N. L. Gorn, "Quasistatic remagnetization processes in two-dimensional systems with random on-site anisotropy and dipolar interaction: Numerical simulations," *Phys. Rev. B* **57**, 14332–14343 (1998).

[117] Q. Chen, and A. Konrad, "A review of finite element open boundary techniques for static and quasi-static electromagnetic field problems," *IEEE Trans. Magn.* **33**, 663–676 (1997).

[118] T. R. Koehler, "Hybrid FEM-BEM method for fast micromagnetic calculations," *Phys. B Condens. Matter* **233**, 302–307 (1997).

[119] M. Donahue and D. G. Porter, OOMMF User's guide, Version 1.0, Interagency Report NISTIR 6376, National Institute of Standard and Technology, Gaithersburg, MD (1999); http://math.nist.gov/oommf

[120] A. Vansteenkiste, J. Leliaert, M. Dvornik, M. Helsen, F. Garcia-Sanchez, and B. Van Waeyenberge, "The design and verification of MuMax3," *AIP Adv.* **4**, 107133 (2014).

[121] W. Scholz, J. Fidler, T. Schrefl, D. Suess, R. Dittrich, H. Forster, and V. Tsiantos, "Scalable parallel micromagnetic solvers for magnetic nanostructures," *Comput. Mater. Sci.* **28**, 366–383 (2003).

[122] T. Fischbacher, M. Franchin, G. Bordignon, and H. Fangohr, "A Systematic Approach to Multiphysics Extensions of Finite-Element-Based Micromagnetic Simulations: Nmag," *IEEE Trans. Magn.* **43**, 2896–2898 (2007).

[123] H. Forster, T. Schrefl, R. Dittrich, W. Scholz, and J. Fidler, "Fast Boundary Methods for Magnetostatic Interactions in Micromagnetics," *IEEE Trans. Magn.* **39**, 2513–2515 (2003).

[124] A. Knittel, M. Franchin, G. Bordignon, T. Fischbacher, S. Bending, and H. Fangohr, "Compression of boundary element matrix in micromagnetic simulations," *J. Appl. Phys.* **105**, 07D542 (2009).

[125] M. Faraday, "Experimental Researches in Electricity. Nineteenth Series," *Philos. Trans. R. Soc. London* **136**, 1 (1846).

[126] P. Fumagalli, "Scanning Near-field Optical Microscopy (SNOM, NSOM)," [Modern Techniques for Characterizing Magnetic Materials], edited by Y. Zhu (Springer, New York, 2005).

[127] H. A. Lorentz, Versuch einer Theorie der elektrischen und optischen Erscheinungen in bewegten Körpern (Springer Netherlands, 1937).

[128] C. C. Robinson, "Longitudinal Kerr Magneto-Optic Effect in Thin Films of Iron, Nickel, and Permalloy," *J. Opt. Soc. Am.* **53**, 681 (1963).

[129] J. Zak, E. R. Moog, C. Liu, and S. D. Bader, "Magneto-optics of multilayers with arbitrary magnetization directions," *Phys. Rev. B* **43**, 6423–6429 (1991).

[130] M. R. Freeman, M. J. Brady, and J. Smyth, "Extremely high frequency magneto-optic sampling pulse magnetic resonance by picosecond magneto-optic sampling," *Appl. Phys. Lett.* **60**, 2555–2557 (1992).

[131] R. J. Hicken, and J. Wu, "Observation of ferromagnetic resonance in the time domain," *J. Appl. Phys.* **85**, 4580–4582 (1999).

[132] T. Gerrits, H. A. M. van den Berg, J. Hohlfeld, O. Gielkens, L. Bär, and T. Rasing, "Picosecond control of coherent magnetisation dynamics in permalloy thin

films by picosecond magnetic field pulse shaping," *J. Magn. Magn. Mater.* **240**, 283–286 (2002).

[133] J. Wu, N. D. Hughes, J. R. Moore, and R. J. Hicken, "Excitation and damping of spin excitations in ferromagnetic thin films," *J. Magn. Magn. Mater.* **241**, 96–109 (2002).

[134] R. J. Hicken, A. Barman, V. V Kruglyak, and S. Ladak, "Optical ferromagnetic resonance studies," *J. Phys. D. Appl. Phys.* **36**, 2183–2192 (2003).

[135] T. Korn, F. Giesen, J. Podbielski, D. Ravlic, C. Schueller, and D. Grundler, "Time-resolved study of the increased magnetization precession frequency in Fe wires," *J. Magn. Magn. Mater.* **285**, 240–244 (2005).

[136] E. Beaurepaire, J.-C. Merle, A. Daunois, and J.-Y. Bigot, "Ultrafast Spin Dynamics in Ferromagnetic Nickel," *Phys. Rev. Lett.* **76**, 4250–4253 (1996).

[137] B. Koopmans, M. van Kampen, J. Kohlhepp, and W. de Jonge, "Ultrafast Magneto-Optics in Nickel: Magnetism or Optics?," *Phys. Rev. Lett.* **85**, 844–847 (2000).

[138] B. Koopmans, H. H. J. E. Kicken, M. van Kampen, and W. J. M. de Jonge, "Microscopic model for femtosecond magnetization dynamics," *J. Magn. Magn. Mater.* **286**, 271–275 (2005).

[139] F. Dalla Longa, J. T. Kohlhepp, W. J. M. De Jonge, and B. Koopmans, "Influence of photon angular momentum on ultrafast demagnetization in nickel," *Phys. Rev. B* **75**, 224431 (2007).

[140] B. Koopmans, G. Malinowski, F. Dalla Longa, D. Steiauf, M. Fähnle, T. Roth, M. Cinchetti, and M. Aeschlimann, "Explaining the paradoxical diversity of ultrafast laser-induced demagnetization.," *Nat. Mater.* **9**, 259–265 (2010).

[141] A. J. Schellekens, and B. Koopmans, "Microscopic model for ultrafast magnetization dynamics of multisublattice magnets," *Phys. Rev. B* **87**, 020407 (2013).

[142] T. Saito, O. Matsuda, and O. Wright, "Picosecond acoustic phonon pulse generation in nickel and chromium," *Phys. Rev. B* **67**, 205421 (2003).

[143] D. L. D. Connelly, J. S. Loomis, and D. E. DE Mapother, "Specific Heat of Nickel near the Curie Temperature," *Phys. Rev. B* **3**, 924–934 (1971).

[144] F. Hansteen, A. Kimel, A. Kirilyuk, and T. Rasing, "Femtosecond Photomagnetic Switching of Spins in Ferrimagnetic Garnet Films," *Phys. Rev. Lett.* **95**, 047402 (2005).

[145] F. Hansteen, A. Kimel, A. Kirilyuk, and T. Rasing, "Nonthermal ultrafast optical control of the magnetization in garnet films," *Phys. Rev. B* **73**, 014421 (2006).

[146] C. Stanciu, F. Hansteen, A. Kimel, A. Tsukamoto, A. Itoh, A. Kirilyuk, and T. Rasing, "Ultrafast Interaction of the Angular Momentum of Photons with Spins in the Metallic Amorphous Alloy GdFeCo," *Phys. Rev. Lett.* **98**, 207401 (2007).

[147] A. V. Scherbakov, A. S. Salasyuk, A. V. Akimov, X. Liu, M. Bombeck, C. Brüggemann, D. R. Yakovlev, V. F. Sapega, J. K. Furdyna, and M. Bayer, "Coherent Magnetization Precession in Ferromagnetic (Ga,Mn)As Induced by Picosecond Acoustic Pulses," *Phys. Rev. Lett.* **105**, 117204 (2010).

[148] L. Thevenard, E. Peronne, C. Gourdon, C. Testelin, M. Cubukcu, E. Charron, S. Vincent, A. Lemaître, and B. Perrin, "Effect of picosecond strain pulses on thin layers of the ferromagnetic semiconductor (Ga,Mn)(As,P)," *Phys. Rev. B* **82**, 104422 (2010).

[149] M. Bombeck et al., "Excitation of spin waves in ferromagnetic (Ga,Mn)As layers by picosecond strain pulses," *Phys. Rev. B* **85**, 195324 (2012).

[150] M. Bombeck, J. V. Jäger, A. V. Scherbakov, T. Linnik, D. R. Yakovlev, X. Liu, J. K. Furdyna, A. V. Akimov, and M. Bayer, "Magnetization precession induced by quasitransverse picosecond strain pulses in (311) ferromagnetic (Ga,Mn)As," *Phys. Rev. B* **87**, 060302(R) (2013).

[151] J.-W. Kim, M. Vomir, and J.-Y. Bigot, "Ultrafast Magnetoacoustics in Nickel Films," *Phys. Rev. Lett.* **109**, 166601 (2012).

[152] J.-W. Kim, M. Vomir, and J.-Y. Bigot, "Controlling the spins angular momentum in ferromagnets with sequences of picosecond acoustic pulses.," *Sci. Rep.* **5**, 8511 (2015).

[153] B. Koopmans, "Laser-induced magnetization dynamics," [Spin Dynamics in Confined Magnetic Structures II, Topics in Applied Physics, Vol. 87], edited by B. Hillebrands and K. Ounadjela, 253 (Springer, Berlin, Heidelberg, 2003).

[154] D. A. Allwood, G. Xiong, M. D. Cooke, and R. P. Cowburn, "Magneto-optical Kerr effect analysis of magnetic nanostructures," *J. Phys. D. Appl. Phys.* **36**, 2175–2182 (2003).

[155] M. A. C. de Araújo, R. Silva, E. de Lima, D. P. Pereira, and P. C. de Oliveira, "Measurement of Gaussian laser beam radius using the knife-edge technique: improvement on data analysis.," *Appl. Opt.* **48**, 393 (2009).

[156] AutoIt v3; https://www.autoitscript.com/site/autoit/

[157] A. V Oppenheim, R. W. Schafer, and J. R. Buck, Discrete Time Signal Processing, 2nd ed., Princeton Hall, Upper Saddle River, NJ (1999).

[158] M. Djordjevic, G. Eilers, A. Parge, M. Münzenberg, and J. S. Moodera, "Intrinsic and nonlocal Gilbert damping parameter in all optical pump-probe experiments," *J. Appl. Phys.* **99**, 08F308 (2006).

[159] Y. Liu, L. R. Shelford, V. V. Kruglyak, R. J. Hicken, Y. Sakuraba, M. Oogane, and Y. Ando, "Optically induced magnetization dynamics and variation of damping parameter in epitaxial Co 2 MnSi Heusler alloy films," *Phys. Rev. B* **81**, 094402 (2010).

[160] S. Pal, B. Rana, O. Hellwig, T. Thomson, and A. Barman, "Tunable magnonic frequency and damping in $[Co/Pd]_8$ multilayers with variable Co layer thickness," *Appl. Phys. Lett.* **98**, 082501 (2011).

[161] I. Neudecker, G. Woltersdorf, B. Heinrich, T. Okuno, G. Gubbiotti, and C. H. Back, "Comparison of frequency, field, and time domain ferromagnetic resonance methods," *J. Magn. Magn. Mater.* **307**, 148–156 (2006).

[162] H.-S. Song, K.-D. Lee, J.-W. Sohn, S.-H. Yang, S. S. P. Parkin, C.-Y. You, and S.-C. Shin, "Observation of the intrinsic Gilbert damping constant in Co/Ni multilayers independent of the stack number with perpendicular anisotropy," *Appl. Phys. Lett.* **102**, 102401 (2013).

[163] S. Mizukami, D. Watanabe, T. Kubota, X. Zhang, H. Naganuma, M. Oogane, Y. Ando, and T. Miyazaki, "Laser-Induced Fast Magnetization Precession and Gilbert Damping for CoCrPt Alloy Thin Films with Perpendicular Magnetic Anisotropy," *Appl. Phys. Express* **3**, 123001 (2010).

[164] J. A. King, A. Ganguly, D. M. Burn, S. Pal, E. A. Sallabank, T. P. A. Hase, A. T. Hindmarch, A. Barman, and D. Atkinson, "Local control of magnetic damping in ferromagnetic/non-magnetic bilayers by interfacial intermixing induced by focused ion-beam irradiation," *Appl. Phys. Lett.* **104**, 242410 (2014).

[165] G. Woltersdorf, M. Buess, B. Heinrich, and C. H. Back, "Time Resolved Magnetization Dynamics of Ultrathin Fe(001) Films: Spin-Pumping and Two-Magnon Scattering," *Phys. Rev. Lett.* **95**, 037401 (2005).

[166] N. Ross, M. Kostylev, and R. L. Stamps, "Effect of disorder studied with ferromagnetic resonance for arrays of tangentially magnetized sub-micron Permalloy discs fabricated by nanosphere lithography," *J. Appl. Phys.* **109**, 013906 (2010).

[167] N. Qureshi, H. Schmidt, and A. R. Hawkins, "Cavity enhancement of the magneto-optic Kerr effect for optical studies of magnetic nanostructures," *Appl. Phys. Lett.* **85**, 431 (2004).

[168] S. Wang, A. Barman, H. Schmidt, J. D. Maas, A. R. Hawkins, S. Kwon, B. Harteneck, S. Cabrini, and J. Bokor, "Optimization of nano-magneto-optic sensitivity using dual dielectric layer enhancement," *Appl. Phys. Lett.* **90**, 252504 (2007).

[169] D. Weller, "Scanning near-field optical microscope domains in optically opaque materials for the imaging of magnetic," *Appl. Phys. Lett* **65**, 658–660 (1994).

[170] G. Meyer, T. Crecelius, A. Bauer, I. Mauch, and G. Kaindl, "In situ near-field imaging of magnetic domain patterns in ultrathin iron films," *Appl. Phys. Lett.* **83**, 1394 (2003).

[171] Zoriniants, G., et al. "Development of a Near-Field Magneto-Optical Microscopy for Studying Ultrafast Magnetization Dynamics." *AIP Conf. Proc.*. Vol. 696. No. LNS-ARTICLE-2003-001. 2003.

[172] Y. Yahagi, C. R. Berk, B. D. Harteneck, S. D. Cabrini, and H. Schmidt, "Dynamic separation of nanomagnet sublattices by orientation of elliptical elements," *Appl. Phys. Lett.* **104**, 162406 (2014).

[173] C. A. Neugebauer, "Saturation magnetization of nickel films of thickness less than 100 A," *Phys. Rev.* **116**, 1441–1446 (1959).

[174] M. J. Graham, and M. Cohen, "On the Mechanism of Low-Temperature Oxidation (23°–450°C) of Polycrystalline Nickel," *J. Electrochem. Soc.* **119**, 879 (1972).

[175] D. Hurley, and K. Telschow, "Picosecond surface acoustic waves using a suboptical wavelength absorption grating," *Phys. Rev. B* **66**, 153301 (2002).

[176] J.-F. Robillard, A. Devos, and I. Roch-Jeune, "Time-resolved vibrations of two-dimensional hypersonic phononic crystals," *Phys. Rev. B* **76**, 092301 (2007).

[177] C. Giannetti *et al*., "Thermomechanical behavior of surface acoustic waves in ordered arrays of nanodisks studied by near-infrared pump-probe diffraction experiments," *Phys. Rev. B* **76**, 125413 (2007).

[178] Q. Li et al., "Generation and control of ultrashort-wavelength two-dimensional surface acoustic waves at nanoscale interfaces," *Phys. Rev. B* **85**, 195431 (2012).

[179] S. Davis, A. Baruth, and S. Adenwalla, "Magnetization dynamics triggered by surface acoustic waves," *Appl. Phys. Lett.* **97**, 232507 (2010).

[180] N. Tiercelin, Y. Dusch, A. Klimov, S. Giordano, V. Preobrazhensky, and P. Pernod, "Room temperature magnetoelectric memory cell using stress-mediated magnetoelastic switching in nanostructured multilayers," *Appl. Phys. Lett.* **99**, 192507 (2011).

[181] A. Casiraghi, P. Walker, A. V. Akimov, K. W. Edmonds, A. W. Rushforth, E. De Ranieri, R. P. Campion, B. L. Gallagher, and A. J. Kent, "Fast switching of magnetization in the ferromagnetic semiconductor (Ga,Mn)(As,P) using nonequilibrium phonon pulses," *Appl. Phys. Lett.* **99**, 262503 (2011).

[182] L. Thevenard, J.-Y. Duquesne, E. Peronne, H. von Bardeleben, H. Jaffres, S. Ruttala, J.-M. George, A. Lemaître, and C. Gourdon, "Irreversible magnetization switching using surface acoustic waves," *Phys. Rev. B* **87**, 144402 (2013).

[183] M. Weiler, L. Dreher, C. Heeg, H. Huebl, R. Gross, M. Brandt, and S. Goennenwein, "Elastically Driven Ferromagnetic Resonance in Nickel Thin Films," *Phys. Rev. Lett.* **106**, 117601 (2011).

[184] L. Dreher, M. Weiler, M. Pernpeintner, H. Huebl, R. Gross, M. S. Brandt, and S. T. B. Goennenwein, "Surface acoustic wave driven ferromagnetic resonance in nickel thin films: Theory and experiment," *Phys. Rev. B* **86**, 134415 (2012).

[185] O. Kovalenko, T. Pezeril, and V. V. Temnov, "New Concept for Magnetization Switching by Ultrafast Acoustic Pulses," *Phys. Rev. Lett.* **110**, 266602 (2013).

[186] A. K. Biswas, S. Bandyopadhyay, and J. Atulasimha, "Acoustically assisted spin-transfer-torque switching of nanomagnets: An energy-efficient hybrid writing scheme for non-volatile memory," *Appl. Phys. Lett.* **103**, 232401 (2013).

[187] T. Saito, O. Matsuda, M. Tomoda, and O. B. Wright, "Imaging gigahertz surface acoustic waves through the photoelastic effect," *J. Opt. Soc. Am. B* **27**, 2632 (2010).

[188] H.-N. Lin, H. J. Maris, L. B. Freund, K. Y. Lee, H. Luhn, and D. P. Kern, "Study of vibrational modes of gold nanostructures by picosecond ultrasonics," *J. Appl. Phys.* **73**, 37 (1993).

[189] H. Robinson, Y. Hahn, and J. N. Gau, "A comprehensive analysis of surface acoustic wave reflections," *J. Appl. Phys.* **65**, 4573 (1989).

[190] D. Nardi, F. Banfi, C. Giannetti, B. Revaz, G. Ferrini, and F. Parmigiani, "Pseudosurface acoustic waves in hypersonic surface phononic crystals," *Phys. Rev. B* **80**, 104119 (2009).

[191] J. Sadhu, J. H. Lee, and S. Sinha, "Frequency shift and attenuation of hypersonic surface acoustic phonons under metallic gratings," *Appl. Phys. Lett.* **97**, 133106 (2010).

[192] D. E. Bray, and W. Tang, "Subsurface stress evaluation in steel plates and bars using the LCR ultrasonic wave," *Nucl. Eng. Des.* **207**, 231–240 (2001).

[193] Lord Rayleigh, "On Waves Propagated along the Plane Surface of an Elastic Solid," *Proc. London Math. Soc.* **17**, 4–11 (1885).

[194] J. de Klerk, "Ultrasonic transducers," *Ultrasonics* **9**, 35–48 (1971).

[195] J. F. Doyle, Wave Propagation in Structures, 2nd ed. (Springer, New York, 1997)

[196] R. M. Bozorth, "Magnetostriction and Crystal Anisotropy of Single Crystals of Hexagonal Cobalt," *Phys. Rev.* **96**, 311–316 (1954).

[197] O. Song, Ph.D. thesis, "Magnetoelastic Coupling in Thin Films," Massachusetts Institute of Technology (1994).

[198] C. Kittel, "Physical Theory of Ferromagnetic Domains," *Rev. Mod. Phys.* **21**, 541–583 (1949).

[199] C. Kittel, "Interaction of Spin Waves and Ultrasonic Waves in Ferromagnetic Crystals," *Phys. Rev.* **110**, 836–841 (1958).

[200] T. Linnik, A. Scherbakov, D. Yakovlev, X. Liu, J. Furdyna, and M. Bayer, "Theory of magnetization precession induced by a picosecond strain pulse in ferromagnetic semiconductor (Ga,Mn)As," *Phys. Rev. B* **84**, 214432 (2011).

[201] A. Kamra, H. Keshtgar, P. Yan, and G. E. W. Bauer, "Coherent elastic excitation of spin waves," *Phys. Rev. B* **91**, 104409 (2015).

[202] A. Rückriegel, P. Kopietz, D. A. Bozhko, A. A. Serga, and B. Hillebrands, "Magnetoelastic modes and lifetime of magnons in thin yttrium iron garnet films," *Phys. Rev. B* **89**, 184413 (2014).

[203] R. R. Birss, "The Saturation Magnetostriction of Polycrystals," *Proc. Phys. Soc.* **75**, 8–16 (1960).

[204] C. Forestiere, M. D'Aquino, G. Miano, C. Serpico, M. D'Aquino, G. Miano, and C. Serpico, "Finite element computations of resonant modes for small magnetic particles," *J. Appl. Phys.* **105**, 07D312 (2009).

[205] V. V. Naletov et al., "Identification and selection rules of the spin-wave eigenmodes in a normally magnetized nanopillar," *Phys. Rev. B* **84**, 224423 (2011).

[206] J.-P. Berenger, "A perfectly matched layer for the absorption of electromagnetic waves," *J. Comput. Phys.* **114**, 185–200 (1994).

[207] L. Patrick, "The Change of Ferromagnetic Curie Points with Hydrostatic Pressure," *Phys. Rev.* **93**, 384–392 (1954).

[208] OOMMF magnetoelastic extension; http://sourceforge.net/projects/oommf-mel/

[209] Y. Yahagi, B. Harteneck, S. Cabrini, and H. Schmidt, "Controlling nanomagnet magnetization dynamics via magnetoelastic coupling," *Phys. Rev. B* **90**, 140405(R) (2014).

[210] C. Chappert, K. Le Dang, P. Beauvillain, H. Hurdequint, and D. Renard, "Ferromagnetic resonance studies of very thin cobalt films on a gold substrate," *Phys. Rev. B* **34**, 3192–3197 (1986).

[211] P. B. Visscher, and D. M. Apalkov, "Fokker–Planck calculation of spin-torque resistance hysteresis and switching currents," *J. Appl. Phys.* **97**, 10C704 (2005).

[212] P.-W. Huang, and R. H. Victora, "Heat assisted magnetic recording: Grain size dependency, enhanced damping, and a simulation/experiment comparison," *J. Appl. Phys.* **115**, 17B710 (2014).

[213] S. Mizukami, S. Iihama, N. Inami, T. Hiratsuka, G. Kim, H. Naganuma, M. Oogane, and Y. Ando, "Fast magnetization precession observed in $L1_0$-FePt epitaxial thin film," *Appl. Phys. Lett.* **98**, 052501 (2011).

[214] Z. Chen, M. Yi, M. Chen, S. Li, S. Zhou, and T. Lai, "Spin waves and small intrinsic damping in an in-plane magnetized FePt film," *Appl. Phys. Lett.* **101**, 222402 (2012).

[215] D. Sander, "The correlation between mechanical stress and magnetic anisotropy in ultrathin films," *Reports Prog. Phys.* **62**, 809 (1999); Voigt-Reuss average and [Birss PPS 1960] was used to obtain the polycrystalline Co parameters with the hcp grains.

[216] H. Takagi, S. Tsunashima, S. Uchiyama, and T. Fujii, “Stress induced anisotropy in amorphous Gd-Fe and Tb-Fe sputtered films,” *J. Appl. Phys.* **50**, 1642 (1979).